UCLA
UCLA Electronic Theses and Dissertations

**Title**
Coherent Control and Spectroscopy of Valley States of Individual Electrons in Silicon Quantum Dots

**Permalink**
https://escholarship.org/uc/item/9kk9x97s

**Author**
Schoenfield, Joshua Steven

**Publication Date**
2017

Peer reviewed|Thesis/dissertation

eScholarship.org Powered by the California Digital Library
University of California

UNIVERSITY OF CALIFORNIA
Los Angeles

# Coherent Control and Spectroscopy of Valley States of Individual Electrons in Silicon Quantum Dots

A dissertation submitted in partial satisfaction
of the requirements for the degree
Doctor of Philosophy in Physics

by

Joshua Steven Schoenfield

2017

© Copyright by
Joshua Steven Schoenfield
2017

ABSTRACT OF THE DISSERTATION

Coherent Control and Spectroscopy of Valley States of Individual Electrons in Silicon Quantum Dots

by

Joshua Steven Schoenfield
Doctor of Philosophy in Physics
University of California, Los Angeles, 2017
Professor HongWen Jiang, Chair

The pursuit of a quantum computer has been driven both by the prospect of solving otherwise intractable problems as well as the desire to master the quantum control of mesoscopic systems. Lateral quantum dots in semiconductors, particularly in silicon, have garnered considerable attention as a potential host for a quantum bit formed from the states of confined electrons.

The conduction states of electrons in silicon are characterized by an additional degree of freedom, known as the valley degree of freedom. Valley states have certain properties which represent both a complication and an opportunity for the use of electrons in silicon as a qubit. Valley states are 6-fold degenerate, reducing to being very nearly 2-fold degenerate when confined to a quantum well, meaning they have the potential to disrupt many qubit readout schemes for spin based on the Pauli exclusion principle. Also, they are rapidly oscillating relative to one another, making their interaction highly sensitive to atomic scale properties of the confining potential, which are difficult to control when fabricating devices. However, they share many spin-like properties leading to the possibility of familiar control protocols and long coherence times.

We have developed techniques for the fabrication of lateral double quantum dots and experimental procedures for the coherent manipulation and readout of quantum states of confined electrons. Through the use of fast pulses, quantum oscillations between two valley states are induced, allowing the energy splitting between these valley states to be probed to a resolution

not possible with conventional methods of valley spectroscopy. The fabrication techniques and experimental procedures have led to the detection of quantum oscillations in multiple devices, demonstrating the utility and generality of the techniques.

In the course of refining these experimental techniques, we developed software allowing for the linear compensation of multiple experimental parameters. These improvements led to the ability to efficiently adjust the inter-dot tunneling rate, the dot-reservoir tunneling rate and the charge sensing channel sensitivity, control parameters whose fine tuning was vital to the success of the quantum manipulation and readout ultimately achieved.

The dissertation of Joshua Steven Schoenfield is approved.

Karoly Holczer

Kang Lung Wang

HongWen Jiang, Committee Chair

University of California, Los Angeles

2017

*To my family.*

TABLE OF CONTENTS

**1 Introduction to Quantum Computing and Quantum Dots** . . . . . **1**

1.1 Computers: Classical and Quantum . . . . . 1

1.1.1 Quantum Computers . . . . . 2

1.1.2 Single Qubit Evolution . . . . . 4

1.1.3 The DiVincenzo Criteria for physical qubit implementation . . . . . 6

1.2 Semiconductor Quantum dots as Qubits . . . . . 6

1.2.1 Quantum Dots: Artificial Atoms? . . . . . 6

1.2.2 Lateral Semiconductor Quantum Dots . . . . . 7

1.2.3 Charge Qubits . . . . . 8

1.2.4 Spin based Qubits . . . . . 9

1.2.4.1 Single Spin Qubits . . . . . 9

1.2.4.2 Singlet-Triplet Qubits . . . . . 11

1.2.4.3 Exchange Only Qubits . . . . . 12

1.2.5 Hybrid Qubits . . . . . 14

**2 Valley State Physics in Silicon** . . . . . **16**

2.1 The Valley Degeneracy in Bulk Silicon . . . . . 16

2.1.1 Basic Band Theory for Semiconductors . . . . . 16

2.1.2 The valley degeneracy . . . . . 18

2.1.3 Detrimental Effect of Valley States on Quantum Information Applications 19

2.2 Silicon Valley States in Confinement Potentials . . . . . 20

2.2.1 Wells . . . . . 20

2.2.2 Dots in the ideal case . . . . . 21

2.3 Effect of Disorder on Dot Valley States . . . . . 23
2.3.1 Sources of disorder . . . . . 23
2.3.2 Disorder's Effect on valley splitting, exchange coupling and inter-valley tunneling . . . . . 25
2.4 Valleytronics . . . . . 26

**3 Experimental Techniques . . . . . 27**
3.1 Device Fabrication . . . . . 27
3.1.1 Operation Principle . . . . . 27
3.1.2 The Wafer . . . . . 28
3.1.3 Global Alignment Markers . . . . . 31
3.1.4 Ion implantation . . . . . 31
3.1.5 High Temperature Annealing . . . . . 32
3.1.6 Patterning of depletion gates . . . . . 32
3.1.7 Global Accumulation Gate . . . . . 33
3.1.8 Etching and Ohmic Contacts . . . . . 33
3.2 Cryogenic Setup . . . . . 34
3.2.1 $^3$He Sorption refrigerator . . . . . 35
3.2.2 Janis 500 Dilution Refrigerator . . . . . 38
3.2.2.1 The Dilution Mechanism . . . . . 39
3.2.3 Oxford Triton Dry refrigerator . . . . . 40
3.2.4 4 K Device Screening and its Elimination . . . . . 40
3.2.5 Sample Holder and Cap . . . . . 41
3.2.6 Electron Temperature . . . . . 44
3.3 Electronic Control . . . . . 45

3.3.1 Static Biases . . . 45
3.3.2 Fast Pulses . . . 46
3.3.3 Arbitrary Waveform Generation . . . 46
3.3.4 Current Measurements . . . 47

**4 Basic Characterization of Quantum Dot Devices . . . 49**
4.1 Dot transport and Coulomb Blockade . . . 50
4.2 The stability diagram . . . 51
4.2.1 Transition Balancing Model . . . 52
4.3 Charge Sensing . . . 53
4.3.1 DC Transport Measurement . . . 54
4.3.2 Transconductance Measurement . . . 55
4.4 Accumulation Procedure . . . 57
4.4.1 Simultaneous Transport and Sensing . . . 57
4.4.2 Single, Double and Triple Dot modes . . . 59
4.5 Vector Based Control and Compensation . . . 59
4.5.1 Compensation in quantum dots . . . 60
4.5.2 Vector Control Software . . . 61
4.5.2.1 Physical Parameter Vectors and the State object . . . 62
4.5.3 Use in conjunction with QPC/SET . . . 63
4.5.4 Use in tracking an individual quadruple point . . . 64
4.5.4.1 Inter-Dot tunneling rate tuning . . . 64
4.5.4.2 Barrier tunneling rate tuning . . . 66
4.5.5 Use to refine parameter space exploration . . . 68

**5 Coherent Manipulation of Valley States . . . 69**

5.1 The System . . . 71
5.2 Interference fringes and coherent oscillations between two valley states following 75
5.3 Principle of the valley qubit operation and read-out . . . 76
5.4 Detuning Dependent Coherent Oscillations . . . 79
5.5 Phase Coherence . . . 80
5.6 Oscillation at Additional Anti-Crossing and Implications . . . 82
5.7 Diagonal Pulsing and Apparent Coherence Times . . . 82
5.8 Contrast with other reported hybrid systems . . . 84
5.9 Use in Valley Splitting Metrology . . . 86

**6 Noise resistant operation and valley spectroscopy . . . 87**
6.1 The dispersion-decoherence relationship . . . 87
6.2 Valley spectroscopy of several devices . . . 88
6.2.1 Differences in clarity . . . 89
6.2.2 Low Efficiency Spectroscopy . . . 91
6.3 Ramsey-Like Spectroscopy in noise resistant region . . . 92
6.3.1 The $\frac{\pi}{2}$ pulses . . . 96
6.4 Charge Noise Resistance from Non-Valley Systems . . . 96

**7 Future Directions . . . 99**
7.1 Key Improvements and Future Directions . . . 99
7.2 Conclusion . . . 101

**A Simulation and Software . . . 103**
A.1 Simulation of Lock-In Signals . . . 103
A.2 GPU accelerated quantum simulation . . . 104

A.2.1 Details of Implementation with MATLAB `gpuarray` . . . . . 106
A.3 Simulation Aided Design . . . . . 109
A.4 Pulse Design . . . . . 109

**References** . . . . . **115**

LIST OF FIGURES


1.1 Bloch sphere representation and evolution . . . . . 5

1.2 The control axes of an exchange only qubit. . . . . 13

1.3 A hybrid qubit spectrum. . . . . 14

2.1 Valley minima in silicon band structure . . . . . 17

2.2 Valley state spatial oscillation . . . . . 22

2.3 Types of atom-scale disorder in quantum wells . . . . . 24

3.1 The full fabrication stack . . . . . 29

3.2 Device cross section . . . . . 30

3.3 STEM images of SiGe heterostructure . . . . . 30

3.4 Dilution refrigerator photos . . . . . 36

3.5 Early sample holder designs . . . . . 42

3.6 New sample holder setup and protective cap . . . . . 43

4.1 Biased transport through a single dot . . . . . 50

4.2 Simulated double dot stability diagram . . . . . 51

4.3 Simulated double dot stability diagram under bias . . . . . 54

4.4 Lock-in vs broadband charge sensing . . . . . 55

4.5 Electronics setup for lock-in charge sensing . . . . . 56

4.6 Symmetric vs anti-symmetric lock-in excitation . . . . . 57

4.7 Simultaneous charge sensing and transport measurement . . . . . 58

4.8 Single, double and triple dot operation regimes . . . . . 59

4.9 Linear QPC sensitivity compensation outline . . . . . 65

4.10 Vector-based inter-dot tunneling rate tuning . . . . . 65

4.11 High visibility region type switching . . . . . 67

5.1 Configuration for time domain valley oscillations . . . . . 72
5.2 Principle of valley qubit operation . . . . . 74
5.3 Valley dispersion and parameter fitting . . . . . 77
5.4 Detuning dependent coherence bound . . . . . 81
5.5 Second charge configuration valley dispersion details . . . . . 83
5.6 Effect on coherence time from pulse direction . . . . . 85

6.1 Valley oscillations in multiple devices . . . . . 88
6.2 Trapezoidal visibility region explanation . . . . . 90
6.3 Inefficient pulse spectroscopy . . . . . 92
6.4 Canonical Ramsey pulse sequence outline . . . . . 94
6.5 Ramsey-style pulse vs single square pulse . . . . . 94
6.6 Time domain oscillations from a Ramsey pulse and dispersion . . . . . 95
6.7 Protected oscillations from non-valley system . . . . . 98

A.1 A diagram of Runge-Kutta implementation with `gpuarray` . . . . . 107
A.2 Electrostatic simulation of dot designs . . . . . 110
A.3 An example of a pulse to be created for the AWG . . . . . 111
A.4 Parts of a fully specified 4-step pulse . . . . . 113

LIST OF TABLES

3.1 Fabrication Runs Summary . . . . . 31

3.2 Summary of cryogenic systems . . . . . 35

6.1 Summary observed oscillations in different devices . . . . . 88

# ACKNOWLEDGMENTS

I would like to thank the many people who taught me to become a scientist: early on Karen Boles, Brenda Royal and Jay Kranzler; later Paul Sheldon, Charles Bailyn, Robert Grober, Daisuke Nagai, and Kelly Holley-Bockelmann; always Harley Kornblum, Carolyn Crandall and Leslie Schoenfield.

I would like to thank HongWen Jiang. I could not have asked for an advisor of greater wisdom or kindness.

I would like to thank my lab mates — those who came before and who patiently taught me: Xiaojie Hao and Hong Pan; those who will stay on after: Nick Penthorn and Nayana Rajapakse; and those who joined me only briefly before moving on themselves. I would especially like to thank Blake Freeman for his friendship, resilience and skill. He has made these days in lab times of real happiness and excitement.

To Michael and Diana and Mom and Dad. Thank you for making me curious. Thank you for making me silly. Thank you for your words, your visions, your laughs, and your songs. Thank you for your love.

This work was supported by U.S. ARO through Grant No. W911NF1410346. The work presented in chapter 6 was made possible through a collaboration with Jason Petta's research group.

# VITA

| | |
|---|---|
| 2010 | B.S. (Physics), Yale. |
| 2011 | M.S. (Physics), University of California, Los Angeles. |
| 2010 | Chancellor's Fellowship, University of California, Los Angeles. |
| 2010-2014 | Teaching Assistant, Physics and Astronomy Department, University of California, Los Angeles. |
| 2014 | Departmental Teaching Award, Physics and Astronomy Department, University of California, Los Angeles. |
| 2012-2017 | Graduate Student Researcher, Physics and Astronomy Department, University of California, Los Angeles. |

# PUBLICATIONS

Joshua S. Schoenfield, Blake M. Freeman, HongWen Jiang. Coherent Manipulation of Valley States at Multiple Charge Configurations of a Silicon Quantum Dot Device. *Nature Communications* (2017)

Blake M. Freeman, Joshua S. Schoenfield, HongWen Jiang. Comparison of low frequency charge noise in identically patterned Si/SiO2 and Si/SiGe quantum dots *Appl. Phys. Lett.* 108, 253108 (2016)

# CHAPTER 1

# Introduction to Quantum Computing and Quantum Dots

## 1.1 Computers: Classical and Quantum

Within every laptop, desktop, gaming console, smart phone, smart watch and supercomputer, a game is being played. The game is a logic puzzle, based on switches. The rules of this game at the finest level are quite simple: If switch $A$ is on, then switch $B$ should be off. Switch $C$ should be on if and only if switches $A$ and $B$ are different from one another. Rules such as these, built into the connections of circuits, form the building blocks from which nearly all computation is derived. [Pet99] Though these rules are simple, they contain all the power necessary to perform the basic operations of arithmetic. By patterning these logic bearing circuits a billion times over a silicon chip in an exquisitely engineered network and executing their operations billions of times a second, computers achieve the impression of complex and nearly instantaneous interaction in ways that have been referred to, without irony, as magic. As artificial intelligence continues to improve, there is no certainty about the limits of what behaviors these connected switches may simulate, if that word even remains appropriate.

Computers may be thought of as performing a series of operations on inputs and yielding an output. These inputs and outputs are encoded in a string of systems which, like a switch, are in one of two states. The vessel which contains such a binary piece of information is known as a *bit* (short for *binary digit* [Pet99]). There is great flexibility in what the physical realization of a bit is. Within a hard drive, it may be the directions of a magnetic domain. Within a CPU, it may be the state of a transistor. In a garage opener, it may be a literal switch used to specify the signal to transmit. The important thing is that they may be in one of two states. For example, a program which returns the square of an 8-bit number may take as input the state of 8 bits,

00001101, which encode the number 13 in binary, and by performing a series of operations return the output bits 10101001, which encode the number 169.

### 1.1.1 Quantum Computers

Impressive as classical computers[1] are, there are certain problems for which they fail to provide efficient solutions. Some of these problems are hypothesized to be fundamentally difficult. Some problems, such as the halting problem, are shown to be fundamentally impossible. The solutions to some of these problems, however, seem to be efficiently accessible under a different computing paradigm — quantum computing.

In quantum computing, the basic unit of information is no longer the bit, but the *quantum bit*, or *qubit*.[Mer07] Like a classical bit, the qubit is a two state system, with states $|0\rangle$ and $|1\rangle$. However, because it is a quantum two state system, rather than unambiguously being either $|0\rangle$ or $|1\rangle$ at all times, the qubit may be in a general state

$$|\psi\rangle = \alpha_0 |0\rangle + \alpha_1 |1\rangle,$$

where $\alpha_0$ and $\alpha_1$ are complex numbers. That is, the qubit is free to take any state within the complex vector space spanned by the two quantum states $|0\rangle$ and $|1\rangle$.[2]

For multiple qubits, the vector space spanned is $2^n$-dimensional, where $n$ is the number of qubits. For example, if there are two qubits, the states are given by

$$|\Psi\rangle = \alpha_{00} |00\rangle + \alpha_{01} |01\rangle + \alpha_{10} |10\rangle + \alpha_{11} |11\rangle$$

where the binary string within the ket (The $|\#\rangle$ symbol), is a basis state of the system where both qubits have well defined values. If, for example, these basis states encoded integers, then such a system would open up the possibility of spreading an input out over several numbers.

[1] By classical computers, I mean even contemporary computers which use bits taking values of either 0 or 1.

[2] There is an important condition that $|\alpha_0|^2 + |\alpha_1|^2 = 1$. This means that states are actually rays within this complex vector space.

For example, a state $|N\rangle$, where

$$|N\rangle = \frac{1}{\sqrt{4}}|0\rangle + \frac{1}{\sqrt{4}}|1\rangle + \frac{1}{\sqrt{4}}|2\rangle + \frac{1}{\sqrt{4}}|3\rangle,$$

would represent a "number" that was spread out over all the integers between 0 and 3. In a sense, this opens up the possibility of performing calculations in parallel, since an operation done to $|N\rangle$ will be done to $|0\rangle$, $|1\rangle$, $|2\rangle$ and $|3\rangle$ simultaneously.

Measurement of a quantum system collapses the system into one of the measurement states with a probability proportional to the magnitude squared of its coefficient. The subtlety of measurement is what prevents one from being able to use the inherent parallelism of quantum computing to simply "try all the inputs at once." The full algorithms used are correspondingly also quite subtle, and a worthy discussion of them is outside the scope of this thesis. In the webcomic Saturday Morning Breakfast Cereal, a caring mother cautions her child about the hype surrounding quantum computing and describes how a succesful quantum algorithm really works[SW]:

> Sweetie, superposition doesn't mean "and," but it also doesn't mean "or." It means a complex linear superposition of a 0 state and a 1 state...If an event could happen one way with a positive amplitude, and another way with a negative amplitude, the two amplitudes can interfere destructively and cancel each other out...
>
> In quantum computing, the whole idea is just to choreograph a pattern of interference where the paths leading to each wrong answer interfere destructively and cancel out, while the paths leading to the right answer reinforce each other.

The full computational power that could be unlocked by the realization of a quantum computer is not yet determined. Some problems, such as repeated application of a black-box function, $f\,(f\,(f\,(\ldots f\,(x))))$, are known to achieve no speedup[Ozh97]. But there are already specific algorithms that have been developed for a working quantum computer with applications to prime factorization[Sho97], secure communication, optimization and quantum simulation.

### 1.1.2 Single Qubit Evolution

Because the work described here is related to the search for an appropriate qubit system, this thesis will essentially deal with the problem of a qubit on the level of the Schroedinger equation. The normalization constraint on the coefficients of a single qubit state $|\psi\rangle$ allow it to be written, up to an overall phase term which does not affect measurements[3] , as

$$|\psi\rangle = \sin\left(\frac{\theta}{2}\right)|0\rangle + \cos\left(\frac{\theta}{2}\right)e^{i\phi}|1\rangle .$$

This allows the state to be considered as a unit norm 3-vector, with an angle from the $z$-axis of $\theta$ and an azimuthal angle of $\phi$, as can be seen in figure 1.1a. Pointing along the $z$-axis are the two orthogonal qubit states $|0\rangle$ and $|1\rangle$. In fact, in this space, any two anti-polar states will be orthogonal. This mapping is known as the Bloch sphere.[4]

To perform operations on a qubit, one must be able to control its evolution in time. Since it is governed by the laws of quantum mechanics, the state will evolve in time according to the Schrodinger equation:

$$i\hbar\frac{\partial}{\partial t}|\psi\rangle = H|\psi\rangle .$$

The operations within a qubit space may be described as rotations within the Bloch sphere: The Hamiltonian, which is Hermitian, may be decomposed, up to the addition of an identity, into the three Pauli matrices

$$\sigma_x = \begin{pmatrix} 0 & 1 \\ 1 & 0 \end{pmatrix} \qquad \sigma_z = \begin{pmatrix} 0 & i \\ -i & 0 \end{pmatrix} \qquad \sigma_y = \begin{pmatrix} 1 & 0 \\ 0 & -1 \end{pmatrix}$$

[3]This applies so long as the measurement is on this qubit alone. If it is coherenly interfering with another quantum system, then this overall phase could make a difference. In fact, if there is a $2\pi$ rotation about the $z$-axis, the qubit as a whole will acquire a phase of -1. A $4\pi$ rotation is needed to get back to the same state exactly. This fact can be observed using an interferometry experiment.[SN11]

[4]The fact that the Bloch sphere is related to single qubit measurements can also be used to redefine it for mixed states as well. In that case, the position in the bloch sphere can be given by $\left(\langle\sigma_x\rangle, \left\langle\sigma_y\right\rangle, \langle\sigma_z\rangle\right)$, which allows for the possibility of unit norm states.

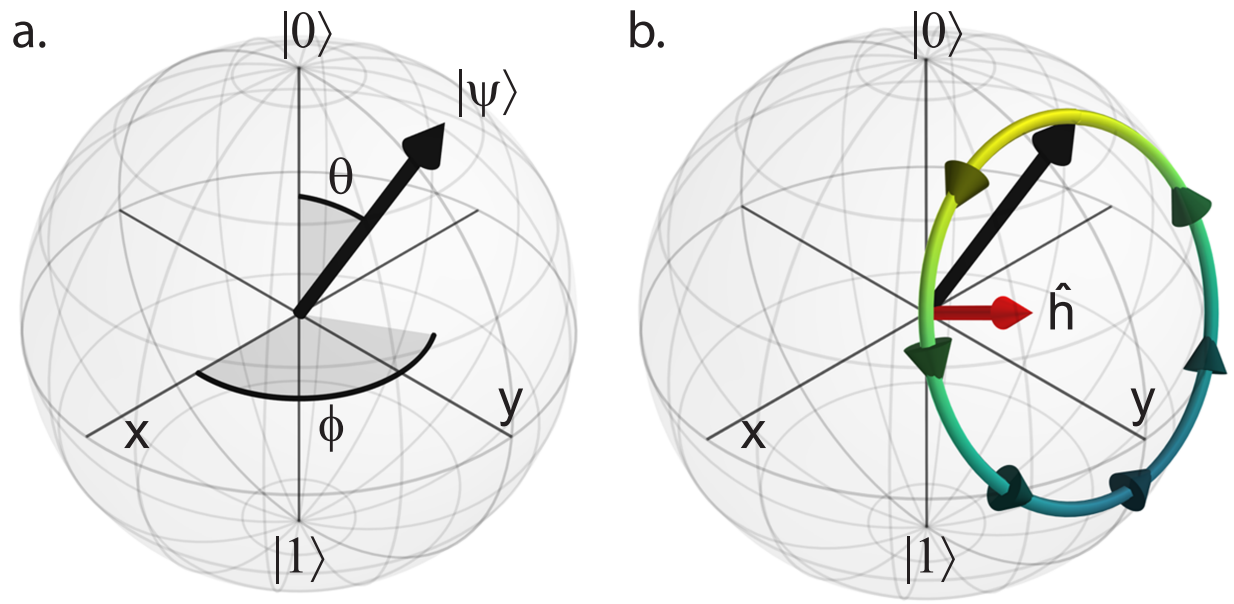


Figure 1.1: (a) Representation of a qubit state $|\psi\rangle$ in the Bloch sphere representation. (b) Demonstration of how a static Hamiltonian evolves a state in the Bloch sphere by providing an axis of rotation.

so that

$$H = cI + h_x\sigma_x + h_y\sigma_y + h_z\sigma_z.$$

The energy eigenvalues will be $c \pm \sqrt{h_x^2 + h_y^2 + h_z^2}$. The 3-vector

$$\vec{h} = \begin{pmatrix} h_x \\ h_y \\ h_z \end{pmatrix}$$

represents an axis of rotation in the Bloch sphere around which the state will precess with an angular frequency of $\omega = \frac{2}{\hbar}\sqrt{h_x^2 + h_y^2 + h_z^2}$. From this description of the time evolution, it can be seen that the two eigenvectors, or stationary states, of the Hamiltonian will be the two states pointing in the $+\hat{h}$ and $-\hat{h}$ directions. Full control of a single qubit can be demonstrated by the ability to apply two linearly independent axes of control for variable times.

### 1.1.3 The DiVincenzo Criteria for physical qubit implementation

Just as there is great flexibility in the physical realization of a classical bit, there is also great flexibility in the physical realization of a qubit. But there are 5 criteria, outlined by David P. DiVincenzo, which are considered vital for the physical implementation of quantum computing. (Wording taken directly from [DiV00])

1. A scalable physical system with well characterized qubits
2. The ability to initialize the state of the qubits to a simple fiducial state, such as $|000\ldots\rangle$
3. Long relevant decoherence times, much longer than the gate operation time
4. A "universal" set of quantum gates
5. A qubit-specific measurement capability

An additional two criteria are identified for qubits intended for quantum communication

1. The ability to interconvert stationary and flying qubits
2. The ability faithfully to transmit flying qubits between specified locations

Furthermore, It has been shown that a universal set of gates for quantum computing may be achieved by one and two qubit gates.[DiV95]

This flexibility has led to many proposed and realized implementations of qubits: in the nitrogen vacancy centers of diamonds, in the polarization of photons, in the flux and charge of superconducting Josephson junctions–and others. In this thesis, I describe work done which advances the use of semiconductor lateral quantum dots as a host for a qubits.

## 1.2 Semiconductor Quantum dots as Qubits

### 1.2.1 Quantum Dots: Artificial Atoms?

A student studying quantum physics for the first time is introduced to atoms in a way that may seem rather ignominious for the system that is so frequently encountered in our daily

lives. The atom becomes simply another potential for a particle to live in, the particle being the electron and the potential being supplied by the attractive force of the nucleus. The hydrogen atom is reduced to a spherically symmetric potential energy trap which may store an electron. Nevertheless, many of the phenomena of chemistry, such as bonding and emission, flow from this simple model.

*Quantum dots* are man made traps for electrons, where the electron is confined in all three dimensions. Given that the basic model of an atom is also simply a trap for an electron, it is perhaps unsurprising they exhibit many of the same phenomena of natural atoms. But, unlike natural atoms, the properties of these electron traps may be engineered.

Quantum dots have a wide range of applications. Some of them are used as tracer particles in biological systems. Recently, commercial displays have been brought to market using quantum dots in the production of colors.

### 1.2.2 Lateral Semiconductor Quantum Dots

The form of quantum dots whose study is detailed in this thesis is known as a lateral semiconductor quantum dot. In this design, a two dimensional electron gas is partitioned using confining gates in order to form pockets where individual electrons may be trapped. Electrons within these pockets exhibit total quantization of momentum states and are therefore referred to as quantum dots.

The design of these systems, particularly the fact that many of the details of the confinement are controlled by electrostatic voltages, allow for the exquisite control over the various degrees of freedom of the electrons contained within. The voltages can be used to raise and lower the energy of individual electrons within dots and effect transitions between the dots. In particular the position and spin degrees of freedom are of interest for quantum information applications. The designed electronic confinement allows for the probing of both of these degrees of freedom.

In the following sections, I try to emphasize the common goal of achieving two axis control over a qubit subspace using the control over the degrees of freedom afforded by electrostatically defined quantum dots.

### 1.2.3 Charge Qubits

The charge degree of freedom refers to the location of the charge bearing particles. In the case of dots, this means the electrons' locations within the dots. A qubit space can be made using the position of a single electron within a double dot system. Let the state corresponding to the electron being in the left dot, $|L\rangle$, and the state corresponding to the electron being in the right dot, $|R\rangle$, be the two spanning states.

The Hamiltonian can be described in the $\{|L\rangle, |R\rangle\}$ basis as

$$H = \frac{t_c}{2}\sigma_x + \frac{\varepsilon}{2}\sigma_z = \begin{pmatrix} \frac{\varepsilon}{2} & \frac{t_c}{2} \\ \frac{t_c}{2} & -\frac{\varepsilon}{2} \end{pmatrix},$$

The parameter $\varepsilon$, known as the detuning, is the chemical potential asymmetry between the two dots. This can be controlled dynamically by adjusting the parameters of the dots. The ability for the electron to tunnel between the two dots, that is to go from state $|R\rangle$ to $|L\rangle$ and back is governed by the tunnel coupling, $t_c$.

When the detuning is large compared to $t_c$, then the energy eigenstates become almost purely $|R\rangle$ and $|L\rangle$, with energies of $\pm\frac{1}{2}\sqrt{\varepsilon^2 + t_c^2}$. The axis of control is nearly exactly along the $z$-axis. However, when the chemical potential of the two dots is made equal, i.e. when $\varepsilon = 0$, then the eigenstates become the even and odd superpositions of $|R\rangle$ and $|L\rangle$, that is

$$\frac{|R\rangle \pm |L\rangle}{\sqrt{2}}.$$

The axis of rotation in the Bloch sphere points along the $x$-axis, which would tend to flip between $|R\rangle$ and $|L\rangle$ with a frequency of $\frac{t_c}{2\pi\hbar}$. Furthermore, at this point, there is a reduced sensitivity to noise. Two axis control can be achieved by switching between 0-detuned and far-detuned configurations.

Another way of achieving two axis control has been demonstrated using Landau-Zenerer transitions.[CLT13] This involves sweeping the detuning from a positive value to a negative value and back again. The total effect of this sweep may be contained in a single rotation

operation of $R(\theta, \phi)$, where $\theta$ is roughly controlled by the rise time of the sweep and $\phi$ is controlled by the total duration of the pulse.

An advantage of charge qubits is that they may be measured directly along the $|R\rangle \leftrightarrow |L\rangle$ axis by any measurement method capable of detecting different electronic configurations. Often used is a charge sensing current channel, which runs adjacent to the dots, and whose resistance depends on the charge occupation of the dots.[CLT13, DSP11] Recently, the charge state of such a system has been coupled to a microwave photon.[MCZ17]

A disadvantage of charge qubits is that they are highly susceptible to charge noise. It has been suggested that this problem is likely to preclude charge qubits from being useful in the long term.[Hou12] Recent results suggest, however, that with sufficient suppression of charge noise through device design choices, significantly longer coherence times in charge qubits could be possible.[MCZ17]

### 1.2.4 Spin based Qubits

#### 1.2.4.1 Single Spin Qubits

A textbook example of a two state system is the spin state of an electron. An electron is a spin-$\frac{1}{2}$ particle, and therefore its spin degree of freedom is two dimensional. The spin states of the electron are spin up, $|\uparrow\rangle$, or spin down,$|\downarrow\rangle$ (along the $z$-axis). Therefore, this would seem a natural candidate for a qubit system, and indeed some of the earliest proposed dot-based qubit implementations involved the manipulation of single spins.[LD98]

The spin up and spin down states may be split from one another by applying a large magnetic field. Doing so leads to a Zeeman energy splitting of $\Delta E_Z = g\mu_B B$, where $\mu_B$ is the Bohr magneton and $g$ is the anomalous gyromagnetic ratio. The Hamiltonian for a single spin system in a magnetic field is

$$H = g\mu_B \vec{B} \cdot \vec{S} = g\mu_B \left( B_x \sigma_x + B_y \sigma_y + B_z \sigma_z \right).$$

To produce Bloch sphere rotations, in initial proposals it was suggested that the magnetic field

itself could be turned on and off via probes[LD98]. More common now is to produce Rabi oscillations via electron spin resonance (ESR). To drive ESR oscillations between $|\uparrow\rangle$ and $|\downarrow\rangle$, a small oscillatory magnetic field perpendicular to the large external field is applied via a microwave stripline running in close proximity to the dots. [KBV07, VHY14] (It must be microwave because the energy splitting must be well above the thermal energy scale.) The frequency of the microwave is given by $\frac{\Delta E_Z}{2\pi\hbar}$, and drives flipping between $|\uparrow\rangle$ and $|\downarrow\rangle$ in the Bloch sphere whose frequency depends on applied power.

Alternatively to ESR, a magnetic field gradient in conjunction with an oscillatory electric field can be used to induce EDSR.[KJS16] To supply a gradient suitable for EDSR, groups have patterned permanent micro-magnets close to the dots. Close to these magnets, the field gradient can become large enough that a changing electric field applied through the confinement gates can, from the electrons point of view, produce a similar effect to an oscillatory magnetic field. By necessity operation of this qubit requires the application of microwave signals, which provides an additional engineering challenge.

An advantage of using single spins as qubits is that two qubits could be coupled, as is necessary for multi-qubit gates, by lowering the potential barrier between two individual electrons, allowing their exchange coupling to facilitate their interaction, through the exchange Hamiltonian $H_{\text{int}} = J(t)\,\vec{S}_1 \cdot \vec{S}_2$[AM76, LD98].

A difficulty, particularly in silicon, where the randomized hyperfine magnetic field is small, is the the addressing of individual qubits, as two adjacent electrons are likely to have the same or very similar resonant frequency. This may also be addressed through the addition of a micromagnet[BSO11] to produce a magnetic field gradient or through using the stark effect to adjust $g$[VYH15].

A necessity of all spin based qubits is some way of translating the spin state into a charge state, in what is known as spin to charge conversion. With single dots, this can be done by using a second dot and the pauli exclusion principle, allowing the qubit electron to transfer into the already occupied dot only if the spin state is different from that already in the second dot.[HRX14] Alternatively, one could use spin dependent tunneling, where the Fermi level of

an electron reservoir is placed between the two Zeeman levels. This allows for the system to relax to the ground state by having the electron tunnel out of the dot and then having another electron tunnel in. This corresponds to a temporary change in dot occupancy that is indicative of the spin state of the electron.

#### 1.2.4.2 Singlet-Triplet Qubits

Singlet-Triplet based qubits are formed in double quantum dot systems. They are governed by the exchange Hamiltonian in the presence of a magnetic field:

$$H = J(\varepsilon)\,\vec{S}_L \cdot \vec{S}_R + g\mu\vec{B}_L \cdot \vec{S}_L + g\mu\vec{B}_R \cdot \vec{S}_R$$

There are two electrons, meaning that the qubit space is a subspace of the full spin Hilbert space. The two qubit states are given by the symmetric triplet state with total spin 1, and the anti-symmetric singlet state with total spin $S = 0$, written as

$$|0\rangle \to |T_0\rangle = \frac{1}{\sqrt{2}}\left(|\uparrow\downarrow\rangle + |\downarrow\uparrow\rangle\right),$$

$$|1\rangle \to |S\rangle = \frac{1}{\sqrt{2}}\left(|\uparrow\downarrow\rangle - |\downarrow\uparrow\rangle\right)$$

respectively[SN11].[5] In a spatially homogeneous magnetic field, where the exchange terms dominate, these are energy eigenstates, with an energy splitting given by $J$.[AM76] Furthermore, due to the Pauli exclusion principle, $|0\rangle$ is capable of transitioning to a state where both electrons are in the same dot, whereas $|1\rangle$ is not. This provides a mechanism for readout.

In the presence of a magnetic field gradient from either the Overhouser field [MBH12] or a micro-magnet [WWP14], the Hamiltonian becomes, in the $\{|T_0\rangle, |S\rangle\}$ basis,

$$H = \frac{1}{2}g\mu_B\Delta B\sigma_x + \frac{1}{2}J(\varepsilon)\,\sigma_x = \frac{1}{2}\begin{pmatrix} J(\varepsilon) & g\mu\Delta B \\ g\mu\Delta B & J(\varepsilon) \end{pmatrix}$$

[5] The remaining two states within the spin Hilbert space are $|T_1\rangle = |\uparrow\uparrow\rangle$ and $|T_{-1}\rangle = |\downarrow\downarrow\rangle$

where $\Delta B$ is the difference in magnetic field between the two dots. Consequently a second axis of control along the $x$-axis becomes available from the gradient in the magnetic field.

#### 1.2.4.3 Exchange Only Qubits

Common to both the single spin architectures and the singlet-triple based architectures was some fine degree of control over the local magnetic field, either through the creation of a field oscillatory in time or a magnetic field with a strong gradient.

There is an alternative design, using triple quantum dot devices, where the entirety of the evolution is caused by the exchange interaction controlled by the confinement gates.[MBT13a] (Although this is not the only form of triple dot coherent control. [GGK12]) With a single electron in each dot, the Hamiltonian includes energy terms from the exchange between the left and middle dot and between the right and middle dot:

$$H = J_L(\varepsilon)\,\vec{S}_L \cdot \vec{S}_M + J_R(\varepsilon)\,\vec{S}_R \cdot \vec{S}_M .$$

The exchange energies are dependent on detuning of the device. The form of this dependence allows for $J_L$ to be much greater than $J_R$ when the device is tuned towards the (2,0,1) regime, where this 3-tuple represents the number of electrons in each of the dots. Similarly $J_R \gg J_L$ when the device is tuned to the (1,0,2 regime). The spin Hilbert space is $2^3 = 8$ dimensional. Following the rules for addition of angular momenta, the spin states can be decomposed into one four dimensional space with total spin $S = \frac{3}{2}$, and a couple of two dimensional spaces with total spin $S = \frac{1}{2}$. The qubit subspace is chosen as two of the $S = \frac{1}{2}$ states with the same spin projection number[6]:

$$|0\rangle = \frac{1}{\sqrt{6}}\left(|\uparrow\uparrow\downarrow\rangle + |\downarrow\uparrow\uparrow\rangle - 2\,|\uparrow\downarrow\uparrow\rangle\right),$$
$$|1\rangle = \frac{1}{\sqrt{2}}\left(|\uparrow\downarrow\uparrow\rangle - |\downarrow\uparrow\uparrow\rangle\right).$$

[6]There are actually two candidate pairs for the qubit space, one with spin projection number $m_z = +\frac{1}{2}$ and one with $m_z = -\frac{1}{2}$.

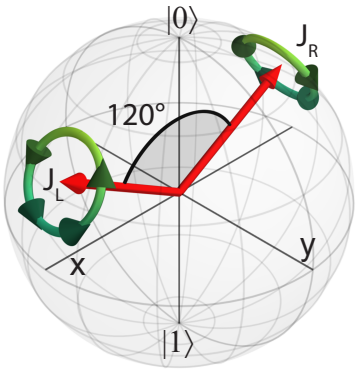


Figure 1.2: The control axes associated with $J_L$ and $J_R$ in an exchange only qubit.

These are energy eigenstates when $\varepsilon$ is tuned to the middle of the (1,1,1) regime so that $J_L$ and $J_R$ are equal. The state $|0\rangle$ connects continuously in $\varepsilon$ to singlet states between either the left two or right two electrons. This state can tunnel to the (2,0,1) or (1,0,2) regime. In contrast, $|1\rangle$ connects to triplet states and is blockaded from such a transition. This provides the readout mechanism and the initialization mechanism for this subspace.

Control in this subspace is mediated by the exchange Hamiltonian, which may be written, up to an constant term proportional to the identity, in the $\{|0\rangle, |1\rangle\}$basis as:

$$H = \begin{pmatrix} -\frac{(J_L+J_R)}{4} & \frac{\sqrt{3}(J_L-J_R)}{4} \\ \frac{\sqrt{3}(J_L-J_R)}{4} & \frac{J_L+J_R}{4} \end{pmatrix} = \frac{J_R}{4}\left(-\sqrt{3}\sigma_x + \sigma_z\right) + \frac{J_R}{4}\left(\sqrt{3}\sigma_x + \sigma_z\right)$$

This provides the two axes of control, since $J_L$ is proportional to one axis and $J_R$ is proportional to another differing by 120°, as can be seen in figure 1.2. As the detuning is adjusted, the relative strength of $J_L$ or $J_R$ can be changed.

There are two modes for exchange only qubits: direct exchange mode[MBT13a] (in silicon: [ELS15]) or resonant exchange mode[TSM13, MBT13b]. The former works by utilizing the two separate axes of control provided by $J_L$ and $J_R$ directly. The latter works close to the regime where $J_L$ and $J_R$ are equal, leading to an axis of control nearly completely in the $z$-direction. Then an oscillatory perturbation is made to the gates, leading to a small oscillatory term in $x$, which can produce Rabi oscillations. A major advantage of exchange only qubits is that they can be controlled only electrically and do not require the incorporation of any magnetic field

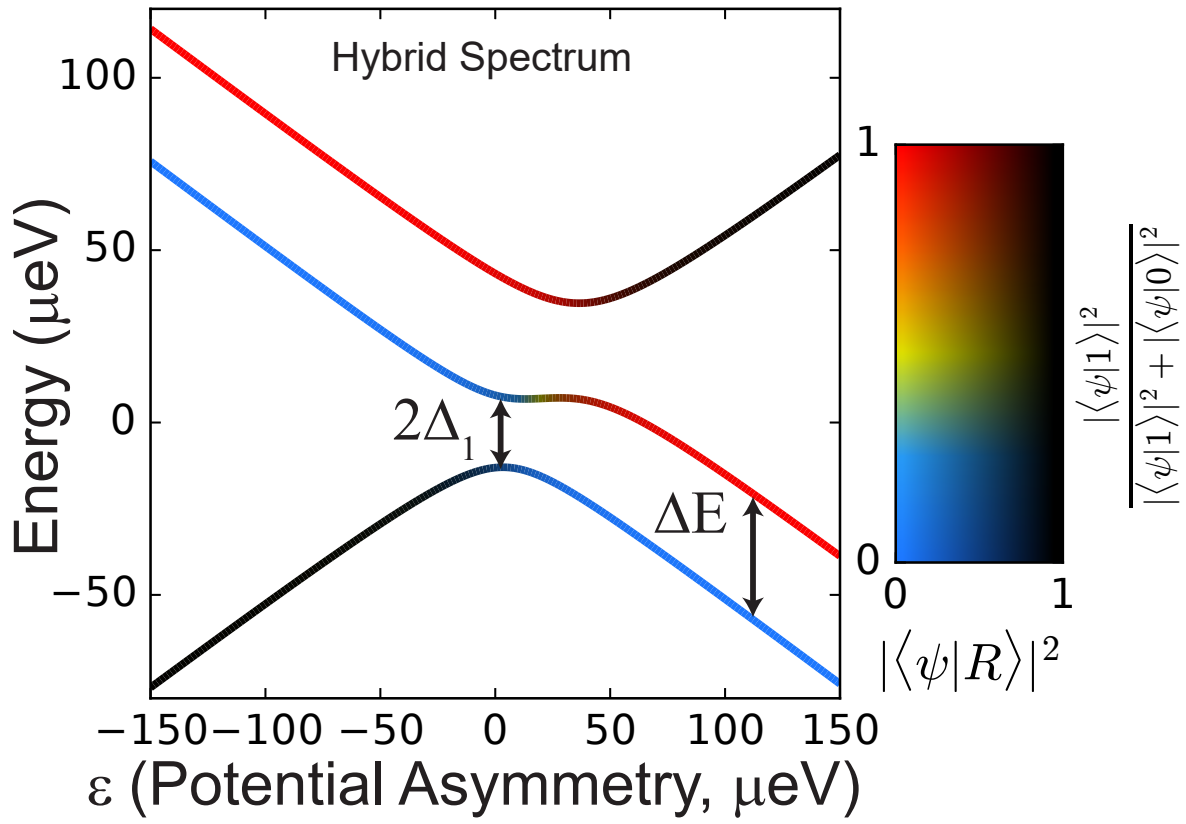


Figure 1.3: A spectrum from a hybrid qubit as a function of detuning as reported by another group. [KSS14]

gradients. The resonant exchange mode qubits, in particular work in a regime protected from charge noise, which is another advantage.

### 1.2.5 Hybrid Qubits

A more recently developed qubit is the hybrid qubit[KGF12, KSS14, CLY16]. This qubit combines the fast operation times associated with charge qubits with the long coherence times associated with spin qubits. Using the sweet spot at the level anti-crossing of two charge states as one axis of control and a second sweet spot in the far detuning regime, where the levels are quite parallel, fast operation times can be achieved in comparison to singlet-triplet qubits which require at least one of the axes to be slow relative to the other.

The classic hybrid qubit, though it relies on a spin state, in some ways bears more resemblance to a charge qubit. The two qubit states have the same charge occupation number, and the

third state has a different charge occupation number. In the basis of $\{|R\rangle, |0\rangle, |1\rangle\}$, where $|R\rangle$ is the state with differing occupation configuration, the Hamiltonian can be written:

$$H = \begin{pmatrix} \frac{\varepsilon}{2} & \Delta_1 & \Delta_2 \\ \Delta_1 & -\frac{\varepsilon}{2} & 0 \\ \Delta_2 & 0 & -\frac{\varepsilon}{2} + \Delta E \end{pmatrix}$$

The hybrid qubit involves, at a minimum, three relevant states, and the spectrum can be seen in figure 1.3. Therefore, discussion of what operations are occurring in the Bloch sphere space at the point of the charge transition are complicated. Broadly speaking, $\Delta_1$ can be said to facilitate the charge transition, while $\Delta_2$ is large enough as to result in adiabatic transitions. While $\Delta E$, which dominates the level splitting as $\varepsilon$ gets large, controls $z$ rotations in the proper qubit subspace. When adiabatic mapping between the levels are taken into account, the transition facilitated at the charge crossing is analogous to an $x$-rotation in the proper Bloch sphere. The main difference between a hybrid qubit and a charge qubit is simply that rather than diverge, the states approach a wide sweet spot at larger detuning, where the exchange interaction is suppressed and the energy levels are parallel.[KSS14]

Though the specific spin states and occupation numbers are often specified within theoretical descriptions of hybrid qubits, the general notion of using the charge transition as one of two parts in a . For example, in chapter 5 of this thesis, I present what could be reasonably described as a Valley-Charge hybrid qubit.

# CHAPTER 2

# Valley State Physics in Silicon

## 2.1 The Valley Degeneracy in Bulk Silicon

### 2.1.1 Basic Band Theory for Semiconductors

A fundamental feature of crystals is their periodicity. The lattice sites occupied by the atoms forming the crystals create repeating spatial patterns, which vary in geometry depending on the makeup of the crystal. It is in this sense that silicon shares a geometry with diamond since they both have a "face-centered cubic" lattice structure. From the perspective of an electron contained within a crystal, this means that the Hamiltonian describing its motion is periodic.

An important result from such a system, is that if a symmetry in the lattice exists such that the Hamiltonian is invariant under a displacement $\vec{R}$ then.

$$\psi = u_{\vec{k}}(\vec{r})\, e^{i\vec{k}\cdot\vec{r}} \qquad\qquad u_{\vec{k}}\left(\vec{r}+\vec{R}\right) = u(\vec{r})$$

That is, the periodicity of the lattice manifests as a periodicity in one part of a separable energy eigenstate wave function, where the other part is a spatially dependent phase described by a plane wave of wave vector $\vec{k}$. This result is known as Bloch's theorem.[AM76]

The wave vector $\vec{k}$ no longer describes the ordinary momentum as it would for a free particle. Instead, it indexes the energy eigenstates and describes by what phase the wave function is changed when it is shifted by a unit cell. But, due to its functional similarities to the momentum of a free particle, the quantity $\hbar\vec{k}$ is called the crystal momentum.

If one maps out the energy dependence of the wave functions vs $k$, one gets a band diagram. Visualizing the three dimensional $\vec{k}$-dependence of $E$ is not easy. But band diagrams provide a

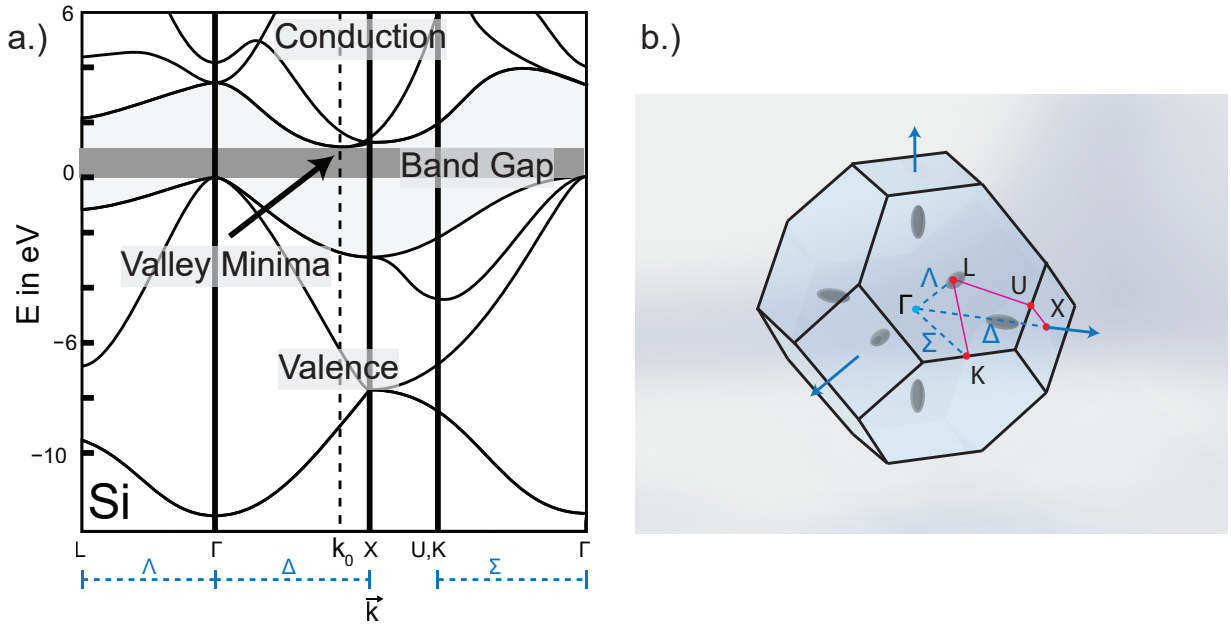


Figure 2.1: (a) The band structure of silicon (b) The first Brillouin zone of silicon, with directions and points of symmetry labeled to aid in reading the band structure. Furthermore, the positions in $\vec{k}$ space of the 6 valley minima are shown as ellipses of constant energy around the valley minima.

useful tool to this end. Such a band diagram (drawn here in its reduced form [Dav97]) is not a complete description of the dependence of $E$ on $\vec{k}$. Rather, it serves to highlight the dependence of $E$ along those axes of the Brillouin zone with high symmetry.

Electrons are fermions, and therefore they will tend to fill up successive low lying energy states without doubly occupying any. A material can conduct only if a band is partially filled.[AM76] Because every band has as many states as there are unit cells, if every lattice site supplies the same number of electrons, the possibility arises that some bands are completely filled and the rest are completely empty. When this happens, there will be an energy gap between the highest filled band (the highest of the valence bands) and the lowest unfilled band (the lowest of the conduction bands). This is known as the band gap, and when it can not be readily breached by some electrons, then the material acts as an insulator.

There is a special class of materials where at some temperature below their melting point the value of $k_b T$ becomes great enough that an electron may be thermally excited from the valence bands to the conduction bands. When this happens, the electrons can serve as a carrier

for current. In addition, the holes left behind in the valence bands can serve as current carrying particles.

For silicon, the band gap (without doping) is 1.1 eV, which is low enough to make it a semiconductor, but not so low as to allow for significant conduction at room temperature.

Since the electronic properties of a semiconductor are almost entirely determined by those electrons which have been excited to the conduction bands, the properties of the conduction within the band are determined by the dispersion at the lowest point of the conduction band. Specifically, the curvature of these band minima can be used to define the effective mass:

$$E\left(\vec{k}\right) \approx \frac{\hbar^2}{2}\left[\frac{k_x^2}{m_x^*} + \frac{k_y^2}{m_y^*} + \frac{k_z^2}{m_z^*}\right]$$

The parabolic dependence of this on $\vec{k}$ relates the dispersion of the band to the effective masses, $m_x^*$ etc., which are dependent on direction.

### 2.1.2 The valley degeneracy

Within the Brillouin zone of Si, there are six minima of the conduction band, which lie along the $\Delta$ directions, as seen in figure 2.1. By symmetry there are 6 $\Delta$ directions, corresponding to 6 different energy minima of the conduction band. Nearby to each of the minima, the energy can be written in terms of $\vec{k}$ as [Dav97]:

$$E\left(\vec{k}\right) = E_c + \frac{\hbar^2}{2m_0}\left[\frac{(k_x - k_0)^2}{m_\mathrm{L}} + \frac{k_y^2}{m_\mathrm{T}} + \frac{k_z^2}{m_\mathrm{T}}\right]$$

where the $x$ axis is taken to be in the $\Delta$ direction, $m_L \approx .98$ is the longitudinal effective mass, $m_T \approx 0.19$ is the transverse effective mass. This latter effective mass governs the motion of electrons within the plane of the 2DEG, that is formed. This means that equal energy contours close to the minimum form 6 distinct ellipsoids. The location of $k_0$ is roughly 82% of the way to the zone boundary (Between point $\Gamma$, where $k = 0$, and point $X$. That is, $k_0 = 0.82\frac{2\pi}{a}$, where $a$ is the lattice constant.). Electrons with a state near one of these minima could not easily

transition to the other minima since their $\vec{k}$ vectors are too distinct. (Though we shall see that in the presence of disorder in a quantum dot, such valley mixing may occur.

It should be noted that some semiconductors, even those with the same face centered cubic lattice structure, do not exhibit valley states. For example, GaAs has a conduction band minimum at $\vec{k} = 0$. In such an instance, there is only a single point at the origin of the Brillouin zone corresponding to the lowest energy, rather than 6. Furthermore in germanium, the band minima are located at the very edges of the first Brillouin zone along the eight $\Lambda$ axes. The corresponding low lying energy contours form half ellipses which connect to one another due to the periodicity, creating a total of 4 valley states.

In general, the bulk valley states have little effect on the transport properties of semiconductors used in ways that are not explicitly quantum. However, the presence of several states of similar energies can complicate their use in quantum information applications, as shall be further discussed.

### 2.1.3 Detrimental Effect of Valley States on Quantum Information Applications

For many proposed spin-based quantum dot qubits the preferred form of spin to charge conversion makes use of the effect known as Pauli blockade. The source of this effect is the Pauli exclusion principle, which forbids multiple fermions to occupy the same quantum state. Because of this, one can convert spin to charge by using the confinement gates to induce a charge transition which will occur dependent on the spin state of the system.

However, the presence of an additional state with the same charge and spin quantum number but a distinct valley number allows for the lifting of Pauli blockade by allowing for another state to become occupied.

The relative ease with which spin to charge conversion is achieved in GaAs/AlGaAs devices attests to the fact that silicon's valley states are a frustrating factor in achieving high yeild spin based quantum dot devices in silicon.[1] Nevertheless, the strong nuclear spin effecs in GaAs

[1]Additional factors include the higher effective mass in silicon, which results in quantum dots which are smaller and which must be placed in closer proximity to one another to achieve effective exchange coupling.

and the promise of long spin relaxation times in silicon, particularly in isotopically purified $^{28}$Si, means that silicon is the longer term prospect for a host for quantum dot based quantum computing.

## 2.2 Silicon Valley States in Confinement Potentials

The six-fold degeneracy in the band structure of silicon can be lifted in the confines of nanodevices such as quantum wells, which are two dimensional, and quantum dots, which are fully quantized (0 dimensional and confined in all three directions). If the degeneracy were fully lifted such that all valley states other than the ground state were dynamically irrelevant, then the deleterious effects on spin systems would be resolved.

### 2.2.1 Wells

The six fold degeneracy caused by the valley states may be lifted as the device geometry changes from bulk silicon to a silicon quantum well.

In-plane strain in the quantum well partially lifts the 6 fold degeneracy.[ZDM13] The source of this strain is lattice mismatch between the silicon well and the material in which it is embedded. The well used in our devices is embedded within SiGe. For pure silicon the lattice constant, $a$, is 0.5431 nm. The average lattice constant for $Si_{1-x}Ge_x$ has the approximate functional form [Wan14]

$$\bar{a}(x) = (0.5431\,\text{nm}) \cdot \left(1 + (3.68\,\%) \cdot x + (0.49\,\%) \cdot x^2\right).$$

The make-up of the SiGe used in our devices is as high as $x = 0.3$ at the edge of the quantum well, making the mismatch in lattice spacing as high as 1 %. This mismatch produces significant strain within the well, and serves to lift the six fold degeneracy.

The results of this lifting is that the valley states split into a 4-fold degenerate high energy subspace and a 2-fold degenerate low energy subspace.

### 2.2.2 Dots in the ideal case

The additional confinement of electrons in a quantum dot causes the lifting of the remaining valley degeneracy:

Within a dot, within the framework of an effective mass theory, one can calculate that the energy eigenstates will be of form [GEC13, FCT07]:

$$\begin{aligned}\Psi_{\pm}(\vec{r}) &= \frac{1}{\sqrt{2}}\left[u_{-k_0}(\vec{r})\, e^{-ik_0 z} \pm u_{k_0}(\vec{r})\, e^{ik_0 z}\right] h(\vec{r}) \\ &= \frac{1}{\sqrt{2}}\left(|z\rangle \pm |\bar{z}\rangle\right)\end{aligned}$$

where $u_{\pm k_0}$ are the periodic parts of the Bloch functions, $z$ points in the interface direction, $h(\vec{r})$ is the envelope function for a given quantum dot, and we term the two pure valley states $|z\rangle = u_{k_0}(\vec{r})\, e^{ik_0 z} h(\vec{r})$, $|\bar{z}\rangle = u_{-k_0}(\vec{r})\, e^{-ik_0 z} h(\vec{r})$. It can be seen that the off diagonal terms of the Hamiltonian in a basis such as this will give the valley splitting between these two states.

Within a dot the term that leads to the degeneracy lifting will be given by the complex valued term (referred to as the valley orbit coupling):

$$\Delta = \langle z|\left(\mathcal{V} + eEz\right)|\bar{z}\rangle$$

where $\mathcal{V}$ is the interface potential energy and $E$ is the electric field. The magnitude of this quantity can determine whether or not the valley sates will lift Pauli blockade.

Of note is that this quantity is highly dependent on atomic scale details of the interface. Although both $\frac{1}{\sqrt{2}}(|z\rangle + |\bar{z}\rangle)$ and $\frac{1}{\sqrt{2}}(|z\rangle - |\bar{z}\rangle)$ share a very similar envelope function, the wave functions are rapidly oscillating at a wavelength very similar to $2\pi k_0^{-1} \approx 0.65\,\text{nm}$. Consequently they are oscillating rapidly relative to one another. If they are out of phase at the interface, where there is a rapid jump, then a large value can accumulate over a short length scale. For this reason, the effects of atomic scale disorder cannot be ignored. This is a direct consequence of the valley minima being at large crystal momenta.

Within a perfectly smooth interface where the growth direction of the crystal is exactly in

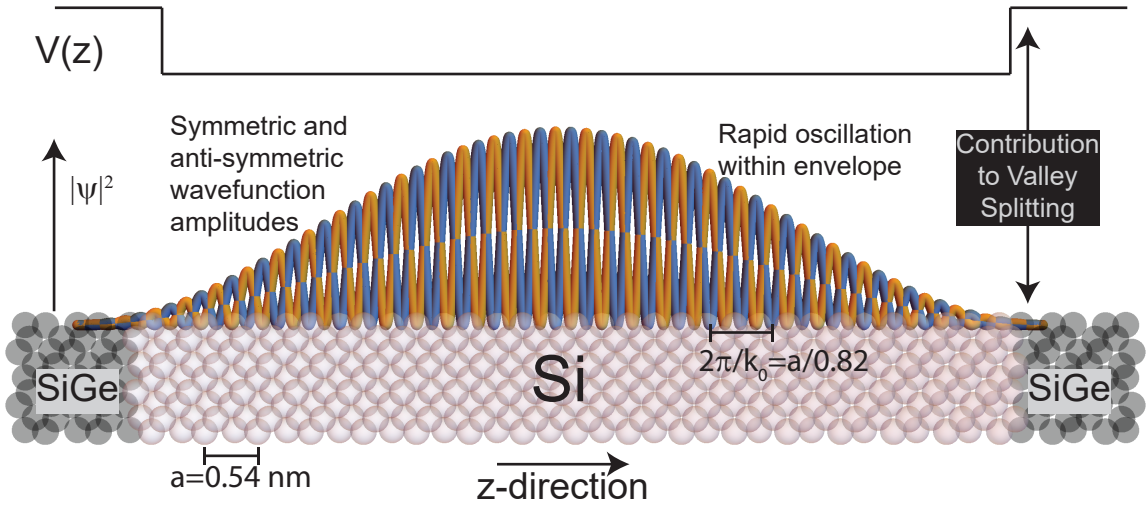


Figure 2.2: The z-dependence of the amplitude of two energy eigenstates within a dot shown to scale with a silicon lattice. The contributions to the valley splitting come mainly from the interface where a rapidly changing potential contributes to the energy of the symmetric and anti-symmetric wave functions differently due to their rapidly varying amplitudes.

the (1,0,0) direction, so that there is not systematic interface stepping, the magnitude of the valley splitting is on the order of 0.1 meV. Because this corresponds to a uniform contribution to the splitting from across the entirety of the interface, this represents the maximum absolute value for the valley splitting. A more realistic picture of the valley splitting requires a consideration of disorder.

Furthermore, in the case of two dots, in the absense of disorder the intervalley tunneling term will be zero:

$$\tau_{-+} = \langle \bar{z}_L \, | H | \, z_L \rangle = 0.$$

This result can also be affected by disorder, which can induce significant inter-valley tunneling. Such a system is observed in chapter 5.

## 2.3 Effect of Disorder on Dot Valley States

An assumption of the models which led to these results was the uniformity of the interface. However, the valley states depend heavily on atomic scale details of the interface. Because the scale of disorder that can affect the valley states is well below the lithographic scale, which is at a minimum 10's of nanometers, in real systems, there are many forms of disorder which could lead to complications of valley physics beyond the picture of the previous sections.

The theoretical approaches for determining the effect of disorder on valley physics have often relied on detailed atomic level simulations. However, a perturbation based approach based off of effective mass theory has also yielded consistent and intuitive results.[GEC13]

The disorder may affect both the magnitude and phase of the valley-orbit coupling[ZHC16]. Most attention has been paid to the magnitude of this difference as it provides the lifting of the Pauli blockade for individual qubit readout. The phase, despite not being important for individual dot operations, is highly relevant for two quantum dots, and can affect their exchange interaction.

### 2.3.1 Sources of disorder

**Step disorders** Step disorders occur when tiered terraces develop at the interfaces of the quantum well, as seen in figure 2.3(a). They will be regularly occurring if there is a mismatch between the direction that the crystal was grown and the $z$ direction resulting in a persistent slant. If there are many step disorders close together, then the the contribution from the wave functions' interactions with the interface are no longer uniform across the whole of the interface. Instead, the contributions from different portions of the interface may cancel each other, resulting in a lower valley splitting. [ZDM13]. (Though the phase contribution to the splitting may remain large as shown in [ZHC16]) Furthermore, step disorders can lead to valley-orbit coupling when the density of step discontinuities is lower. This is because the wave function has space enough to locally adjust to the new geometry, however the phase then becomes spacially dependent, increasing the valley orbit coupling.

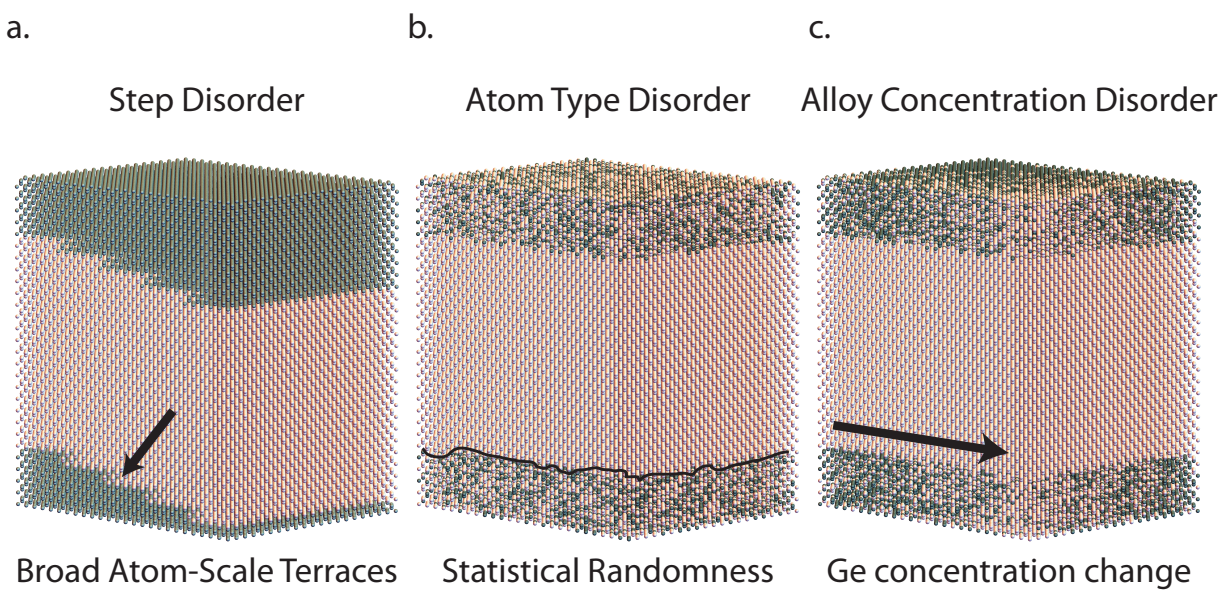


Figure 2.3: Types of atom-scale disorder in quantum wells. (a) Step Disorders, (b) Atom typed disorders. SiGe is actually a mixture of Si and Ge atoms This type of fluctuation can also lead to atom position disorder (c) Alloy concentration disorder.

**SiGe related disorder** All three of these forms of disorder are related to the disorders occurring due to the interspersion of a variable amount of silicon with germanium to enclose a silicon quantum well. These categories come from [ZDM13]:

**Atom Type Disorder** When using a silicon well embedded within SiGe, a form of disorder comes from the statistical fluctuations of which element will occupy which lattice site since both Si and Ge could occupy any of the lattice sites. [ZDM13] This makes the very definition of an interface potentially random. As a result statistical variations in the composition of the individual lattice sites lead to effective interface roughness, as shown in figure 2.3b.

**Atom position disorder** Due to the interspersing of Ge with Si, the resulting crystal no longer has exactly the same inter-atom spacing. Instead, the concentration of Si contributes to a variable spacing. Although the average lattice constant $\bar{a}$ is well described by the formula above, individual lattice sites have variable lengths depending both on the total concentration and on the particular elements being bonded. This spatial variation is another form of disorder

**Alloy Concentration Disorder** The concentration $x$ in $Si_xGe_{1-x}$ is itself another source of disorder, as shown in figure 2.3c. This variation is slow relative to the statistical fluctuations of atom type disorder, but is still on a length scale that can be experienced as disorder contributing to valley-orbit coupling.

### 2.3.2 Disorder's Effect on valley splitting, exchange coupling and inter-valley tunneling

Of great interest is how disorder can affect the magnitude of the valley splitting. The larger this number is, the less likely additional valley states are to interfere in the operation of qubit schemes designed to function with only spin and charge degrees of freedom. As discussed above, the magnitude of the valley splitting will tend to be decreased by the presence of disorder. But the potential ramifications of valley physics for even spin based architectures extend beyond lifting Pauli blockade.

If we consider the valley orbit coupling, $\Delta = |\Delta| e^{i\phi}$, then so long as multiple dots are being considered the phase of this term also plays an important role in determining the operation of the device. Of particular importance for spin based qubits, the exchange splitting, $J$, which was described in chapter 1, depends on the phases of the dots as: $J \propto 1 - \cos(\phi_L - \phi_R)$.[ZHC16] The source of this change in phase can be at least partially attributed to interface roughness in the form of random interfaces and step based disorder.

By studying either sustained roughness [ZHC16] or the presence of a single atomic bump [GEC13], a significant inter-valley tunneling term has been shown to emerge. This will be the case so long as inter-valley mixing is facilitated by the valley-orbit coupling, since the inter-valley coupling is given by $t_{-+} = \frac{t_0}{2}\left[1 - e^{-i(\phi_L - \phi_R)}\right]$.[ZHC16] The fact that these inter-valley tunneling rates are non-zero, and in fact can be larger than the intra-valley tunneling rates are important in the explanation of observed hybrid-like coherent oscillations [SSW14]and will be important in the explanation of the results outlined in chapter 5.

The strong dependence of the valley physics and corresponding device operation on atomic scale details does not completely doom the possibility of reliably producing silicon quantum dots with a high yield. In fact, the very strong dependence on the microscopic details which

would inject randomness into the design can also be used to re-tune the device. For example, the extremely strong dependence on inter-valley transition amplitudes on microscopic details means that this parameter can be tuned over many orders of magnitude by shifting the dot less than 5 nm[ZHC16]. Such a shift would not need to be lithographically designed, but could instead be effected by the tuning of confinement gates.

## 2.4 Valleytronics

Though valley effects have primarily represented a barrier to simple implementation of spin-based quantum information schemes in silicon, there is also the possibility of utilizing the valley degree of freedom. Analogously to spintronics and electronics, which are the use of the spin and charge degrees of freedom, respectively, in engineered devices, valleytronics could lead to novel systems and devices. Valleytronics has been advancing in 2D systems in a variety of materials including graphene[SYC16].

One possibility for valleytronics in silicon is the use of valley states to form a qubit. A proposed design for encoding a qubit with different valley states has been proposed[CSK12]. It is thought that such a device would exhibit excellent resistance to charge noise.

Recently, the valley states of silicon have been used in a double dot system in order to create valley-blockade. [PGT16] This application is directly analogous to the spin blockade, except using the valley degree of freedom in lieu of spin blockade.

The results which will be outlined in chapter 5, where coherent oscillations are induced between two valley states represents such a valleytronics application.

# CHAPTER 3

# Experimental Techniques

## 3.1 Device Fabrication

The early focus of my research was towards realizing spin based qubits in Metal-Oxide-Silicon quantum dot devices (MOS-Dot). Later, the focus of my research shifted towards quantum dots in a Si/SiGe heterostructure. This shift required the modification of the fabrication recipe used previously in the lab.[Hou12, Pan13] Nevertheless, the recipes remain quite similar. Therefore, in this section I will describe the fabrication procedure for Si/SiGe devices and make notes of where it differs from the fabrication for $Si/SiO_2$.

### 3.1.1 Operation Principle

The specifics of dot operation will be discussed in chapter 4. However, a short description of the operation is appropriate to give context to the fabrication steps. The full fabrication stack can be seen in figures 3.1 and a cross sectional view of the device through the formed dots can be seen in figure 3.2. A global accumulation gate, or top gate, made of aluminum and set at a positive voltage is used to form a conducting two-dimensional electron gas (2DEG) in a silicon quantum well embedded between two layers of insulating SiGe[1]. Placed in between the global accumulation gate and the 2DEG that it forms are the depletion gates. These gates, which are set at a lower voltage, screen the parts of the quantum well directly beneath them from the effects of the top gate and produce insulating regions, separating zones of the 2DEG into distinct electron reservoirs. The finest features of the depletion gates form the dot region by creating local minima in the electronic potential energy. Nearby to the region where the dots are formed

[1]Note that whenever I do not specify, SiGe refers to $Si_{0.7}Ge_{0.3}$

is a constricted conducting channel connecting a source and a drain electron reservoir. This channel's resistance depends on the electron occupation of the dots and, when biased, serves as the charge sensing channel.

The task of fabrication is to be able to connect electronically to the global accumulation gate, the electron reservoirs and the depletion gates.

### 3.1.2 The Wafer

Fabrication begins with a commercially sourced wafer with a Si/SiGe heterostructure, which itself is on top of a base silicon (100) wafer. The heterostructure is composed of 4 layers. The first layer, counting from the bottom, is a SiGe buffer layer. Second is an undoped, strained silicon quantum well of roughly 10 nm, in which the dots and electron reservoirs are formed. Third is a SiGe spacer layer of roughly 30 nm. Fourth is a thin, 2 to 5 nm silicon cap.

The first SiGe fabrication run was sourced from the semiconductor company IQE. The devices made from this wafer were used to obtain the results outlined in chapter 5. The second fabrication run used substrate that was donated to us by Jason Petta's lab at Princeton. There they had already done extensive characterization of the substrate, including SIMS to determine that the silicon quantum well was 50 nm deep. Further details of this substrate are layed out in a publication from their lab.[MHP15] (The wafer number we used was #16)

To confirm the properties of the heterostructure from the IQE wafer, and to image the interfaces between the regions, we used the Titan TEM at the Electron Imaging Center for NanoMachines (EICN) at the California NanoSystems Institute (CNSI). With the help of Billy Hubbard and Jared Lodicio, we used the STEM mode to image the layers of the substrate. First a cross sectional TEM sample of the wafer was made using the Nova 600 Focused Ion Beam available from CNSI. In doing this a protective sacrificial layer of metal is deposited above the cross section, as is visible in Figure 3.3a. Using the STEM mode the different layers of the heterostructure were easily visible, as can be seen in Figure 3.3b. We were then able to confirm the thicknesses of the SiGE spacer and the quantum well as being 30 nm and 15 nm respectively.[2]

[2]There were complications in obtaining the exact scale of the images directly from the TEM. However, due to

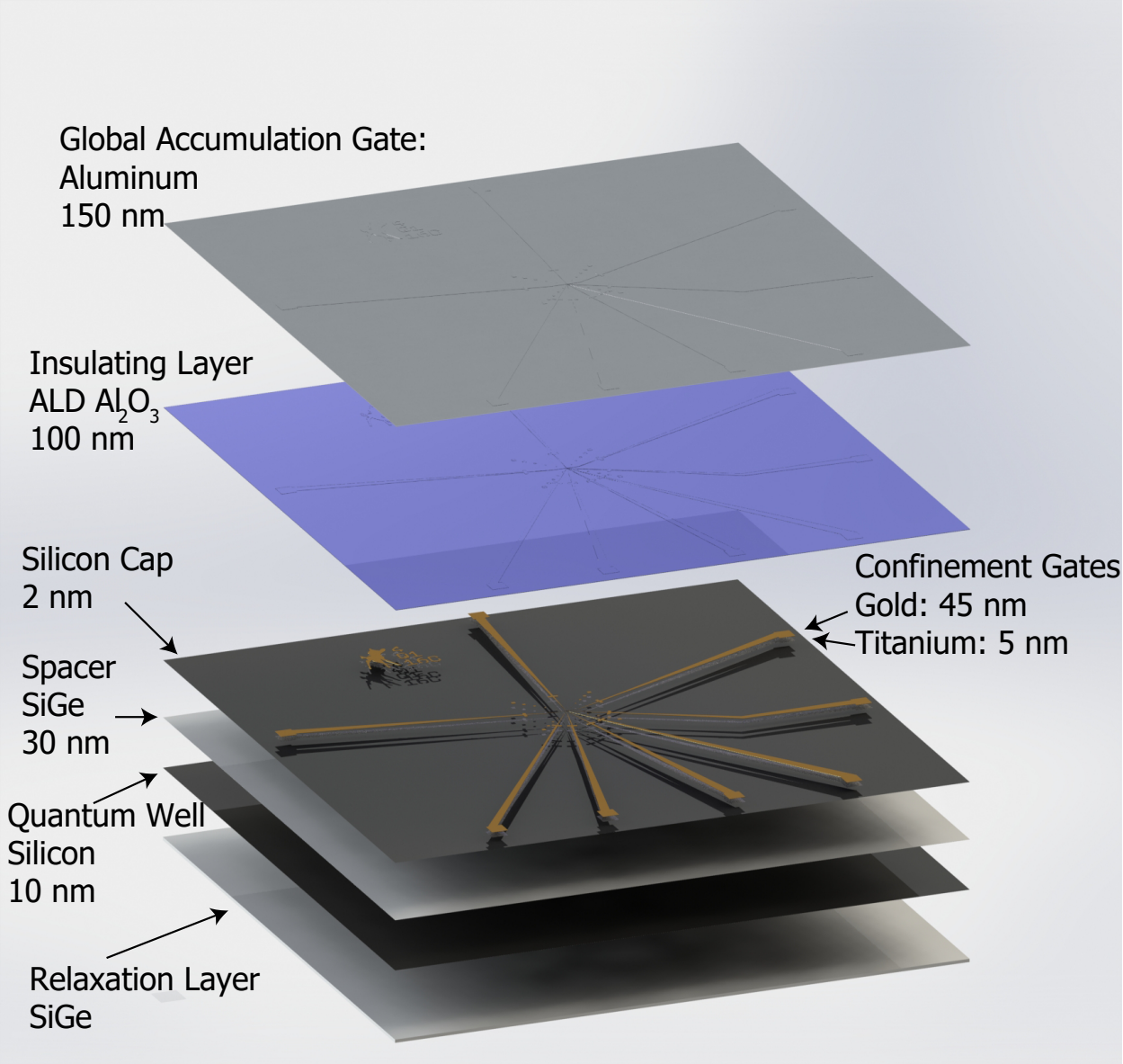


Figure 3.1: An exploded representation of the full fabrication stack of one of our SiGe devices.

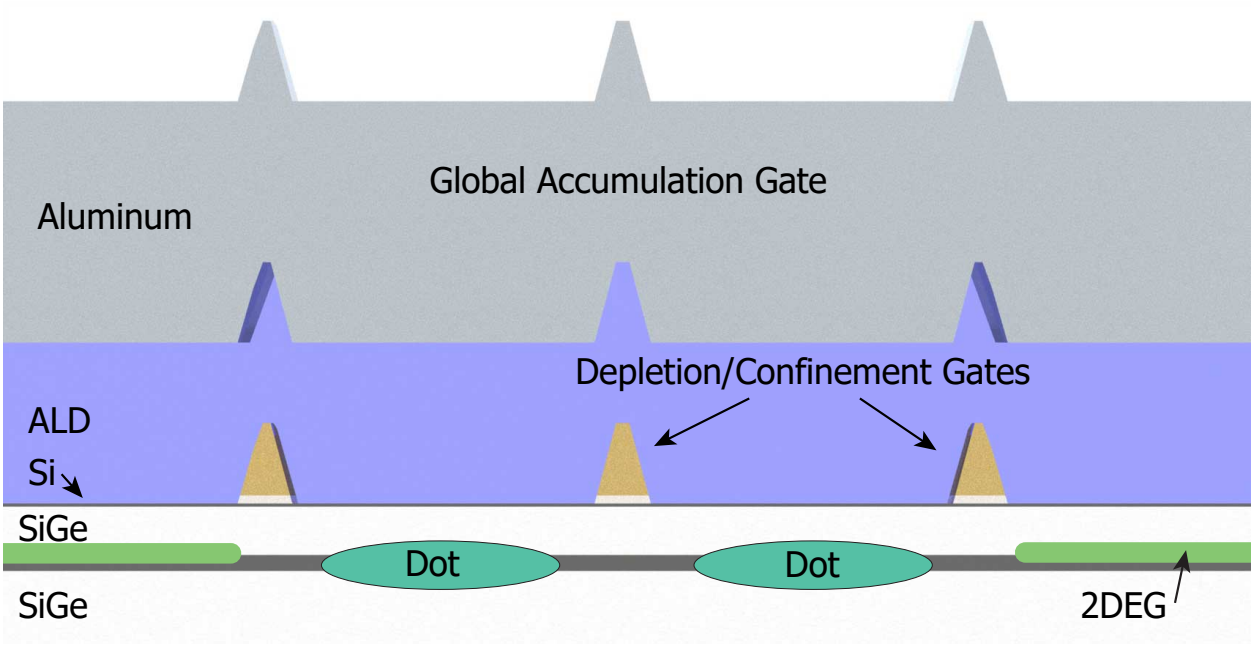


Figure 3.2: Device cross section through the location of the dots. Layers are shown to scale.

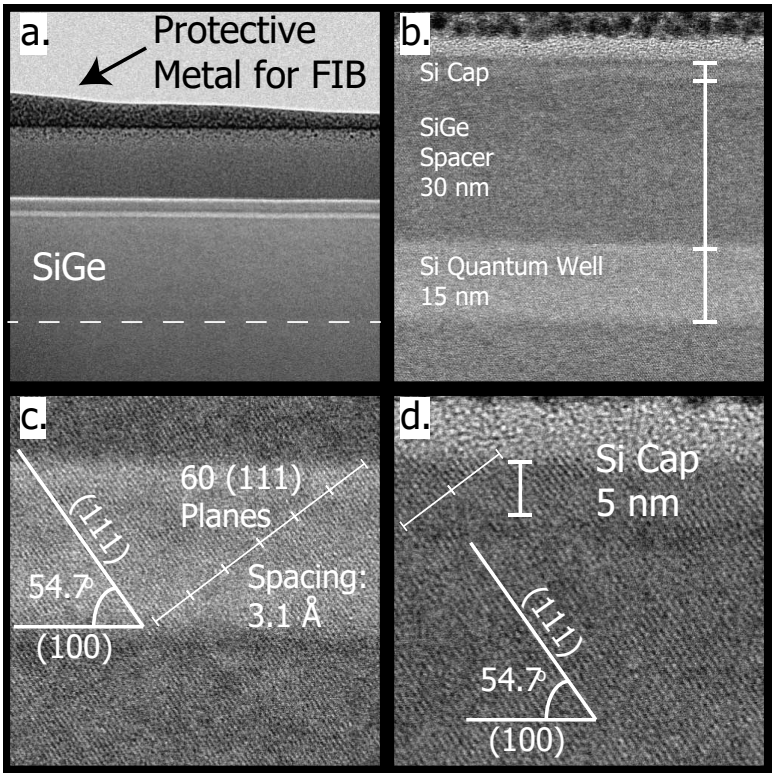


Figure 3.3: STEM images of the heterostructure in the lab. (a) Cross section with view of protective metal used to make the cross section (b) Close up of the layers (c) Detail of the quantum well with (111) silicon planes visible (d) Detail of the silicon cap

| | SiGe Run 1 | SiGe Run 2 | MOS |
|---|---|---|---|
| **QW Depth/Oxide Thickness** | 30 nm | 50 nm | 20 nm |
| **QW Thickness** | 15 nm | 8 nm | NA |
| **Si Cap Thickness** | 5 nm | 2 nm | NA |
| **Implantation Energy** | 25 keV | 30 keV | 17 keV |
| **Implantation Dosage** | $2 \cdot 10^{15}$ cm$^{-2}$ | $2 \cdot 10^{15}$ cm$^{-2}$ | $2 \cdot 10^{15}$ cm$^{-2}$ |
| **ALD Thickness** | 100 nm | 100 nm | 100 nm |
| **Depletion Gate Thickness** | 5 nm Ti /45 nm Au | 5 nm Ti /45 nm Au | 5 nm Ti /45 nm Au |
| **Annealing** | RTA 15 s, 700 °C | RTA 15 s, 700 °C | Furnace 20 min, 900 °C |
| **Alignment Markers** | Chrome | Chrome | Etched Oxide |
| **Wafer Source** | IQE | Lawrence Semiconductor | Wafer World |

Table 3.1: Summary of the different large fabrication runs.

### 3.1.3 Global Alignment Markers

The first step of fabrication done in our lab is to create patterns on the wafer which can be used for the alignment of subsequent steps. Where in Si/$SiO_2$ this was done by etching away the oxide layer, in our Si/SiGe process we do this with a metalization step. The patterns for the global alignment markers are made using photolithography in a single layer of photoresist. We then thermally evaporate roughly 100 nm of chrome using our in-lab evaporator and perform liftoff in acetone.

### 3.1.4 Ion implantation

The next step of fabrication is ion implantation. In order to make electrical contact to the 2DEG that will form the sources and drains of the device, the device is embedded with phosphorous ions. This creates doped regions of the substrate which are conducting irrespective of the top gate voltage. These regions extend from the 2DEG out beyond the part of the device under top gate to a place where ohmic contact can be made with a wire bond.

The patterns for the ion implanted regions are made using photolithography in a double

the atomic resolution of the Titan TEM, we were able to confirm the thickness of the silicon well by counting the visible (111) planes of silicon in the well. It is well known that in a silicon lattice, these planes lie at an angle of 54.7° to the (100) plane and that they have a separation from one another of 3.1 Å. Measuring the angle of the observed planes of rows to the (100) plane, we find the angle to be nearly exactly 54°, confirming that they were {111}. We were able to use these to confirm the thicknesses of the heterostructure layers.

layer of positive photoresist. The device is then shipped out for embedding with phosphorous ions, which are accelerated at the sample at an energy of between about 20 and 35 keV. The details of the implantation dosage and energy for each of the runs can be found in table 3.1.

### 3.1.5 High Temperature Annealing

Following the implantation, the crystal structure has sustained significant damage. The regions where the ions have been implanted are at that point visible to the naked eye. High temperature annealing, which involves subjecting the sample to a very high temperature, is used to repair the crystal. Without this healing step, it is very difficult to make good electrical contact with the 2DEG. This annealing step occurs in vacuum.

In the past our lab would use a furnace which would adjust its temperature over the course of many hours to achieve annealing temperatures of 900 °C. However, for the SiGe devices we switched to the use of rapid thermal annealing (RTA). The rapid annealer uses a lamp to increase the temperature of the wafer over the course of seconds, allowing precise control of the annealing time. We annealed at 700 °C for 15 seconds.

After RTA, the regions that were embedded with ions are no longer visible to the naked eye, indicating that the damage to the crystal has been repaired.[3]

### 3.1.6 Patterning of depletion gates

The next step is to pattern the depletion gates. These gates must begin at a scale suitable for wire-bonding and taper to a scale of a few tens of nanometers in order to form the dot region. Therefore, we use a combination of photolithography and electron beam lithography to achieve the desired results.

First the larger parts of the depletion gates are patterned using positive photolithography with a single layer of photoresist. Then using a CHA 40 electron beam evaporator at the UCLA

[3]One concern about this step is due to the use of chrome alignment markers. In general it is not allowed by clean rooms to include metal when performing high temperature annealing. We have tried to keep the temperature of the annealing below the sublimation point of chrome to prevent contamination of the annealer. But it is not yet certain what the long term effects of repeated fabrication will be.

NRF Nanolab facility, we deposit 5 nm of titanium as an adhesion layer and then 45 nm of gold. We then perform liftoff in acetone.

Next we extend these depletion gates to the dot region by doing electron beam lithography, which allows for a much finer resolution than photolithography. First, we spin a double layer of electron beam resist. The top layer is A2 PMMA and the lower layer is A4 PMMA. We then expose the resist to a focused beam of 30 keV electrons tracing out the desired pattern. This is done using our in-lab Hitachi S3000H scanning electron microscope and Nano-Pattern Generation System (NPGS) control software for patterning. When the exposed resist is developed in a solution of MIBK and IPA, the double layer forms an overhang where the top layer is less removed than the lower layer. This overhang will aid in liftoff. We then evaporate Ti/Au using the CHA and perform liftoff in acetone. The depletion gates are now complete.

### 3.1.7 Global Accumulation Gate

The final step is to add the global accumulation gate. This gate must be separated from the depletion gates so that they do not short. So prior to metalization, 100 nm of $Al_2O_3$ is deposited via atomic layer deposition (ALD) over the entire sample. This is a high quality insulator which will prevent leakage from the top gate to the depletion gates.

Then the global accumulation gate is patterned using photolithography. A 150 nm aluminum layer is then evaporated using our in-lab thermal evaporator and liftoff is done in acetone.

### 3.1.8 Etching and Ohmic Contacts

The final stages of fabrication involve making windows in the insulator and ohmic contacts to the ion implanted regions.

Following ALD, the ion implanted regions and the depletion gates are covered by insulator. Therefore, in order to reach them, windows must be etched in the ALD. The pattern for these windows is made in a double layer of photoresist using photolithography. Then a wet etch is

used to remove the $Al_2O_3$ from the regions exposed by the photolithography. [4]This is done with Transetch-N, which is heated to 180 °C and exposed to the sample for two intervals of 5 s. [5] When fabricating MOS devices, it was necessary to further etch away the $SiO_2$ with a buffered hydroflouric acid solution (BOE) to reach the silicon, because even doped oxide was not conducting.

The final step in fabrication is to dab indium solder onto the bonding area of the ion implanted regions. Indium solder makes relatively good ohmic contact. However, with the early devices, we noticed that many of the contacts were freezing out at low temperature. We hypothesized that this was because the SiGe spacer layer was acting like an insulator even when doped and it was therefore necessary to have direct contact with the silicon quantum well. We therefore began scratching the contacts with a diamond scribe immediately prior to applying the indium solder. This seems to have decreased the percentage of ohmic contacts that freeze out at cryogenic temperatures.

After fabrication is complete, we use A4 superglue to attach the sample to the holder and a West-Bond manual wedge style wirebonder to connect from the pads on the holder to the sample itself. Bonds are made to the contacts for the 2DEG and to the depletion gates.

## 3.2 Cryogenic Setup

Coherent control of quantum systems, at least at this current date, almost always requires the use of a cryogenic setup. A quantum system is made up of a collection of energy states, whose

[4]The step of etching the ALD used to come before depositing the global accumulation gate. This was mainly due to the use of a low temperature annealing in forming gas, which was supposed to repair the substrate to an extent following electron beam lithography. Performing this annealing step also had the effect of making the ALD resistant to etching. Therefore, the etching went before the final metalization. However, since we have noticed no improvement due to the forming gas step, we have moved the etching after metalization. This is because pinholes in the photoresist during the etching step can lead to pinholes in the insulating layer. If the top gate is deposited after the pinholes are created, then that can lead to a short. However, by putting the etch step after metalization, it reduces the risk of pinhole shorting by forcing the acid to etch away the top gate before reaching the insulator. Since the top gate has been etched away, there is no short even if the pinhole was directly above a depletion gate.

[5]We have found that this is an overly aggressive etch. This over-etches the windows with some frequency and often leaves stubborn photoresist which has been heated beyond the point of easy removal in acetone. Fortunately, our designs are robust to over-etching at this step and the stubborn photoresist appears to be easily removed by plasma ashing.

| Setup | Mechanism | $T$ (Typical) | Magnet | DC Lines | HF Lines | Turn time |
|---|---|---|---|---|---|---|
| $^3$He Sorbtion | Sorbtion | 300 mK | ±7 T | 16 | 2 | 1 Day |
| JDR-500 | Dilution | 120 mK | ±4 T | 32 | 4 | 2 Weeks |
| Oxford Triton | Dilution | 46 mK | No | 112 | 13 | 2-3 Days |
| 4K Probes | Soaking | 4.2 mK | No | 16-18 | 0 | 1 Hour |

Table 3.2: Summary of different cryogenic systems used in out lab. At the expense of using a magnet the Oxford Triton refrigerator allowed for a massive increase in the throughput of the the lab, resulting in qualitative differences in research.

energy gap plays a central role in the time evolution of the system. The environment will tend to induce random fluctuations on the order of $k_b T$, where $k_b$ is Boltzmann's constant and $T$ is the absolute temperature of the system. If $k_b T$ is greater than the relevant energy scale of the quantum system under control, and the quantum states are not somehow protected, then the environment has significant potential to destroy the quantum coherence.

As an example from our lab, a quantum system, whose coherent control will be detailed in chapter 5, had a minimum relevant energy scale of about 20 $\mu$eV, which corresponds to a temperature of 240 mK. (0.4 °F above absolute zero). The typical charging energy, meaning the energy required to load an additional electron into one of the dots tends to be around 0.5 meV, which corresponds to to about 5 K. Therefore, in order to conduct experiments at temperatures that allow for the manipulation of the relevant physics without the environment interfering, it is necessary to operate within a cryogenic setup.

Three different refrigerators were used in order to achieve the cryogenic temperatures needed to perform quantum experiments. I will discuss the capabilities and tradeoffs associated with each system and justify why the move to the Oxford Triton system allowed for a qualitative improvement in the investigation of these dot systems. A summary of the various systems is found in table 3.2.

### 3.2.1 $^3$He Sorption refrigerator

This is a top loading refrigerator from Oxford. It cools the sample by submerging it into a bath of $^3$He which has been cooled to 300 mK by lowering its vapor pressure. The vapor pressure

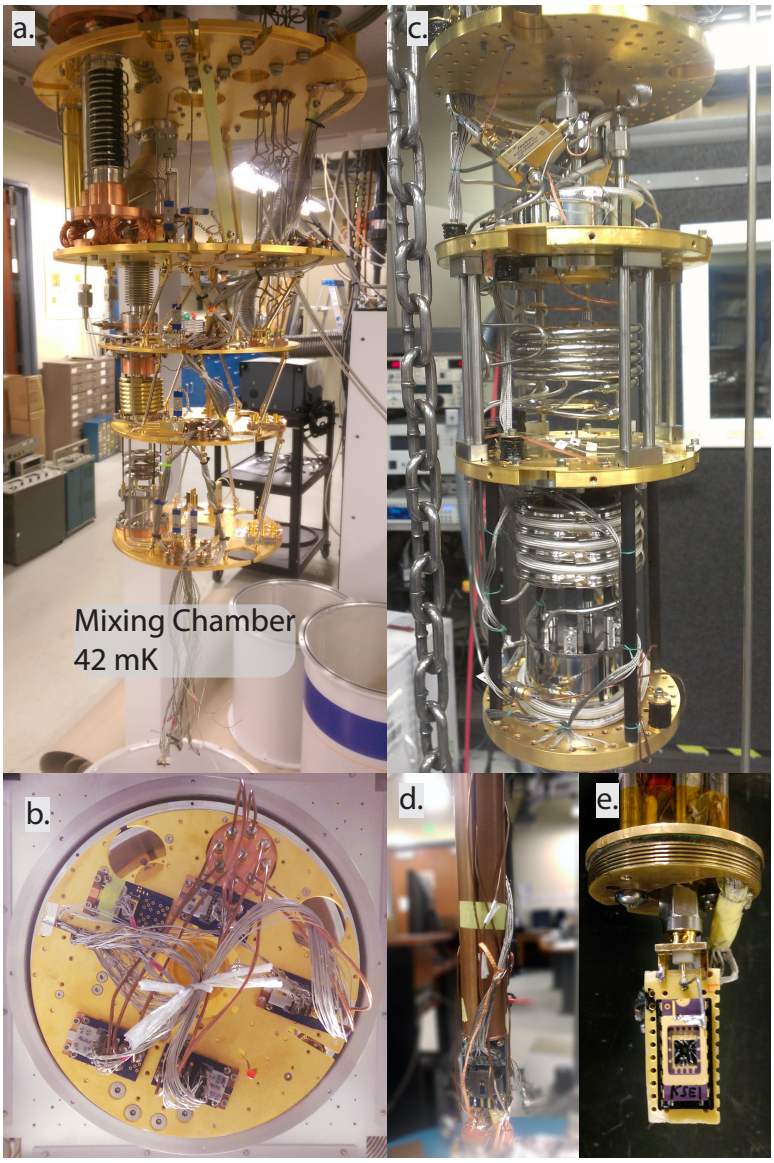


Figure 3.4: (a) The Oxford Triton dry fridge (b) its sample space; (c) JDR-500 (d) its sample space (e) Sorption Fridge sample space.

is kept low through the use of a so-called sorption pump, or sorb. The sorb is a high surface area device made of charcoal placed in the same chamber as the pool of helium. The sorb is in thermal contact with a 1 K pot, which uses a conventional pump to lower the vapor pressure of $^4$He and cause it to cool to 1K. The $^4$He gets to a higher temperature due to its higher latent heat. When the high surface area cools to this extent, it causes any $^3$He vapor in the chamber to condense onto the sorb. By removing the vaporous $^3$He, the effect is analogous to that of a conventional pump, and the vapor pressure of the helium pool is lowered. Lowering the vapor pressure leads to evaporative cooling of the pool, resulting in temperatures as low as 300 mK.

The primary benefit of this refrigerator relative to JDR-500 is that it only requires a single day to replace a sample. This allows for relatively rapid screening of devices. Another benefit of using a sorption pump rather than a conventional pump is that the pumping of the chamber does not induce further mechanical vibrations and the ensuing electronic noise. As a result, even though the temperatures are higher than those of the other two refrigerators, the raw data from this refrigerator is still often quite useful. This refrigerator is also outfitted with an electromagnet that is capable of producing up to 7 T, which can be used to investigate spin states of electrons within the quantum dots.

There are three major drawbacks to this refrigerator. The first drawback is that to cool this refrigerator requires a significant amount of liquid helium, which is expensive and increasingly difficult to source. The second is that its base temperature, while quite low, is still significantly higher than that of the dilution refrigerators in our lab. The third is that the sorption process is single shot, meaning that roughly every 24 hours the pool will have completely evaporated and the sorb must be heated to release the helium that has collected on its surface and to re-condense the helium into the pool. During this process the temperature of the sample will rise to at least 1.2 K. The dot occupation configuration is generally resilient to a rise in temperature of this magnitude. Nevertheless, this is a temperature sufficient to exceed most quantum energy gaps of interest since this corresponds to a thermal energy of 100 $\mu$eV, or a frequency of 25 GHz.

What is worse is that although this re-condensation process can be largely automated, in order to ensure that it is completed with sufficient efficiency to last a full 24 hours human intervention is often required, sometimes involving physically adjusting the probe. If the pool of $^3$He

completely drys up, then the temperature of the sample will begin to rise to room temperature. If the temperature rises to 4 K, is is nearly assured that even the electron configuration will be lost.[6]

In spite of its drawbacks, this fridge has proven itself an extremely capable machine. The capacity of this refrigerator is sufficient to screen a single device with either one or two high frequency control lines attached. Use of a cryogenic bias tee is not possible with our setup. The cooling fridge is permanently housed in the cryostat, but it is accessed with a probe, the sample space of which can be found in figure 3.4e.

### 3.2.2 Janis 500 Dilution Refrigerator

The Janis 500 Dilution Refrigerator (JDR-500), visible in figure 3.4c, uses a cooling mechanism that exploits a phase transition that occurs within a $^3$He-$^4$He mixture. This explained in more detail in the subsequent section 3.2.2.1. In contrast to the sorption refrigerator described in section 3.2.1, JDR-500 operates continually with a cooling power of 500 mW at 100 mK. The refrigerator is capable of producing even lower temperatures, potentially as low as 10 mK, if a second mechanical pump, called a Roots pump, is engaged to pump the still. The fridge is outfitted with a magnet that allows it to achieve fields of up to 4 T.

The device has one major drawback: the overhead per device tested is enormous. The fridge is outfitted with 36 DC lines and 4 semi-rigid cables for high frequency signals. This is sufficient to test two fully wired devices, as shown in figure 3.4d. In order to replace a sample, the shielding baths of liquid nitrogen and liquid helium must be removed or evaporated away. Without active pumping, this process may take several weeks to occur. Furthermore, during cool-down, liquid helium must be expended to chill the fridge from room temperature. This is expensive and time consuming. The result is that devices remained in the fridge for very long periods of time even if they were sub-optimal. Though once they were in the fridge, they required comparatively

[6] A potential improvement would be to switch control of the condensation and temperature monitoring process to a dedicated control computer rather than have it be controlled by the same machine that is used for experiments. This would allow for experiments to continue while the refrigerator is simultaneously monitored to see if a condensation process should be started.

little overhead relative to the sorption fridge.

#### 3.2.2.1 The Dilution Mechanism

The JDR-500 and Oxford Triton are both dilution refrigerators, which exploit a phase boundary between two differently concentrated solutions of $^3$He and $^4$He.[Pob07, BT15] One of the solutions, called the concentrated phase, is comprised almost entirely of $^3$He. The other, called the diluted phase in reference to its concentration of $^3$He, is composed primarily of $^4$He with a concentration of $^3$He of roughly 6.4 %. This boundary exists in a mixing chamber with the less dense dilute phase resting on top of the concentrated phase.

The binding energy of an atom of $^3$He is generally higher in a solution of $^3$He than $^4$He since atoms of $^3$He generally take up more space than atoms of $^4$He and when $^3$He molecules are surrounded by $^4$He they experience an attractive force to one another. Therefore, at the boundary between a solution composed of $^3$He and one composed of $^4$He, atoms of $^3$He will tend to migrate from the concentrated phase to the dilute phase. Counteracting this tendency however is the fact that $^3$He atoms are fermionic, meaning that as each additional atom of $^3$He joins the dilute phase, the Pauli exclusion principle pushes the energy of the next atom to join even higher as the Fermi level increases. Eventually the energy of an atom of $^3$He joining the dilute phase and concentrated equalize. The concentration at which this occurs remains finite all the way to $T = 0$, meaning that below a certain temperature, a mixture of $^3$He and $^4$He will spontaneously separate into one part nearly entierly composed of $^3$He and one composed of roughly 6% $^3$He.

By removing $^3$He from the dilute phase, atoms of $^3$He may be induced to transfer from the concentrated phase to replenish those taken. The enthalpy of $^3$He in the dilute phase is greather than it is in the concentrated phase, meaning that this transfer induces cooling. This process is analogous to the effect of evaporative cooling of a liquid in the atmosphere.

### 3.2.3 Oxford Triton Dry refrigerator

The Oxford Triton fridge, seen in figure 3.4b, was an important addition to the cryogenic capabilities of the lab. This system, like the JDR-500 system, is a dilution refrigerator, reaching temperatures as low as 16 mK prior to being outfitted with the DC lines and semi-rigid cables needed to control our systems. Following this wiring, the base temperature of the system rose to 42 mK, which we still believe to be significantly below our electron temperature with our current filtering strategy.

In total the fridge has 116 DC lines and 13 semi-rigid cables. This is enough to allow 5 fully wired devices to be tested at the same time. Furthermore, the sample space was quite large, as can be seen in figure 3.4b.

The major drawback to this fridge is that it currently lacks a magnet, and the addition of one would likely reduce its capacity to test as many devices at the same time.

### 3.2.4 4 K Device Screening and its Elimination

Prior to the purchase of the Triton system, due to the limited capacity of the $^3$He Sorption refrigerator and the JDR-500 Dilution refrigerator, the number of devices that could be examined in depth at cryogenic temperatures was limited. Furthermore, the percentages of completed devices that were fully functional was rather low. Therefore, it was necessary to set up a screening procedure to quickly select those devices which were functional.

Placing voltages across the depletion gates or ohmic contacts while the device was at room temperature was found to sometimes damage the device. Therefore, the screening procedure had to be cryogenic. And to test the strength of the individual depletion gates on the dot region it was necessary to go to at least the temperature of liquid helium, 4.2 K. Therefore, we used probes which were designed to lower the sample directly into a liquid helium Dewar.

However, the transfer of the sample from the screening holder, which was usually a 16 pin DIP since it was easy to prepare, to the holder suitable for millikelvin-scale cryogenic studies would often result in damage to the device. Furthermore, even though care was taken to lower

and raise the probe gradually the thermal cycling of the device was often quite sudden, exposing the device to stresses and moisture after it was tested. This raised the risk of the sample failing to perform at lower temperatures in the other fridges.

Once Triton was introduced to the lab, 4 K screening was phased out of the testing process. This is because the capacity of Triton was such that 5 devices could be cooled in a fully wired state at the same time. Since a fabrication run usually only produced up to 20 devices, this throughput was sufficient to combine the screening and in depth testing into a single cooldown. If the device was found to be good, it could be explored in depth immediately. As a result the bar for being considered a good device was raised and potentially damage inflicting steps were eliminated.

### 3.2.5 Sample Holder and Cap

Initially the sample holder used to house the sample during cryogenic testing was either a commercially available 16 pin dip or a machined piece of copper plated board. The 16 pin DIP was easy to wire-bond because the gold on the bonding pads was very soft. Furthermore, the standardized socket made mounting in the fridges relatively simple. However, such a holder was not appropriate for high frequency signals since cross-talk and attenuation was significant. The machined copper plated board, visible in figure 3.5a, was more suitable for high frequency signals. However, it lacked a grounding plane to reduce cross talk. Furthermore bonding directly to copper was difficult and the bonds themselves were unreliable. Therefore, indium needed to be placed by hand onto each of the areas where bonding was desired, as can be seen in figure 3.5b. Furthermore, wires needed to be directly soldered onto the board, which complicated the creation of new sample holders. Also a copper plate was soldered onto the back of the holder in order to make thermal contact with the fridge and to serve as the actual surface onto which the sample was mounted.

Early in my time, we decided to switch to the use of a traditional PCB design software and manufacturing to allow for increased flexibility in design and reliability. The first model of sample holder made in this way, visible in figure 3.5c, was similar in its layout to the machined

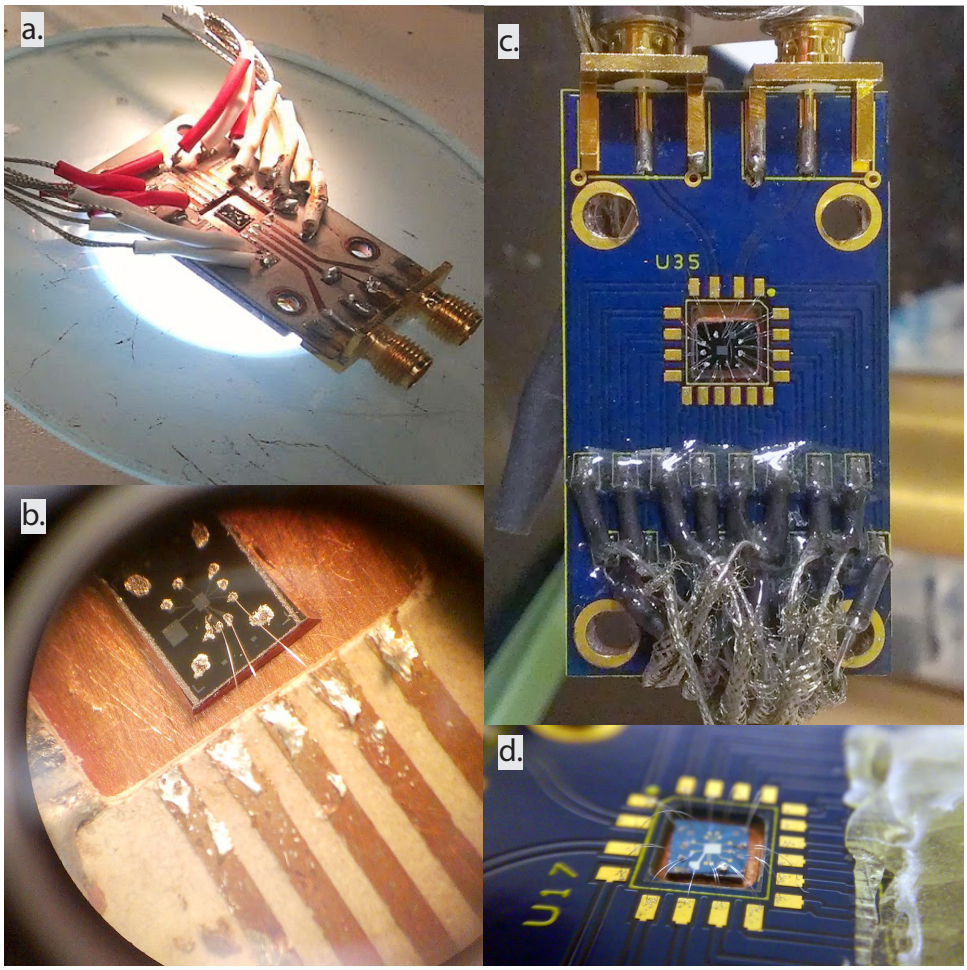


Figure 3.5: (a) Old Sample Holder, (b) Close up of bonding area on old sample holder (c) First sample holder made with standard PCB design techniques (d) Close up of bonding area with copper plate visible in cutout.

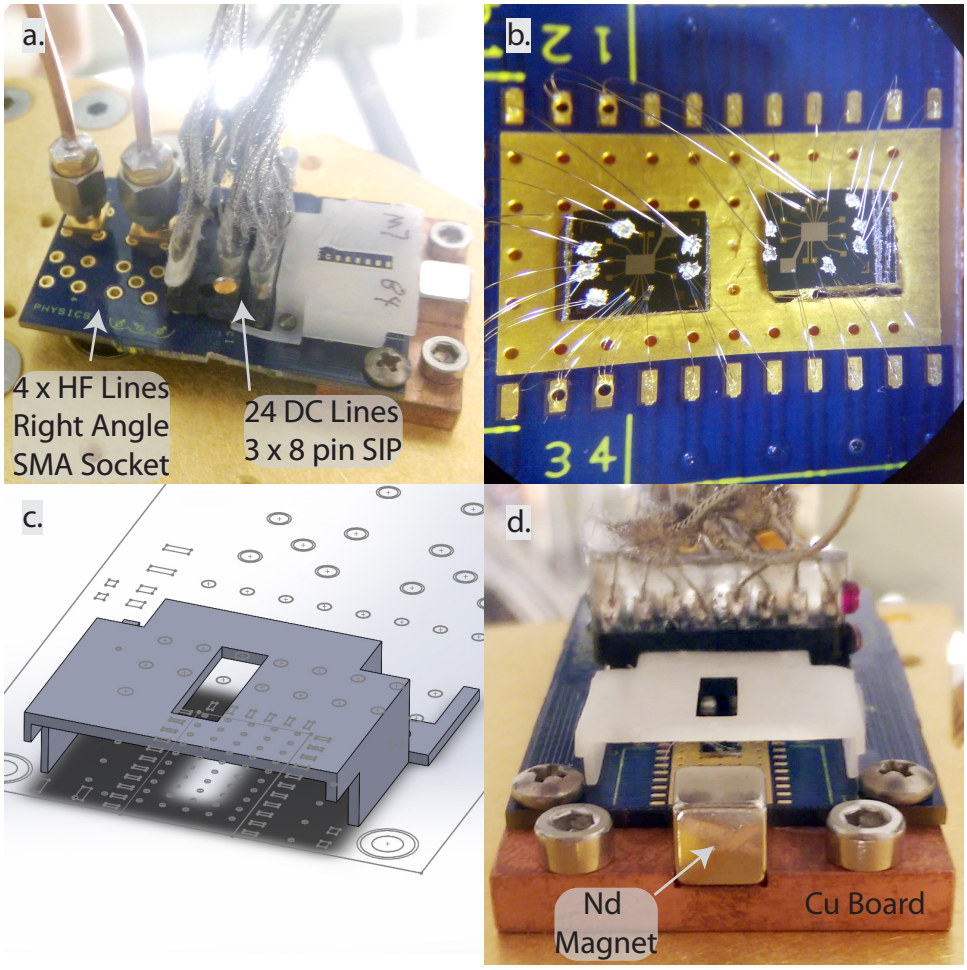


Figure 3.6: (a) Newest sample holder; (b) Close up of bonding area on new holder; (c) The CAD design used to 3D print the cap; (d) The placement of the copper board, permanent magnet and the PCB cap.

copper board. However, it had the addition of a ground plane to reduce cross talk as well as some optimization for trace width. It also had a solder mask to aid in board preparation. Furthermore, the bonding pads, visible in Fig 3.5d, were coated in nickel and gold, making them easier to bond to (though still not as easy as to the 16 pin dip). Even without substantial design changes, this was a major improvement in the time required to prepare the board and wire bond the sample. Though the continued use of direct soldering of stainless steel wire to the board still required a significant investment of time per board, and the use of epoxy made repairs difficult. Furthermore, the necessity to remove samples in order to free up boards added an additional step between screening and testing that led to the loss of several devices.

The next generation of sample holder, seen in figure 3.6a, was made with the goal of being the single holder to which a sample would be mounted for the course of its lifetime. Though this board turned out to be incompatible with the $^3$He sorption fridge, it was compatible with Triton and JDR-500. Furthermore, several changes were made to ease its use. Rather than stainless steel wire being directly soldered to the board, we added a socket to the board which could be used to plug in a separate adapter. Rather than permanently attach the copper plate, the board was made so that the plate could be attached and removed with screws, as can be seen in figure 3.6d. Also, high frequency capacity per board was increased from 2 SMA connections to 4 SMA connections and DC capacity was increased to 24 lines, as can be seen in figure 3.6b.

One major difficulty that was noted with the initial board was that the sample was directly exposed, so there was a large risk of bumping or breaking the wire bonds during handling. Therefore, in the most recent board design, we incorporated mounting holes for a protective cap. This protective cap was designed on the computer using SolidWorks, allowing the compatibility with the board to be assessed during the design phase, as can be seen in figure 3.6c. The cap was manufactured using a 3D printer, the Form 1+, using either the white or black standard resin. This has dramatically improved the reliability of the wire bonds, nearly completely eliminating the phenomenon of wire bonds breaking during handling.

### 3.2.6 Electron Temperature

Complicating discussion of a singular temperature associated with these experiments is the presence of a distinct electron temperature. The dilution refrigerators described above in sections 3.2.2 and 3.2.3 are capable of achieving temperatures on their mixing chambers well below 100 mK. Furthermore, the mixing chamber is a good conductor and is thermally well connected to both the device under test and the wires attached to it. However, this thermal connection most directly affects the phonon temperature in the materials. The electrical carriers making up the 2DEG in the device must couple to these phonons in order to achieve similarly low temperatures. Because of this, the temperature of the electron system is not exactly that of the surrounding material, and is instead higher.[MSB13] We have made measurements in some

of our refrigerators using our current setup and found the electron temperature to be roughly 150 mK.

Contributing to this elevated electron temperature is the fact that coupling between electrons and phonons are relatively weak in the device itself. Furthermore, the wires can heat the electrons by conveying the effects of radiation and thermal fluctuations via electronic noise. For this reason, many groups employ low pass electronic filtering in order to shield the device from these effects, lowering the electron temperature. For such filtering to work, the filtering must occur at a cryogenic stage and block the electronic signals originating from higher temperature regions. Our group has begun work on implementing electronic filtering at the mixing chamber stage in the hopes that it will improve our noise levels and electron temperature.

Further measures already taken in our lab to improve electron temperatures include the use of cryogenic bias tees for those lines which require both DC biases and high frequency signals to be able to pass. A bias tee is a simple circuit element which allows a DC bias voltage to be combined with a fast electronic signal through the use of a capacitor and inductor. The DC lines connected to the bias tee benefit from a block by the inductor which serves as a low pass filter. The high frequency line, which cannot have a low pass filter, is at least mechanically separated from the final node of the circuit by the capacitor in the bias tee. Therefore, when the bias tee is used at a cryogenic temperature it can reduce the heat load on the sample relative to doing such biasing at room temperature. It should be noted, however, that the results of chapter 5 were obtained without cryogenic biasing.

## 3.3 Electronic Control

### 3.3.1 Static Biases

Ubiquitous in our setup was the necessity for DC biases. These defined the voltages on the depletion gates as well as the accumulation gate and the source and drains of electron reservoirs. To provide these biases, the auxiliary outputs of a Stanford Research System Model SR830 Lock-In were used. They were transmitted to the device via stainless steel Cooner wire. Stainless steel

is a relatively poor thermal insulator, and therefore each part of it will tend to come into thermal equilibrium with its local environment. This means that the use of stainless steel in the wire as opposed to other metals with higher electrical conductivity aids in thermally isolating the portion of the wire connected to the sample from the portion of the wire which resides at room temperature.

### 3.3.2 Fast Pulses

The coherent quantum control of the systems under test sometimes required the application of rapidly rising pulses. To achieve this, we used the Agilent 81134A Pulse Pattern generator. It has 2 channels, each with two of outputs. Each output within a pair fires at the same time but with a different polarity. The generator outputs square pulses with picosecond resolution at a frequency ranging from 15 MHz to 3.35 GHz and a rise time of under 60 ps. The pairs also have a delay relative to one another which can be adjusted. These fast pulses were needed in order to induce the non-adiabatic transitions required for the experiments outlined in chapter5 and 6.

The slowest repetition time between individual pulses was set by the lowest repetition rate of 15 MHz. If the time between pulses needed to be increased, the mode could be switched from "pulse" to "data." In data mode, each cycle represents a bit in a string of data, where 1 is encoded as a pulse occurring within that cycle. Therefore, if the data string were switched from (11111111) to (10101010), that would represent a doubling of the repetition time. This can be necessary to reduce the effects of distortion arising from longer pulses.

### 3.3.3 Arbitrary Waveform Generation

Despite the speed and quality of the fast pulses which are generated by the Agilent 81134A, if a more complicated pulse was required, it was either impossible to accomplish or required the use of splitters to combine the outputs into a more complex pulse shape. Even in these instances it was only really possible to create two distinct voltage levels during the pulse. If a more complex pulse was required, an alternative was to use an arbitrary waveform generator. Such a device allowed for intricate pulse sequences at the expense of rise time and temporal resolution. We

developed a software framework for the scripting of classes of pulse sequences in an idiomatic way. These allowed for Rabi Pulses, Ramsey pulses and square pulses to be produced with the arbitrary waveform generators. In addition to the pulse shapes themselves, a binary marker could be set to output at programmable times within the pulse sequence. This feature was often used for triggering or chopping auxillary signals.

There were two different arbitrary waveform generators in the lab. The first was the Tektronics AWG 520. This machine had a sampling rate of up to 1 GHz with two independently programmable voltage channels. The second was the Tektronics AWG 610. This had a higher sampling rate of 2.6 GHz, but had only one independently programmable channel and an additional channel that output the same waveform but with an opposite polarity. Due to the limited storage capacity of both generators, a network file system was set up to allow for a large group of waveform files to be generated at the same time.

Sometimes this generator would be used in conjunction with a microwave generator in order to excite transitions in a dot. This involved having a slow pulse from the AWG superimposed with a microwave signal from a microwave generator chopped by the markers. To assure the synchronicity of the disparate pulse systems, an Agilent Infiniium 54855A oscilloscope, with a bandwidth of up to 6 GHz, was used to check the output and adjust the delays between the markers and the features of the pulses in the AWG in order to ensure that the total pulse was correct.

### 3.3.4 Current Measurements

The changes in current being measured through the charge sensing channel were almost always on the order of picoamps. When a DC current was being directly measured, a Stanford Research Systems 570 (SRS 570) current amplifier was used to amplify the current prior to measurement with a standard Keithley 2000 series multimeter.

This is a challenging measurement to make due to the noise in our system. To combat this, we employed a homodyne measurement using an SR830 in either current mode or in voltage mode after amplifying with the SRS 570. Such a measurement decreases the bandwidth

of the noise that the measurement is sensitive to by integrating the signal against a reference frequency. The Lock-In amplifier also produces an output voltage signal in phase with that reference frequency. In our most common setup this output voltage is used to directly perturb the system. The result of the lock-in measurement is then very sensitive to the effects of this perturbation. Most commonly, a depletion gate's voltage is perturbed and current through a nearby charge sensing channel is monitored for spikes indicative of an electron being loaded into or out of the dots.

However, when engaged in pulse related experiments, the reference output can be used to trigger the presense or absense of the pulse. This makes the lock-in measurement indicative of the pulse's effect directly. This is called "pulse-gated mode," and the two AWGs support it directly. The fast pulse must use a hardware switch to accomplish this same task.

# CHAPTER 4

## Basic Characterization of Quantum Dot Devices

In this chapter I will describe the basic measurements taken in the characterization of our quantum dot devices.

The device design which was used for the experiments detailed in this thesis can be seen in figure 5.1a. For reference, the side gates, which we often label metonymically by their voltages, and their designed purposes are as follows:

$V_L$, $V_R$ These are the plunger gates. They are designed to most directly affect the energy levels in the left and right dots respectively.

$V_{BL}$, $V_{BR}$ These are the barrier gates. They are supposed to regulate the tunneling rates to the electron reservoirs.

$V_T$ This central gate is designed to control the tunneling rate between the left and right dots.

$V_{WL}$, $V_{WR}$ These are the wall gates. They separate the dots from the charge sensing channel.

$V_Q$ This is the QPC gate, which regulates how constricted the charge sensing channel is.

Any side gate will effect all of these design objectives in some measure. Therefore, when the coupling was too great to be ignored, a multi-gate compensation strategy was deployed, as will be discussed in section 4.5. The QPC may be biased, leading to a current, $I_{\mathrm{QPC}}$. The dots may also be biased, leading to a current $I_{\mathrm{dots}}$.

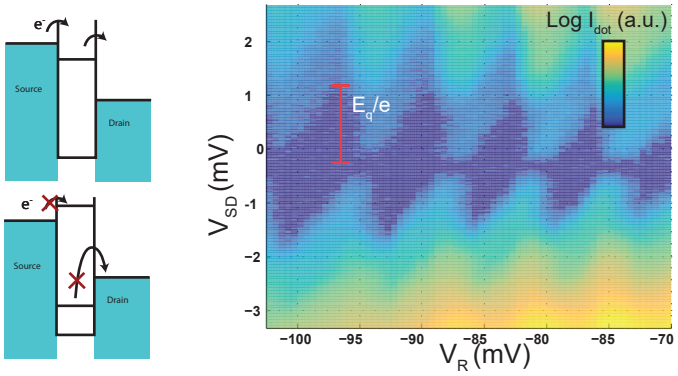


Figure 4.1: Schematic of electron transport through a single dot when placed under a bias $V_{SD}$.

## 4.1 Dot transport and Coulomb Blockade

One of the ways that quantum dots may be explored is to examine the transport of charge carriers (either electrons or holes) through them when a bias is put on the electron reservoirs that they are adjacent to. When this happens the transport signatures give insights into level structure and charging energy of the dots. When pulses are applied, spin blockade can even be observed directly using transport measurements.[HRX14] One of the main measurements that can be taken with single dot transport measurements is the calculation of the charging energy, $E_q$, and lever arm, $\alpha$, which is the constant of proportionality between the voltage applied to a side gate and its effect on the energy level of the electrons in a dot. Both of these measurements may be obtained from the so-called coulomb diamond plot, an example of which is shown in figure 4.1.

The height of the internal diamonds, as marked in figure 4.1, is a direct measurement of the charging energy, since it is precisely when the bias between the reservoirs is greater than the energy spacing that it will be impossible for there not to be at least a single state into which the state can temporarily transition. Once the charging energy is known, the slope of the diamond may be used to determine $\alpha$.

Transport can also be conducted in double quantum dots. Again the criterion for whether transport can occur is whether there are available states for charge carriers that are between the source and drain Fermi levels in energy. However, with double dot systems, it is also necessary

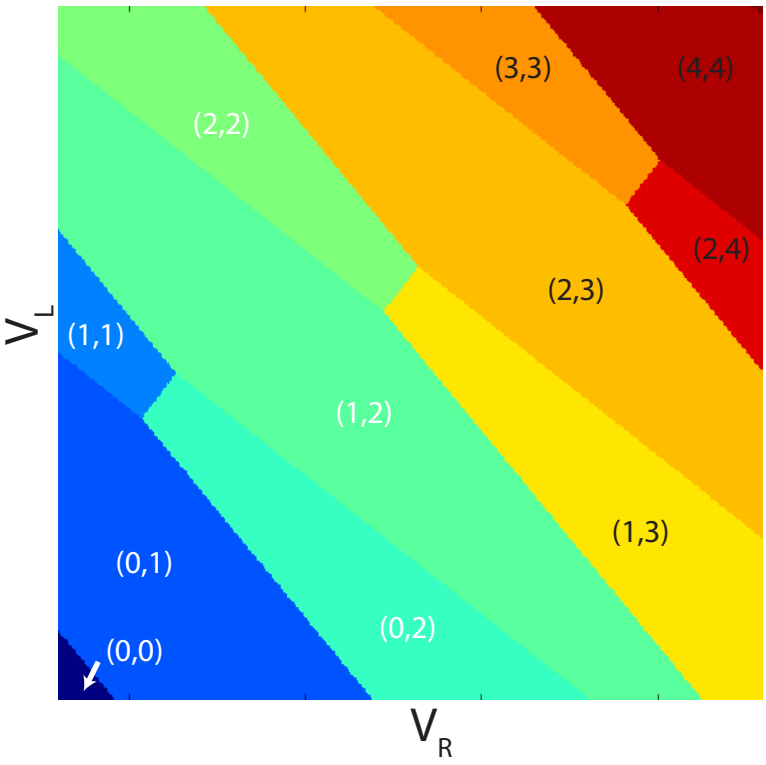


Figure 4.2: A simulated example of a stability diagram for a double quantum dot system. If charge sensing were made using direct mapping of $I_{qpc}$, then the result would resemble this figure.

for transport that the charge state's energy consistently decreases as the carrier moves through the dots. The energy levels must cascade from high to low during transport, as seen in figure 4.2a. If one of the charge states is higher than the previous one, then that will cause a blockade. This blockade can actually be the basis of spin readout.

## 4.2 The stability diagram

By sheer numbers, the most common plot made in the characterization of quantum dot devices is the stability diagram. This is a diagram that maps out the occupation number of each of the dots as a function of side gate voltages. Such a diagram is of great utility. From it, the rough location of the dots can be deduced and it allows us to configure our devices at the cusps of the charge transitions which are required to operate the device as a qubit.

Usually, we refer to the occupation state of a given dot system by a tuple of length equal to the number of dots. For example in a two dot system, if there is one electron in the left dot and two in the right dot, we refer to that as being in the (1,2) state.

Within a stability diagram there will be regions defined by different occupation numbers. The slope of the boundary between regions contains information related to the location of the dot whose occupation number is changing. The closer the side gate is to the dot, the more densely the charging lines for that dot will be spaced in the voltage of that side gate. If there is a single dot, then the stability diagram will be represented by a series of parallel regions. If there are are two dots, then the structure of the stability diagram resembles a honeycomb. Beyond that, the diagrams increase in complexity, as they represent a higher dimensional structure of which a 2D cut is being taken.

Furthermore, the stability diagram can be used to search for the effects of voltage pulses by comparing a stability diagram taken without a pulse on and one with a pulse on. This can reveal interference regions, such as will be presented in chapter 5.

An example of a theoretical stability diagram for a double dot, obtained via the method outlined in section 4.2.1, can be seen in figure 4.2. Also, similarly to the single dot case, this type of measurement may be used in order to extract the different lever arms between the various dots and side gates.[HPX11]

### 4.2.1 Transition Balancing Model

To obtain the stability diagram representing the time-averaged charge occupation at a non-zero temperature, a transition balancing model may be used (following [NLN13]): If the probability of being in a given charge configuration state is $P_a$, then

$$\frac{dP_a}{dt} = \sum_{k \neq a} \Gamma_{k \to a} P_k - \sum_k \Gamma_{a \to k} P_a,$$

where $\Gamma_{a \to b}$ is the dot transition amplitude. If we know the transition amplitudes. We can then impose the conditions that at equilibrium $\frac{dP_a}{dt} = 0$ in order to solve for the probabilities. It is a

matrix equation with $M\vec{P} = 0$, where

$$M_{ab} = \begin{cases} \Gamma_{b\to a} & a \neq b \\ -\sum_k \Gamma_{ak} & a = b \end{cases}.$$

The null space of this matrix represents the equilibrium probability vector . As a form for the transition amplitudes, we may take $\Gamma_{a\to b} = t_{ab} \cdot f\,(\mu_a - \mu_b)$, where $t_{ab}$ is a tunnel coupling between states $a$ and $b$ (which is symmetric in the states), $f$ is the Fermi-Dirac function, and $\mu$ is the chemical potential of a given charge state. The difference, $\mu_a - \mu_b$, turns out to be the difference in system energy between the two states. To get the energy of the states, a network of conductors representing the dots, 2DEGs and side gates, connected by capacitors may be used. (This widely used and is outlined in detail in [HKP07])

An example of a time when a non-equilibrium charge sensing diagram is useful is when one wishes to see the effect of transport through the dots on a charge configuration. The calculation for such a system is in figure 4.3. Visible are the biasing triangles, the regions in voltage space where current may flow from the source to the drain.

## 4.3 Charge Sensing

Charge sensing techniques are widely used to measure the charge states of nano-scale systems such as quantum dots. Such techniques work by creating a current channel which passes very close to a system where one wishes to detect changes in charge configuration and occupation. Such a channel is designed to have a conductance with very high sensitivity to changes in local electrical landscape, meaning that changes in the adjacent charge configuration produce a sudden and measurable change in the current through the channel. Charge sensing channels are often realized as either a Quantum Point Contacts (QPC) or, more recently, as Single Electron Transistors (SET).

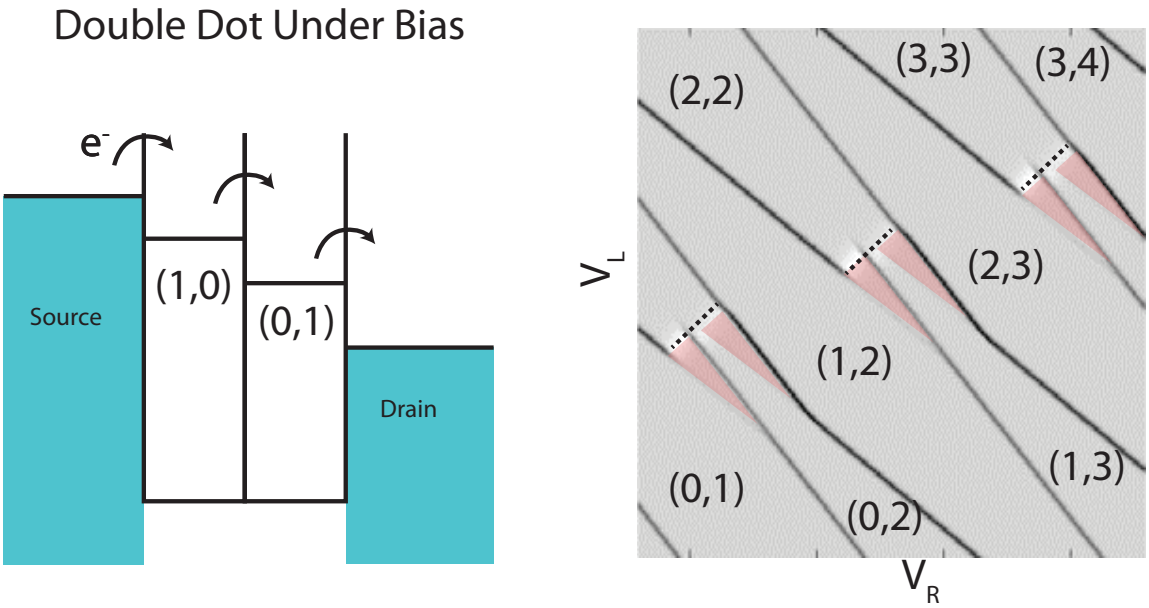


Figure 4.3: (a) A diagram showing the transport of electrons through a double quantum dot. The transport of holes proceeds similarly. (b) A simulation using the tunneling rate model with biasing triangles where current can flow highlighted in red.

### 4.3.1 DC Transport Measurement

The most straightforward way to perform charge sensing is to record the DC current flowing from the source to the drain of the QPC. To start, a bias voltage, $V_{SD}$, is applied between the source and the drain of the QPC. The side gate whose purpose is to regulate the constriction of the sensing channel, and whose voltage we term $V_Q$, is adjusted so that it is maximally sensitive to changes in its environment. In reality, at its most constricted point the QPC is more dot-like than 2DEG like. When $I_{QPC}$ is mapped out as a function of $V_{SD}$ and $V_Q$, there is clear evidence of coulomb blockade, just as can be seen in figure 4.1. The point of maximum sensitivity is at the sides of one of these coulomb diamonds.

If a stability diagram were to be taken via $I_{QPC}$ directly, the plot might look something like what is seen in figure 4.2. This is known as a wide-band measurement. However, we tend to see that such a measurement has poor signal to noise ratio, as can be seen in figure 4.4a. The direct coupling of the side gates to the QPC leads to the introduction of a significant background. Furthermore, the noise level is too great and we have found odd systematic artifacts

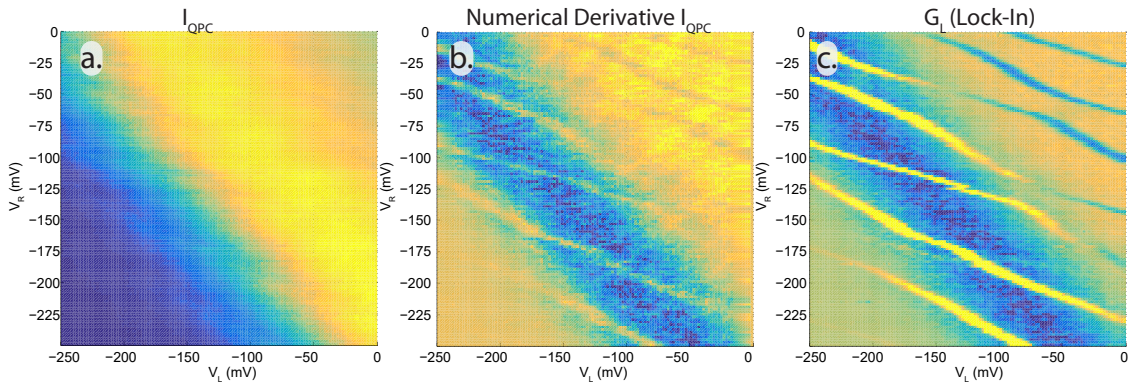


Figure 4.4: a) A direct readout of the charge sensing current, also known as a broadband measurement and b) its transconductance, $G_L$, taken by a numerical derivative. c) A measurement of $G_L$ taken using the real part of a lock-in signal.

in our DC measurements. Taking a numerical derivative as in figure 4.4b improves the clarity somewhat, but the noise level is still high.Therefore, we almost exclusively make use of lock-in transconductance measurements.

### 4.3.2 Transconductance Measurement

Due to the difficulty in discerning the charge sensing signal using DC transport through the QPC directly, the most common form of charge sensing measurement was a lock-in measurement of the transconductance, $G \equiv \frac{dI_{QPC}}{dV_g}$. The transconductance is a measure of the sensitivity of current through the charge sensing channel to changes in the voltage of a single side gate. There is always a contribution to $G$ from the direct capacitive coupling of the side gate to the QPC. However, when the system is at the cusp of a charge transition, the slight change in side gate voltage will also cause the loading or unloading of an electron. When that happens, there is a sudden effect on the QPC signal and a spike or dip in the transconductance. The transconductance is measured via an SRS 830 Lock-in amplifier. The results of such a measurement can be seen in comparison with a direct current measurement in figure 4.4c. The hardware setup for such a measurement is sketched in figure 4.5.

In addition to being applied to a single gate, the excitation may be applied simultaneously to two gates. This may be necessary if coupling to one of the dots is too low from one of the

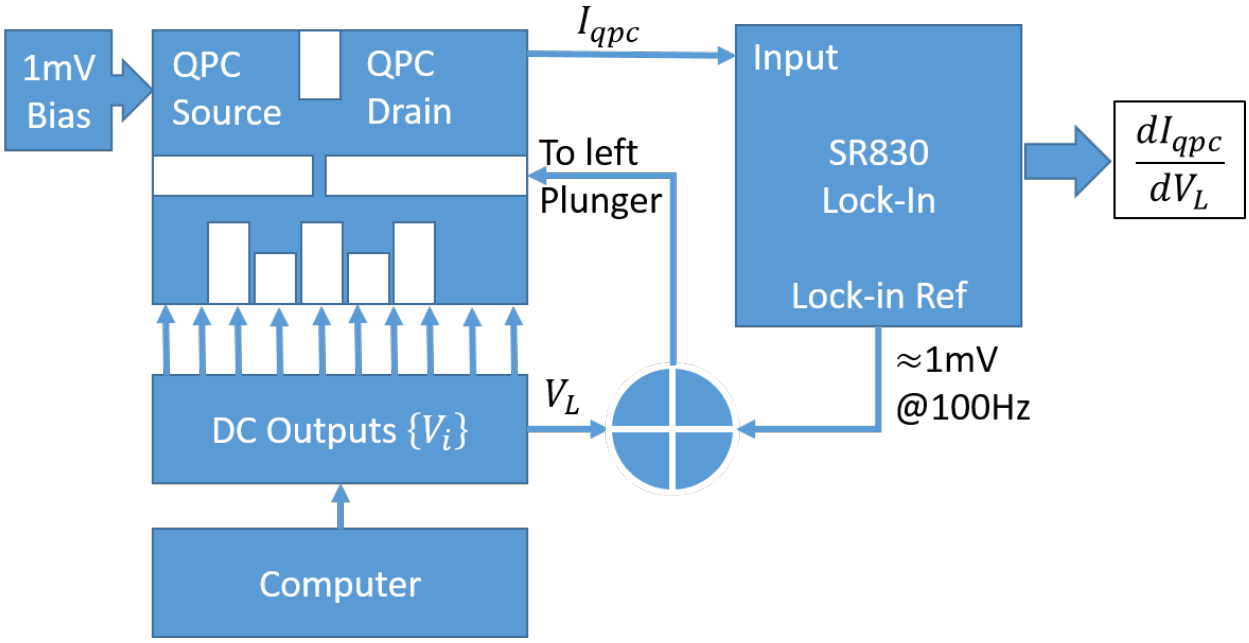


Figure 4.5: The electronics setup describing how the transconductance measurement is made and where the control computer is used.

side gates to make a visible charging line. Furthermore, depending on whether these excitation signals are in phase or out of phase with one another, one can enhance different aspects of the stability diagram. In figure 4.6a, the data was taken using a symmetric excitation, allowing $V_L$ and $V_R$ to be oscillated in phase. As a result, we term what is measured $G_\delta = \frac{dI_{QPC}}{dV_\delta}$, where $V_\delta \equiv V_L + V_R$. The charging lines are both the same color and the line representing the middle dot is quite robust. However, since both of the dots are having their energy levels raised in phase, electron transitions between the dots are less induced, leading to an almost non-existent inter-dot transition line, as can be seen in the circle. However in figure 4.6b, an anti-symmetric excitation was used, measuring $G_\varepsilon \equiv \frac{dI_{QPC}}{dV_\varepsilon}$, where $V_\varepsilon \equiv V_L - V_R$. This has the effect of enhancing the inter-dot transition line. However, since there is a middle dot in this diagram, and it is being equally and oppositely affected by the two side gates being excited, the middle dot charging line is nearly invisible. Another benefit of the anti-symmetric excitation is that the net capacitive effect from the excited side gates on the QPC, which is centrally located in our devices, is minimized. This makes the background level of $G_\varepsilon$ much closer to zero than $G_\delta$. Furthermore, whether dots are to the right or to the left may be distinguished by whether

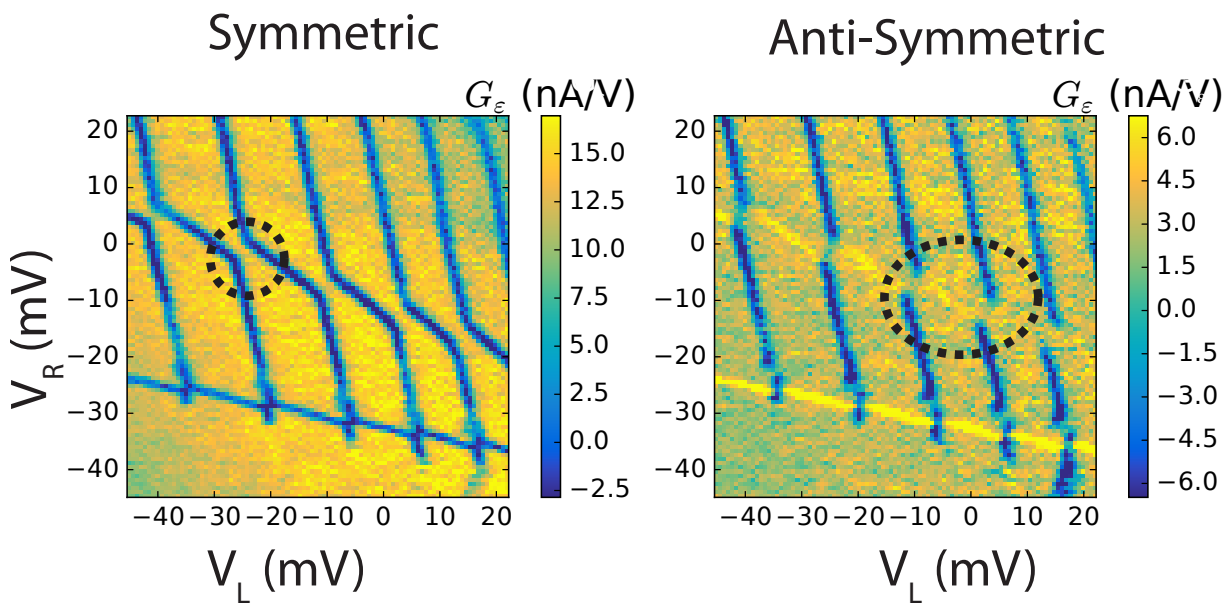


Figure 4.6: A stability diagram taken with (a) a symmetric excitation and (b) an anti-symmetric excitation, with the difference in inter-dot line clarity highlighted.

they are peaks or dips from the background level of $G_\varepsilon$. As can be seen, with the symmetric excitation all of the dots result in the same qualitative effect on $G_\delta$, and position can only be determined within a single dimensional scan by observing the magnitude of the effect, not the sign.

## 4.4 Accumulation Procedure

### 4.4.1 Simultaneous Transport and Sensing

When performing the initial accumulation of MOS devices, it was common to take I-V curves to determine the point at which the charge sensing channel began to turn on. We found that this I-V curve was very repeatable and gave good insight into when the 2DEGs were accumulated and the QPC channel became conductive. However, the heterostructure of the SiGe devices had challenges associated with accumulation which were not encountered in MOS.

The range of top gate voltages between that which would lead to completely empty dots and that which would result in a loss of confinement may occasionally be quite narrow. This

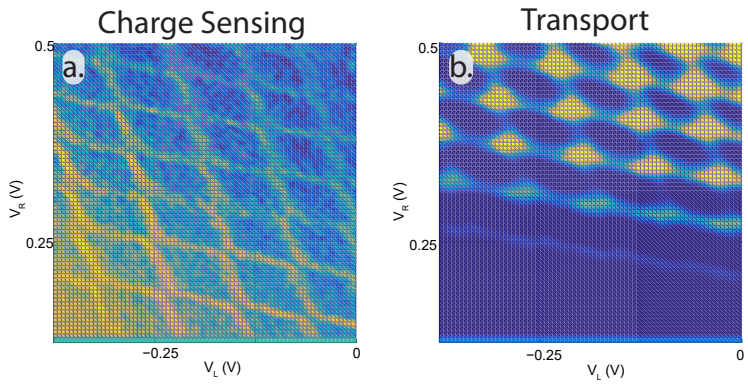


Figure 4.7: (a) A lock-in measurement made during initial characterization revealing a double dot system; (b) a direct measurement of current flowing through the double dot system made simultaneously

means that when performing initial accumulation, a problem that is sometimes encountered is that, due to lack of a clear charge sensing signal, a given top gate voltage is perceived as not having accumulated electrons into the dots when in fact the voltage was already so high that confinement has been compromised. If as a result of this mistaken belief excessive top gate voltages are applied, the device may be irreparably damaged. But, even short of permanent damage, as other groups have noted, if the top gate is pushed beyond a certain saturation point, charge will accumulate in the layer between the SiGe spacer and the silicon cap. [Wan14] This charge serves as a screening layer for the silicon well. This means that if the device needs to be accumulated again, the turn-on voltage will be even higher. [1]

To counter this risk, particularly at the initial stages of tuning, it can be useful to perform simultaneous charge sensing and dot transport measurements. Transport through the dots necessarily entails the presence of energetically available states in the dot. At the lowest accumulation gate voltages which allow transport, we find that the side gates are usually within range of a well tuned charge sensing region. An example of simultaneous charge sensing and dot transport can be seen in figure .

[1] A remedy which we began taking was to set the top gate voltage to a negative voltage for some amount of time. Sometimes this procedure had a revitalizing effect on the devices, though the success rate was far from perfect.

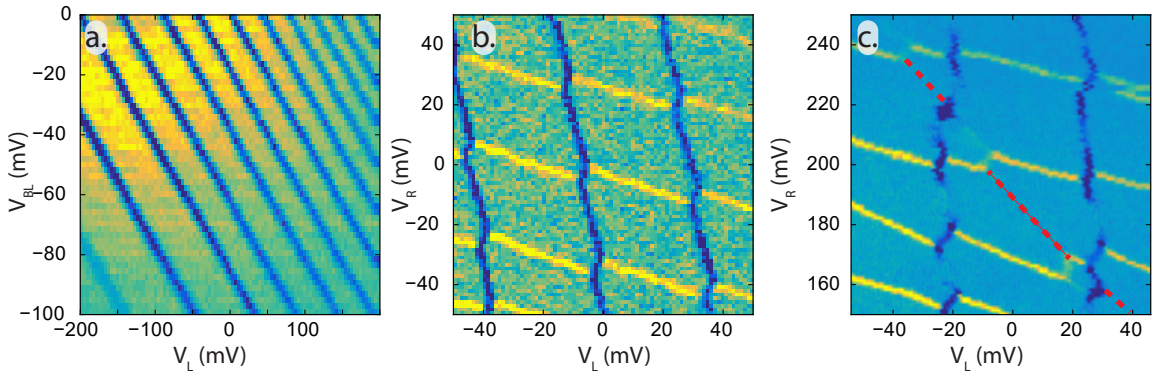


Figure 4.8: Three different charge configurations formed using the same device on the same cooldown. (a) single dot; (b) double dot; (c) triple dot, with the third dot's line accentuated with a red dotted line. Primarily, $V_T$ is used to transition between these regions.

### 4.4.2 Single, Double and Triple Dot modes

The gate $V_T$ has a primary purpose of increasing the tunneling rates between the dots. But during rough characterization, it may serve to tune the entire device between regions behaving as either a single, double or triple dot device. At high voltages, the left and right dots combine to form a single dot, as in figure 4.8a. At intermediate voltages, two dots, one on the left and one on the right are formed, as in figure 4.8b. And when the voltage is low enough, the lines become less regular, and almost always a middle dot forms, as in figure 4.8c.

## 4.5 Vector Based Control and Compensation

Here I discuss the efficacy of a vector-based approach to device tuning and passive sensitivity compensation of charge sensing channels. We find such passive compensation to be effective at maintaining sensitivity of these channels over a range of plunger gate voltages. I will also demonstrate the use of the framework it provides for efficiently and idiomatically tuning devices by using it to adjust the inter-dot coupling of an individual double-dot triple point.

### 4.5.1 Compensation in quantum dots

Qubits composed of a single dot, a double dot, and even a triple dot [MBT13a, MBT13c] have been proposed and demonstrated. As the the number of dots considered has increased, so too has the potential parameter space to be explored during tuning, as well as the potential for many side gates acting together to de-sensitize ajacent charge sensing channels with their stray fields.

In order for lateral quantum dots to be useful, it is necessary to have the ability to control and measure the charge configurations within the dots during both operation and tuning. Charge sensing channels of both QPC and SET types have been used heavily in order to access the charge states of such devices.

However, the same strong dependence to the local electrical environment that makes such channels effective measurement devices for charge sensing also make them vulnerable to losses of sensitivity caused by changes to the very experimental parameters which are under study, such as side gate voltages.

To deal with the problem of side gate induced de-sensitization of charge sensing channels, systems of compensation, either dynamic[YLZ11] or passive[BER15], are sometimes employed, where the effect of one gate is compensated for by a countervailing effect from another gate.

Here we describe the implementation and efficacy of a control framework for making changes to multiple experimental parameters such as side gates, where the total change is considered as the vector sum of several basis changes of differing magnitude. This framework allows for the agile traversal and slicing of large parameter spaces in a way not possible without some way of mathematically combining the effects of two changing experimental parameters, which nevertheless are composed of overlapping physical parameters. In this framework, first order passive compensation is achieved through the traversal of a well tuned subspace where sensitivity is kept constant by scanning components in a user defined basis of that subspace. We also demonstrate the framework's utility in the tuning and operation of quantum dot systems in both Si/SiGe and SiMOS heterostructures. Finally, we discuss the utility in allowing for control parameters to be specified in keeping with the idioms of theory.

### 4.5.2 Vector Control Software

The core notion of a compensation scheme is that the system begins in a well tuned state and any changes to a single parameter in general require compensation from another parameter in order to keep the tuning figure of merit constant. If the goal is to maintain the sensitivity of a QPC/SET, then the figure of merit is usually the differential conductance through the measurement channel. In dynamic compensation, a tracking measurement correlated with the figure of merit, such as the total current through the QPC/SET, is constantly monitored after each perturbation to the system and an adjustment is made in real time to the compensating parameters in order to keep the figure of merit within an acceptable range. Such systems employ active feedback and parameter estimation, which allow them to adjust to abrupt changes in the state of the device, including changes due to events unrelated to the variables being changed by the experimenter.[YLZ11] Furthermore, such a system has the ability to adjust to the changing of many interdependent parameters built in.

However, there may be times when the use of such an active feedback system is not viable, either for reasons of hardware availability, setup simplicity or experimental necessity. In such an instance, the ability to perform passive compensation could still prove valuable to the experimenter. However, as the interdependence of the parameters grows, it becomes necessary to be able to take into account the compensation required by a combination of changes, whose cumulative effect may be greater or smaller than either of the individual changes in isolation.

In the system we describe here, the well tuned state away from which the system is being perturbed is defined as the origin of a vector space. The vectors of this space are given by deviations of the adjustable physical parameters away from this well tuned spot. For example, suppose there are three externally adjustable parameters, $V_R$, $V_L$ and $V_Q$, and a well tuned state, $O$, where $\left(V_R, V_L, V_Q\right) \rightarrow \left(V_{O,R}, V_{O,L}, V_{O,Q}\right)$. Further suppose that one wishes to perform a scan where $R \equiv (V_R - V_{R,O})$ and $L \equiv (V_L - V_{L,O})$ take the values of $\{R[x], L[x]\}$ where $x$ is the index of the scan step. Note that, often times the scan may be decomposed into two dimensions, where one of the gates is scanned along the quick axis and the other along the slow axis.

For an uncompensated scan, at step $x$, then

$$\begin{aligned} V_R[x] &= R[x] + V_{O,R} \\ V_L[x] &= L[x] + V_{O,L} \\ V_Q[x] &= V_{O,Q} \end{aligned}$$

If we now define a vector space of voltage, maintaining the same ordering as before, we can re-write the above update functions as

$$\vec{V}[x] = R[x]\,\vec{\Delta}_R + L[x]\,\vec{\Delta}_{b_L} + \vec{V}_O,$$

where $\vec{\Delta}_R = (1,0,0)$, $\vec{\Delta}_L = (0,1,0)$ and $\vec{V}_O = \left(V_{O,R}, V_{O,L}, V_{O,Q}\right)$.

#### 4.5.2.1 Physical Parameter Vectors and the State object

A physical parameter vector is defined over the space of physical parameters $\{V_i\}$, where $i$ indexes the available physical parameters to change. These vectors, which are the generalization of the $\vec{V}$ and $\vec{\Delta}$ objects defined above, obey the standard rules for elements of a vector space, including closure under scalar multiplication and vector addition. The creation of such objects allows for the easy expression and computation of the ideas outlined in the last section.

A state object contains an origin, $\vec{V}_O$, a set of $N$ scalar scanning parameters $\{p_n\}$, and a set of physical parameter vectors representing the deviations from the origin associated with each scanning parameter, $\left\{\vec{\Delta}_n\right\}$. At each scan step $x$, the state object then computes what each physical parameter $V_i$ must be in terms of the scanning parameters and the deviation vectors:

$$\vec{V}[x] = \vec{V}_O + \sum_{n=1}^{N} p_n[x]\,\vec{\Delta}_n$$

Note that this update function is independent of any event at $x-1$. For this reason, subsequent equations will omit the explicit dependence on $x$.

### 4.5.3 Use in conjunction with QPC/SET

The assumption of using such a compensation system for QPC/SET tuning is that the set of appropriately tuned states in parameter space is well approximated by a plane for a useful region around the well tuned point $O$.

The devices used in our experiments have a single gate, $V_Q$, which serves as a regulator for the QPC/SET channel. As the two wall gates are very strongly coupled to both the measurement channel and the dot channel, they are usually changed very sporadically and are not usually used either to apply compensation or to serve as a scanning gate.

Returning to the example from before, in which the goal was to scan parameters $R[x]$ and $L[x]$, we can change the perturbation vectors associated with these parameters to ones where the change in $V_R$ is compensated for by a change in $V_Q$ in order to keep the sensitivity of the measurement channel regulated. That is, we replace $\vec{\Delta}_{\{R,L\}}$ with the balanced permutation vector $\vec{\Delta}_{\{R_b,L_b\}}$:

$$\vec{\Delta}_R \rightarrow \vec{\Delta}_{R_b} = \begin{pmatrix} 1 \\ 0 \\ \left.\frac{dV_Q}{dV_R}\right|_{I_{\text{qpc}}} \end{pmatrix}, \qquad \vec{\Delta}_L \rightarrow \vec{\Delta}_{L_b} = \begin{pmatrix} 0 \\ 1 \\ \left.\frac{dV_Q}{dV_R}\right|_{I_{\text{qpc}}} \end{pmatrix}$$

Where, $\left.\frac{dV_Q}{dV_R}\right|_{I_{\text{qpc}}}$ is the change in $V_Q$ required to keep the current in the QPC constant after a change in $V_R$. A similar definition holds for $\left.\frac{dV_Q}{dV_L}\right|_{I_{\text{qpc}}}$ This parameter depends heavily on the geometry of the specific device, but we have observed that it does not change so dramatically within a single device, meaning that these parameters do not need to be re-checked too often. In Si/SiGe devices, we have still observed an improvement over uncompensated scanning by lifting the parameters from one device of a given design and using them on a device of identical design.

The way we obtain the compensation parameter $\left.\frac{dV_Q}{dV_L}\right|_{I_{\text{qpc}}}$ is by measuring the lock-in signal, $\frac{dI_{\text{qpc}}}{dV_g}$, from exciting an arbitrary side gate voltage $V_g$, versus $V_Q$. Several scans are taken so that a measure of noise at each $V_Q$ can be obtained. The specific side gate used, in our case $V_L$, for the tuning lock-in signal should be reasonably coupled to the QPC, but can often simply be the excitation gate to be used during actual measurement. The optimal tuning point is, where

the absolute response of the QPC to the side gate is high, indicating a high sensitivity to signal, but the scan to scan variability is low, representing lower QPC noise. We have observed that in both MOS and Si/SiGe there is often a sweet spot of higher signal to noise ratio, which corresponds to a clean charge sensing signal. Once this sweet spot is identified, either by eye or by an automated process, $V_L$ is then changed by $\Delta V_L$, usually on the order of about 100mV in our devices, and the process of finding the sweet-spot is found again, with care to make sure it is the same sweet spot. The difference in the channel regulating side gate between the two scans, $\Delta V_Q$, is then used to make the approximation $\left.\frac{dV_Q}{dV_L}\right|_{I_{\text{qpc}}} \approx \frac{\Delta V_Q}{\Delta V_L}$. The process can be repeated with the voltage associated with the remaining side gates to obtain the rest of the compensating factors. This allows for an approximate first order correction to the scanning gates by following the update function

$$\vec{V} = R\vec{\Delta}_{R_b} + L\vec{\Delta}_{L_b} + \vec{V}_O.$$

Such a compensation scheme was used in both Si-MOS and Si/Ge devices, and the results were a significantly more robust signal. The results and an outline of the process can be seen in Figure 4.9.

### 4.5.4 Use in tracking an individual quadruple point

#### 4.5.4.1 Inter-Dot tunneling rate tuning

Another form of compensation that the vector scan has been used for is the tuning of an individual double-dot quadruple point through a range of inter-dot coupling levels. As seen in figure 4.10, to determine the compensation required, one takes two stability diagrams, where $V_T$ is changed by $\Delta V_T$. Then, by marking a feature that is shared by the two diagrams, one can determine how much $\Delta V_R$ and $\Delta V_L$ is required in order to stay centered on a feature associated with this anti-crossing. Once these values are determined, a new balanced perturbation vector can be built from the previously defined balanced perturbation vectors, $\vec{\Delta}_{R_b}$, $\vec{\Delta}_{L_b}$ and $\vec{\Delta}_{T_b}$, which is defined similarly. The parameter associated with a perturbation in that vector's direction is called $\delta$ and the vector itself is similarly $\vec{\Delta}_\delta$.

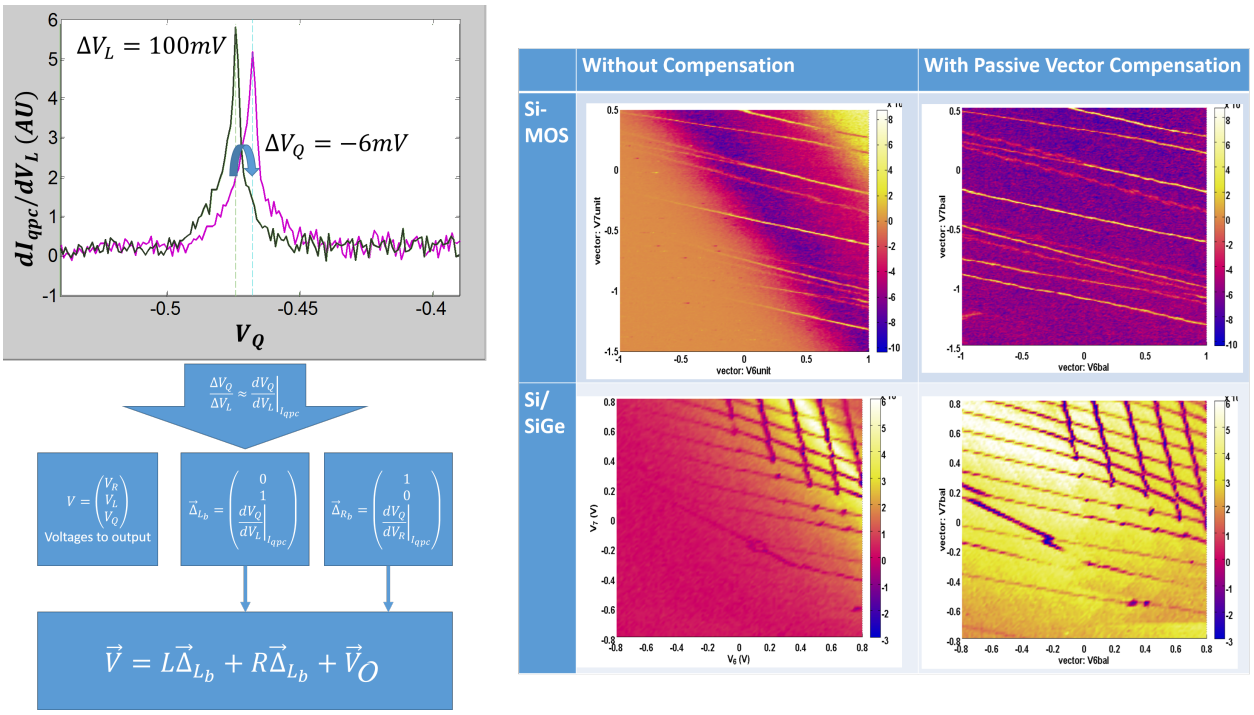


Figure 4.9: (a) An outline of the process for obtaining compensated vectors when using a QPC (b) Demonstration of increased signal across a range of plunger gate voltages in both a SiGe and $SiO_2$.

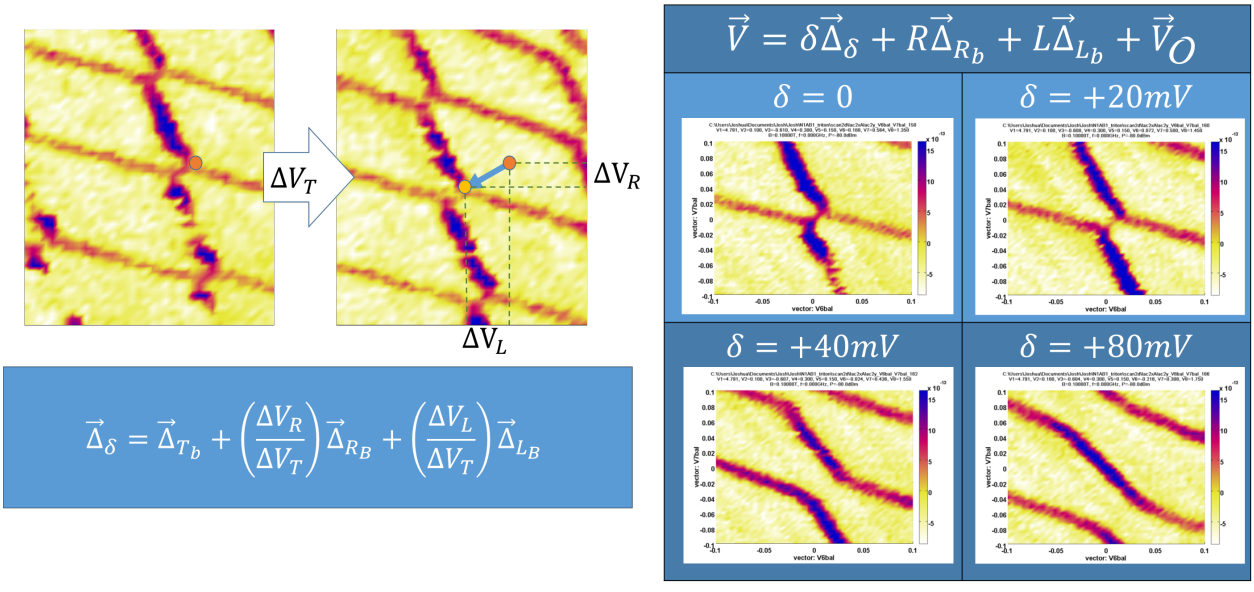


Figure 4.10: (a) An outline of the setup for following an individual anti-crossing across a range of $V_T$ (b) The effect of $V_T$ on the anti-crossing, following the anti-crossing as it moves in plunger voltage space, while keeping the QPC well tuned.

$$\vec{\Delta}_\delta = \vec{\Delta}_{T_b} + \frac{\Delta V_R}{\Delta V_T}\vec{\Delta}_{R_b} + \frac{\Delta V_L}{\Delta V_T}\vec{\Delta}_{L_b}$$

Then a three dimensional parameter scan is performed over a range of values for $\delta$, $R$, and $L$, according to the equation

$$\vec{V} = \delta\vec{\Delta}_\delta + R\vec{\Delta}_{R_b} + L\vec{\Delta}_{L_b} + \vec{V}_O.$$

Using this technique, we tracked an individual anti-crossing over a modest but useful range of different $V_T's$ from the largely uncoupled regime to the nearly single dot regime. The tracking can be seen in figure 4.10. The QPC was occasionally automatically re-tuned at the origin of a new stability diagram, but the value for $V_{Q,O}$ calculated was never more than a millivolt outside of that predicted by the vector framework. Within each scan, vector-style QPC compensation was always used. By allowing the position of the window to track in this manner, we were able to save considerable time by reducing the scan window size. These scans and seven others documenting this tuning were taken over several hours and without manual intervention. Nevertheless, the triple point remained within the scanning region despite $V_T$ being changed over a range well in excess of the deviation, $\Delta V_T$, used to calculate $\vec{\Delta}_\delta$.

#### 4.5.4.2 Barrier tunneling rate tuning

During fast voltage pulsing, the readout from the quantum effects can be enhanced by a so-called "high visiblity region." Since measurement often involves whether or not an electron has remained in a dot or returned to the original dot, the QPC is able to see the result of this measurement as a change in conductance because of differing charge states. However, stronger than the inter-dot signal is a charging signal, since that involves a change in total charge within a dot and not nearly its positions. If the tunneling rates to the barriers are right, the fastest pathway of relaxation may be for an electron to tunnel out of the dots before having the original dot replenished by a separate tunneling event. During that time, the QPC can clearly see the electron loading or unloading, resulting in higher sensitivity of the measurement. But in order to have this effect, the tunneling rates to the reservoir must be well controlled.

There are two different channels for a high visibility region. One of the channels involves

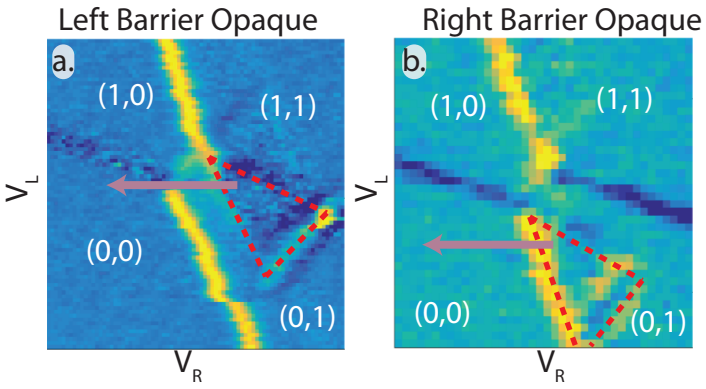


Figure 4.11: A demonstrated switching of the high visibility region. The arrows represent the direction of the pulse. (a) The left barrier is more opaque than the right, leading to a high visibility relaxation pathway of $(1,0) \rightarrow (1,1) \rightarrow (0,1)$; (b) The right barrier is more opaque than the left, leading to a high visibility relaxation pathway of $(1,0) \rightarrow (0,0) \rightarrow (0,1)$.

the electron tunneling out of the . Furthermore, there may be physically motivated reasons to prefer a region where the total number of electrons goes up or one where it goes down. By defining parameters which increase barrier asymmetry, $V_{BL} - V_{BR}$, and following an analogous process to that outlined in the previous section in order to keep the anti-crossing in frame, the relaxation pathway of the high visibility region can be switched from $(1,0) \rightarrow (0,0) \rightarrow (0,1)$ to $(1,0) \rightarrow (0,1) \rightarrow (0,1)$, as shown in figure 4.11.

A change in a plunger gate also has the ability to affect the tunneling rate from the dot across the barrier to the 2DEG reservoir. If one can determine the appropriate level of compensation to apply to $V_{bl}$ in order to compensate for changes in $\vec{\Delta}_{L_b}$ and $\vec{\Delta}_{R_b}$, one could also attempt to keep the dot-2DEG tunneling rate constant while exploring different voltages for the left and right plunger gates. What we have presented is an idiomatic way of expressing this form of compensation. Although we have not use this form of compensation in our lab to keep the dots' tunneling barriers transparent, passive linear compensation applied to tunneling barriers has been successfully used by other groups.[BER15] This framework provides an convenient way to combine these additional compensation factors into the control system.

### 4.5.5 Use to refine parameter space exploration

Defining the parameters to be scanned in terms of vectors within the full space of experimenter controlled parameters allows for more efficient traversal of the parameter space of interest. For example, when scanning an anti-crossing associated with a double dot system, it is sometimes the case that the region of interest is only where the total occupation number of the dot system is 1. Because the charging lines in a stability diagram are rarely completely horizontal or vertical, but rather usually have a negative slope, re-defining the scanning axes can provide for better coverage efficiency. For example, instead of $R$ and $L$, the new parameters could be $\epsilon$ and $\sigma$ , where

$$\vec{\Delta}_\epsilon = \vec{\Delta}_{R_b} - \vec{\Delta}_{L_b}, \qquad \vec{\Delta}_\sigma = \vec{\Delta}_{R_b} - \vec{\Delta}_{L_b}$$

Roughly speaking, $\epsilon$ would point along the detuning axis, and $\sigma$ would point in the direction of increasing total side gate voltage. By elongating the scan in the $\epsilon$ direction but not the $\sigma$ direction, the time required to capture the relevant parts of a stability diagram could be reduced. Furthermore, in the theory of quantum dots, $\epsilon$ is also often used as the detuning axis variable, so in such an instance, this change of variables allows for a more idiomatic framework of control.

Similarly, for a triple dot system, much of the theory is defined in terms of the axis of a subspace in which the sum of the voltages is constant.[TSM13] One of the axes is defined as the difference in energy levels between the two outer dots, and the other axis is defined by how much higher in energy the central dot is in comparison to the average of the outer two dots. While examining a quadruple point, one may desire to scan strictly within this subspace, and make use of these axes. In general to take a two dimensional slice of the three dimensional stability diagram space of a triple dot system will require some form of vector control unless the slices are along the trivial axes. The vector based control framework outlined here provides a way to specify the necessary control in an idiomatic way.

# CHAPTER 5

# Coherent Manipulation of Valley States

As was discussed in Chapter 2 the presence of valley states in silicon has the potential to greatly complicate the use of silicon based quantum dots as a physical implementation of quantum computing. Such systems are considered attractive host candidates mainly due to the long coherence times of individual spins in silicon. And as was discussed in chapter 1, a number of groups have successfully demonstrated coherent control of spin-based qubits in silicon quantum dots.[MBH12, ELS15, VYH15, KSS14]

However the valley degree of freedom presents a major complication to the use of such spin based architectures in silicon. Key to spin based quantum computing architectures is the ability to convert the spin degree of freedom, which is not in general directly measurable, to one of charge (meaning the degree of freedom corresponding to the spatial location of charge bearing particles). In the case of the classic Stern-Gerlach experiment, such conversion would correspond to the spin carrying particle being deflected either one way or the other by the magnetic field depending on the measured spin. In the case of quantum dots, this corresponds to the electron occupation numbers of the various dots. To perform such a conversion in quantum dots it common to seek to exploit the phenomenon of spin-blockade, where an electron tunneling from one dot to another in which an electron with the same spin state already resides may be prohibited by the Pauli exclusion principle.

However, the valley degree of freedom in silicon nanostructures presents a major challenge. Electrons in bulk silicon have six degenerate states, known as valley states, which, when confined to two dimensions, separate into four high-energy states with higher effective mass and two lower energy states. Only the two low energy valley states are energetically relevant to charge/spin states in quantum dots. They are non-degenerate with a splitting energy that de-

pends on the microscopic details of the interface.[YRR13, CSK12, ZLS13, HRX14] Nevertheless, when the energy splitting between the two low energy valley states is small enough, it can provide an additional low lying state, allowing an otherwise blockaded electron to tunnel into a dot and disrupting spin to charge conversion that depends on spin blockade. Thus characterization and control of valley states is important in order to develop a scalable quantum computing architecture using silicon based quantum dots.

In this chapter I will discuss the coherent manipulation of a qubit based on the two valley states of an electron confined in a silcon quantum dot. Coherent evolution between the states, which have a relatively small energy splitting of 20 $\mu$eV, is excited by a fast electrical pulse. Valley-to-charge conversion is performed when the final state in the valley subspace is projected into the occupation numbers of two different charge states, which are then read out by a nearby charge sensing channel.

We have been able to carry out the valley qubit operations at multiple charge configurations of the double quantum dot device. The dependence of coherent oscillations on pulse excitation level and duration allow us to map out the energy dispersion as a function of detuning as well as a lower bound on the phase coherence time of the valley qubit.

As was mentioned in chapter 2, it has been proposed that the valley degree of freedom may itself represent a promising candidate for quantum computing. The energy structure of the valley qubit is similar to spin-charge hybrid qubits,[KSS14, SSW14, CLY16] and shares a desirable resistance to charge noise. The experiment shows the valley states being manipulated are good quantum numbers.

But beyond probing the valley states' potential for use as a qubit subspace, the coherent manipulation presented here also provides a method of measuring valley splittings which are too small to probe with conventional methods of magneto-spectroscopy. Such probing may provide insights into the failure or success of different host materials and structures to exhibit spin blockade.

This chapter is largely based on and lifts liberally from published research from this group.[SFJ17]

## 5.1 The System

Experiments were performed in a device lithographically identical to the device shown in Fig. 5.1a fabricated as described in chapter 3. This particular device was fabricated on a SiGe substrate consisting of a 16 nm silicon well, a 40 nm $Si_{0.7}Ge_{0.3}$ spacer and a 2 nm Si cap. Ti(5 nm)/Au(45 nm) depletion gates were patterned on the substrate. Following this 100 nm of $Al_2O_3$ was grown using atomic layer deposition to provide an insulating layer. Finally, a 300 nm global top gate was patterned over the device area. This gate is used to accumulate a 2-dimensional electron gas (2DEG) within the silicon well. Quantum dots are formed by applying confining voltages (labeled $V_L$, $V_R$, etc.) to the side gates. A charge sensing quantum point contact (QPC), runs adjacent to the dots with a current, $I_{\mathrm{QPC}}$. Ohmic contacts, depicted as squares in Fig. 5.1a, are connected to the source and drain of the QPC and are used to bias the charge sensor as well as measure its current. This current is sensitive to the electron occupation of the dots, and abrupt spikes or dips in the transconductance, $G_\varepsilon \equiv \frac{dI_{\mathrm{QPC}}}{dV_\varepsilon}$, represent transitions between charge configurations as an electron is either loaded into, unloaded from or transferred between the dots in response to a small change in $V_\varepsilon \equiv V_L - V_R$. The QPC transconductance current is measured via a lock-in measurment, where $V_L$ and $V_R$ are simultaneously varied in order to obtain $G_\varepsilon$.

The device was tuned into a triple dot regime. A charge stability diagram (where $G_\varepsilon$ is mapped out as a function of $V_L$ and $V_R$ as described in chapter 4) can be found in Figure 5.1b. The regions between charge transitions are labeled by a three number tuple with the number of electrons in the left, middle and right dots, $(N_L, N_M, N_R)$.

To operate as a qubit, the device is tuned close to a so-called quadruple point, where there is a charge transition from the (0,1,1) configuration to the (1,0,1) configuration. It is important to point out that although there are the three available quantum dots, the states of only a single electron and its transition between the left and middle dots are used to produce qubit behavior. For this reason, and to emphasize the motion of the single electron, in the detailed stability diagram in Fig. 5.1c and subsequently in the body of the text we re-label these charge configurations as (0,1) and (1,0) respectively, where the tuple, $(N_L, N_M)$, represents the left and middle dot electron occupation numbers. Furthermore, we label the electron states associated

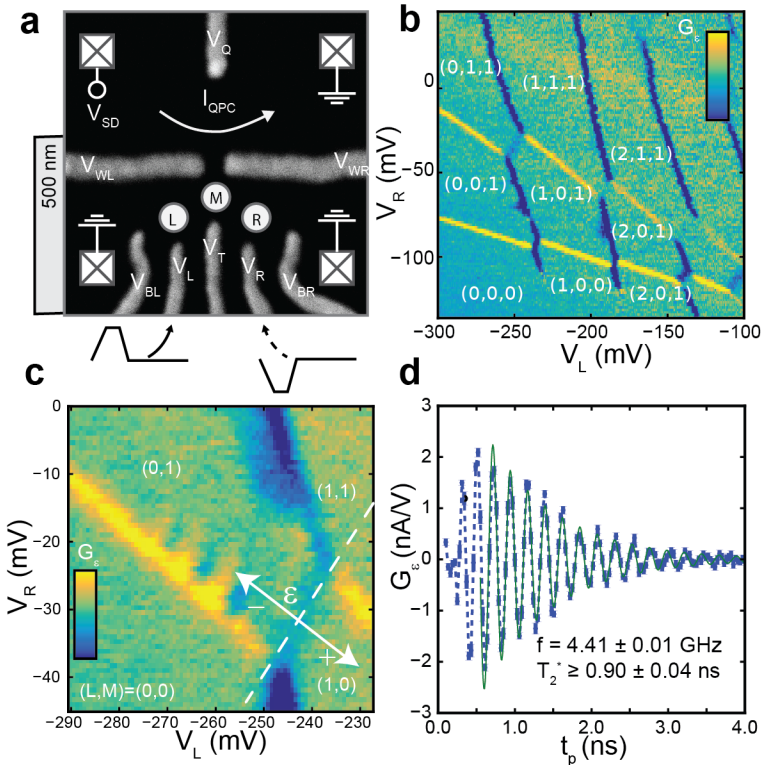


Figure 5.1: (a) A scanning electron micrograph of the quantum dot forming region in a lithographically identical device: The three circles represent the estimated location of three dots. The squares represent ohmic contacts. (b) The charge stability diagram, which maps out the ground state electron occupancy of the three dots as a function of side gate voltages: (c) A close-up of interference fringes at the (0,1,1)↔(1,0,1) charge transition: A 500 ps square pulse with an amplitude of +30 mV is placed on $V_L$. The 0 detuning line is shown as a dotted line and the detuning axis is shown as a solid arrow. (d) Time domain oscillations: Fixing $V_L$ and $V_R$ at values within the interference region and fixing the pulse height at +24 mV, the nominal time of the square pulse is varied, resulting in an oscillatory average charge occupation. Also shown is a fitted decaying sinusoid used to extract a frequency and decay time, the latter of which serves as a lower bound on $T_2^*$. A moving average with a window of several periods of the oscillation has been subtracted prior to fitting to counteract pulse duty cycle effects.

with the charge configurations (0,1) and (1,0) as $|M\rangle$ and $|L\rangle$ respectively, with subscripts added as needed to refer to specific valley states within these charge configurations.

For qubit operation, the primary control parameter is the middle-left dot detuning, $\varepsilon$, which is a measure of potential energy asymmetry between the two dots induced by the confining gates. Adjusting $\varepsilon$ allows for the electron to transfer between the (0,1) and (1,0) states. As defined in this paper, at positive detuning, the (1,0) configuration is energetically favored and at negative detuning the (0,1) configuration is. When detuning is zero, the two configurations are equally favored. This case corresponds to the detuning line in Fig. 5.1c, represented by a dotted line at the boundary between the (1,0) and (1,0) regions of the stability diagram. The solid arrow represents the directions of increasing and decreasing $\varepsilon$.

If no valley splitting is present, or if its value is too large to be relevant to the dynamics, the energy spectrum of the system as a function of detuning would be that of a standard charge qubit as shown in Fig. 5.2a. In contrast, Fig. 5.2b shows the spectrum in the presence of a small valley splitting in the left dot, as in the case in our experiments.

When strongly detuned into the (1,0) charge configuration, the ground and the first excited valley states, $|L_{v_1}\rangle$ and $|L_{v_2}\rangle$ respectively, are separated by the valley splitting $\delta$. The qubit subspace will be the Hilbert space spanned by these two valley states. A model Hamiltonian describing this system, in the basis of $\{|M\rangle, |L_{v_1}\rangle, |L_{v_2}\rangle\}$ is given by

$$H = \begin{pmatrix} \frac{\varepsilon}{2} & \Delta_1 & \Delta_2 \\ \Delta_1 & -\frac{\varepsilon}{2} & 0 \\ \Delta_2 & 0 & -\frac{\varepsilon}{2} + \delta \end{pmatrix} \tag{5.1}$$

where $\Delta_1(\Delta_2)$ is the inter-dot tunnel couplings between the middle dot and the left ground (excited) state.

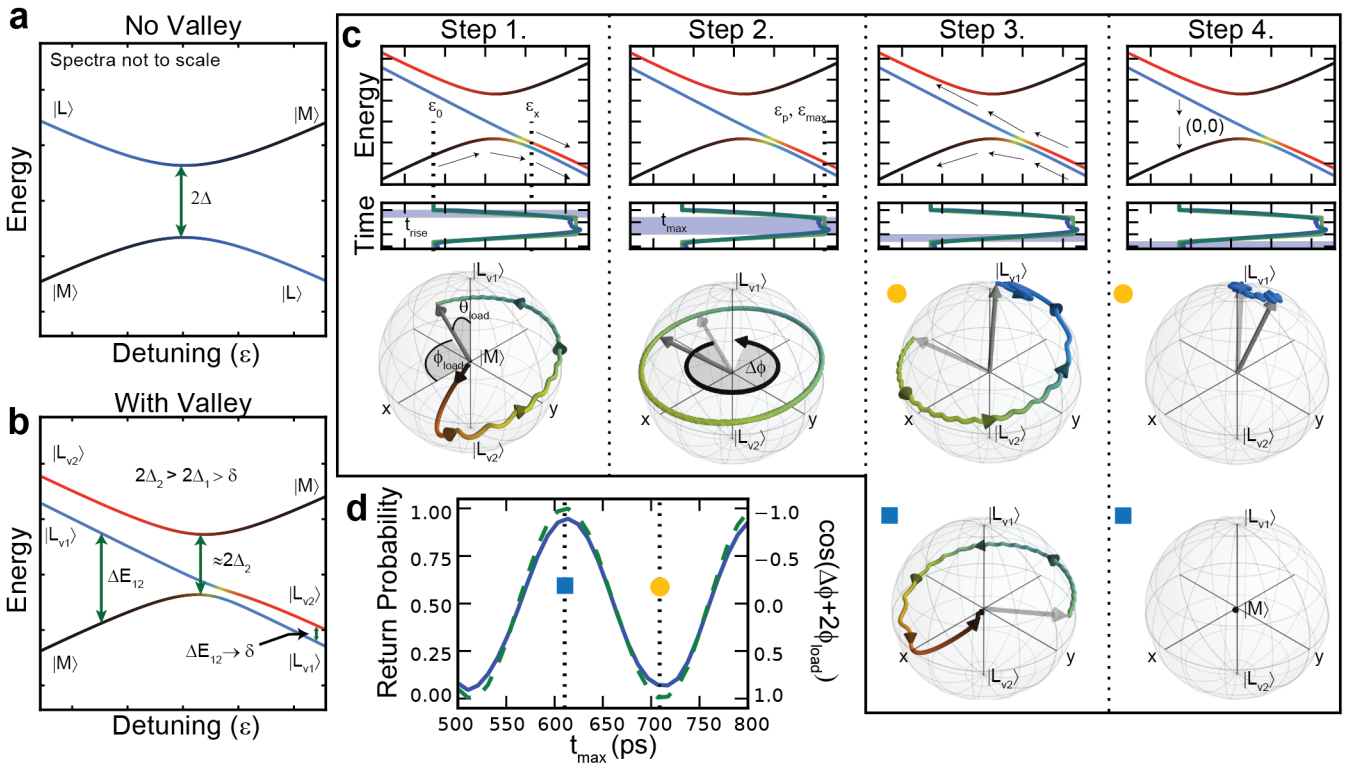


Figure 5.2: (a) The two state spectrum of a standard charge qubit Hamiltonian (b) The three state spectrum in the presence of a small valley splitting: The same coloring is used for these spectra as in figure 2b and d. (c) The steps of qubit operation: Shown is the evolution of the system on the spectrum, the control pulse profile and the evolution of the state within the Bloch sphere of the valley states at the different steps in the state evolution. The paths of states evolution in the Bloch sphere have been colored in the same way as the states in the spectra. (d) The simulated probability of the electron returning to the middle dot plotted along with $\cos(\Delta\phi + 2\phi_{\text{load}})$: The high correlation between these two values shows how the total accumulated phase is effectively encoded in the return probability. The yellow circle marks an amount of phase accumulation that results in the electron likely remaining in the left dot after operation, and the blue square similarly shows the case where it almost certainly returns to the middle dot.

## 5.2 Interference fringes and coherent oscillations between two valley states following

To perform the experiment, positive voltage square pulses were applied to $V_L$ in Fig. 5.1c in order to induce an inter-dot electron transition. Applying such a pulse results in the clear interference fringes present in the stability diagram in Fig. 5.1c. Applying a pulse to only a single gate may temporarily bring the system to a part of voltage space outside of either the (0,1) or (1,0) region. However, because the tunneling rates to the electron reservoirs are slow relative to the pulse durations, which are a few nanoseconds at the longest, the electrons are unlikely to be either loaded or unloaded from the dots during the pulse. Therefore, in Fig. 5.1c, the detuning line is extended into the regions (0,0) and (1,1) to represent that these states are generally invisible to the qubit during its operation time, but that this line continues to represent the boundary between voltage regions where (0,1) and (1,0) are preferred relative to one another. The effect of applying a simultaneous negative voltage pulse to $V_R$ is discussed in section 5.7.

The generated pulses were nominally square, starting at an initial detuning, $\varepsilon_0$, and nominally rising to a detuning of $\varepsilon_p$ for a pulse time $t_p$. But, crucially, in practice they had a non-zero rise time, $t_{\text{rise}}$. To a reasonable approximation, the detuning rises at a constant rate, $v \equiv \frac{d\varepsilon}{dt} \approx \frac{\varepsilon_p - \varepsilon_0}{t_{\text{rise}}}$. The pulse then reaches a maximum detuning, $\varepsilon_{\text{max}}$, where it remains for a time $t_{\text{max}}$, corresponding to the remainder of $t_p$. (If the rise time is longer than $t_p$, then $t_{\text{max}}$ might be zero. If $t_p > t_{\text{rise}}$, then $\varepsilon_p = \varepsilon_{\text{max}}$.) After $t_p$ has elapsed, the detuning returns to $\varepsilon_0$, again at a rate of roughly $v$, where it remains for 30 ns until the next pulse.

The clear interference fringes in Fig. 5.1c induced by a short pulse of 500 ps are a signature of the coherent evolution between the two valley states in the left QD during the pulse duration. We believe the energy splitting in the middle dot is much larger, since no interference can be observed when the pulse is pumped in the opposite direction.

Fixing the DC voltages of the side gates at a point within the interference region, coherent time domain oscillations of $G_\varepsilon$ are observed by varying pulse width. Fig 5.1d shows the differential measurement QPC current, which relates to the probability of being in state (0,1), $|M\rangle$,

at the end of operation time, as a function of $t_p$, for a given pulse height. Also shown as a solid line is a decaying sinusoidal fit used to extract both the oscillation frequency and decay times, the latter of which serves as a lower bound on $T_2^*$.

## 5.3 Principle of the valley qubit operation and read-out

The qubit operation is outlined in Figure 3c. In step 1, the system begins at a negative initial detuning, $\varepsilon_0$, with the electron in the ground state, $|M\rangle$. Then, so long as the level anti-crossing between $|M\rangle$ and at least one of the left states is highly gapped relative to $\sqrt{\hbar v}$, the pulse adiabatically brings the electron from state $|M\rangle$ to the left dot. As the pulse continues to rise, the system is brought non-adiabatically through a level anti-crossing which occurs at detuning $\varepsilon_x$. Near this anti-crossing the lower two eigenstates are both superpositions of $|L_{v_1}\rangle$ and $|L_{v_2}\rangle$, a feature which is indicated in yellow on the spectra in figures 5.3b, 5.3d and 5.3b. The total effect of these two transitions is a unitary transformation that loads the state $|M\rangle$ into a state approximately given by $e^{i\Phi(0)}\left(\cos\left(\frac{\theta_{\text{load}}}{2}\right)|L_{v_1}\rangle + e^{i\phi_{\text{load}}}\sin\left(\frac{\theta_{\text{load}}}{2}\right)|L_{v_2}\rangle\right)$, where $\theta_{\text{load}}$ and $\phi_{\text{load}}$ are angles in the Bloch sphere defined by $|L_{v_1}\rangle$ and $|L_{v_2}\rangle$ and $\Phi(0)$ is an overall phase that does not affect measurement. This unitary transformation as well as the overall loading fidelity into the left subspace are dependent on $v$.

In step 2, once the pulse reaches its maximum detuning, $\varepsilon_{\text{max}}$ , the system is far detuned towards the left dot, and assuming that $t_p > t_{\text{rise}}$, the detuning level is now constant for a time $t_{\text{max}}$, so the state will evolve according to the Schrödinger equation as

$$|\Psi\rangle = e^{i\Phi(t)}\left(a\,|\psi_1\rangle + e^{i\frac{\Delta E_{12}(\varepsilon_{\text{max}})}{\hbar}}b\,|\psi_2\rangle\right).$$

Given that near $\varepsilon_{\text{max}}$ the energy eigenstates $|\psi_1\rangle$ and $|\psi_2\rangle$ are almost exactly the states $|L_{v_1}\rangle$ and $|L_{v_2}\rangle$, this may be approximated as

$$|\Psi\rangle = e^{i\Phi(t)}\left(\cos\left(\frac{\theta_{\text{load}}}{2}\right)|L_{v_1}\rangle + e^{i\left(\phi_{\text{load}}+\frac{\Delta E_{12}(\varepsilon_{\text{max}})}{\hbar}\Delta t\right)}\sin\left(\frac{\theta_{\text{load}}}{2}\right)|L_{v_2}\rangle\right)$$

where $|\psi_1\rangle$ and $|\psi_2\rangle$ are the ground and first excited state, $\Delta E_{12}$ is their energy difference, and $a$

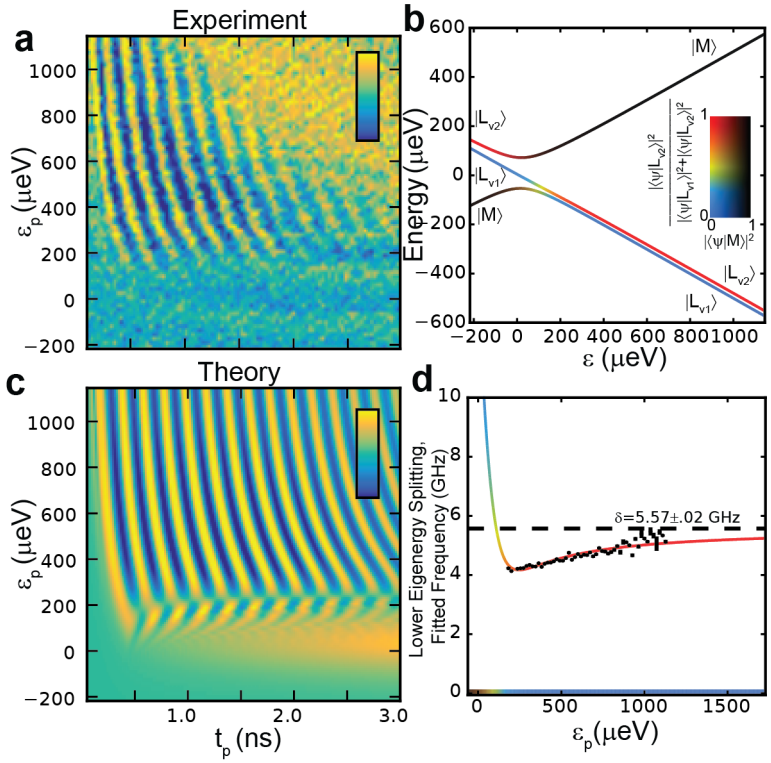


Figure 5.3: Experimental mapping of the detuning dependence of the time domain oscillations; (b) Energy spectrum derived from fitting to the extracted dispersion: A two dimensional colorbar is used to simultaneously map a state's makeup in the charge degree of freedom (brightness) and valley degree of freedom (hue).( $\delta = 5.57\,\text{GHz}$, $\Delta_1 = 6.4\,\text{GHz}$, $\Delta_2 = 13.6\,\text{GHz}$) (c) Simulated charge sensing transconductance signal, obtained by solving the time dependent Schrodinger equation without dissipation: A square pulse with a finite rise time of 200 ps was assumed. (d) Experimentally extracted frequencies plotted along with the separation between the lower two eigenenergies as a function of detuning: The extracted value of the valley splitting, $\delta$, is plotted as a dotted line. The color of the fitted curve is the color associated with the middle eigenstate at a detuning using the coloring from (b). Along the bottom axis, the color represents the makeup of the ground state.

and $b$ are the initial coefficients when $\varepsilon_{\max}$ is first reached, $\Delta t \equiv t - t_{\text{rise}}$ is the time spent at $\varepsilon_{\max}$, and $\Phi(t)$ is a time dependent overall phase that does not affect measurement. The axis of control is almost purely along the $z$-axis of the Bloch sphere. Therefore, the state precesses around the $z$-axis at a Larmor frequency given by $\Delta E_{12}$. The effect on the qubit state of the system being maximally detuned for a time $\Delta t$ is approximately given by $R_z(\Delta\phi)$, where $\Delta\phi = \frac{\Delta E_{12}}{\hbar}\Delta t$.

In step 3, as the pulse returns to its initial value, $\varepsilon_0$, the system first pulses through the anti-crossing at $\varepsilon_x$, experiencing another non-adiabatic transition. The system then experiences another adiabatic charge transition where the ground state is projected to $|M\rangle$ and the first excited state is projected to the left states. The net result of this step is that the total phase accumulated, $2\phi_{\text{load}} + \Delta\phi$,is encoded in the probability of the electron returning to the middle dot, as shown in Fig. 5.2d. Since these two states correspond to different charge configurations, they are discernible to the QPC, which collapses the system to one of these two measurement states. If the electron is measured to have remained in the left dot, it will remain there until it relaxes back to the ground state.

Step 4, the measurement/re-initialization phase, is much longer than $t_p$, so its average charge configuration is the primary contributor to the differential transconductance, $G_\varepsilon$. Therefore, $G_\varepsilon$ is sensitive to the probability of the electron finally being in state $|M\rangle$ and ultimately to $\Delta\phi$. Further enhancing the sensitivity of the QPC is the fact that since the charge relaxation rate, $T_1$, is likely longer than the measurement/initialization time of 30 ns, the readout will be most pronounced in so-called the high visibility region, where the fastest relaxation channel of the electron from the left dot back to the middle dot is by first having the electron tunnel out of the dots ((1,0)→(0,0)) and then a different electron tunneling directly back into the middle dot ((0,0)→(0,1)).[WPD13] In such a region, the total charge occupancy of the dots temporarily changes, which enhances read out sensitivity as the QPC is more sensitive to the total number of electrons in the dots than to their positions within the dots. After this relaxation process, the qubit has been re-initialized to $|M\rangle$.

## 5.4 Detuning Dependent Coherent Oscillations

Fig. 2a shows the dependence of the coherent time domain oscillations on $\varepsilon_p$. In Fig. 5.3b, The energy spectrum is plotted over a detuning range that matches the one explored in Fig. 5.3a. Fig. 5.3c shows a simulated lock-in signal produced by time-evolving the Schrodinger equation under the influence of a square pulse with a finite rise time as a function of $\varepsilon_p$ and $t_p$.

The evolution of the qubit was examined numerically by time evolving the Schrodinger equation in the density matrix formalism[WM09]: $\frac{d\rho}{dt} = -\frac{i}{\hbar}[H, \rho]$. The expected charge state is given by the probability of being in the middle dot: Tr $(\rho \left|M\right\rangle \left\langle M\right|)$ The simulation explicitly included neither dephasing nor charge relaxation, and could therefore not make a full prediction of the average charge configuration. Instead, the final charge state after 4 ns of operation time is used as a proxy for the average QPC current. Since this final time is well into the measurement period for all operation times considered, and since the charge relaxation time $T_1$ is believed to be relatively slow, this state is taken to be representative of the pulse's effect on the average charge configuration observed by the QPC, and therefore of the average QPC signal.

Simulation of the trans-conductance signal was achieved by sampling the simulated $\varepsilon_0$ from $\varepsilon_0 + A \sin(x)$, where the spacing in $x$ was even between $-\frac{\pi}{2}$ and $+\frac{\pi}{2}$. Then the calculated average charge occupancy from these simulations was numerically integrated against $\sin(x)$ to simulate the real part of the QPC signal as described in Appendix A.

The fixed parameters in the Hamiltonian, $\Delta_1$, $\Delta_2$ and $\delta$, are determined by matching the observed frequency of time domain oscillations to a numerically calculated value of $\Delta E_{12}$ as a function of $\varepsilon$ using a weighted least squares fit. In Fig. 5.3d, the observed frequency is plotted versus detuning along with the calculated value of $\Delta E_{12}$.

An example of the decaying sinusoidal curve fit used to extract the observed frequency is presented in Fig. 1d as the solid green line. The fit was restricted to data where $t_p$ was greater than 500 ps, to allow the pulse to significantly exceed its rise time, which is estimated to be about 100-200 ps. By making this restriction, a change in the total pulse time, $\Delta t_p$, leads directly to a change in the time spent at the maximum detuning, $\Delta t_{\max}$. The additional pulse time should, therefore, contribute directly to additional phase accumulation at detuning $\varepsilon_p$. The extracted

frequency can then be used to map out the detuning dependence of $\Delta E_{12}$, as shown in Fig. 5.3d.

The extracted Hamiltonian parameters in general depend on the lever arm, $\alpha$, which, based on magneto-spectroscopy of a lithographically identical device in a similar configuration, we estimate to be 3%. The only extracted parameter that is nearly independent of $\alpha$ is $\delta$, which is measured reliably to be $\sim 5.6\,\mathrm{GHz}$ across a variety of assumed $\alpha$'s. This is because $\delta$ is the value that the observed frequency approaches as the dot becomes highly detuned (See the dotted line in Fig. 5.3d).

Through simulation, we find that the specific value of $\alpha$ assumed and the corresponding values for $\Delta_1$ and $\Delta_2$ in the Hamiltonian affect the details of evolution in a detuning region ($\varepsilon_p < \varepsilon_x$) where $\left|\frac{d\Delta E_{12}}{d\varepsilon}\right|$ is large. In this region susceptibility to charge noise is too great to observe coherence given our experimental setup's noise level. In the highly detuned region ($\varepsilon_p > \varepsilon_x$) where $\Delta E_{12}$ asymptotically approaches $\delta$, $\left|\frac{d\Delta E_{12}}{d\varepsilon}\right|$ is small, hence the qubit is protected against charge-noise induced decoherence.

The increased coherence times in a wide region of nearly constant dispersion is a feature shared with recently reported spin-charge hybrid qubits, which rely on the small correlation energy of singlet/triplet-like states. However, in hybrid qubits, which tend to be guided by Hamiltonians where $2\Delta_1, 2\Delta_2 < \delta$, the frequency approaches a minimum close to the detuning line. Instead, in our system, the qubit behavior does not appear until deeply detuned into the left dot, and, even then, never exhibits the pronounced chevrons as the pulse approaches the detuning line.

## 5.5 Phase Coherence

From the decaying sinusoidal fit of the QPC signal, one can extract the decay time of the oscillations, which is a lower bound on the coherence time $T_2^*$. As shown in Fig. 5.4b, there is a peak in the observed coherence time at $\varepsilon_p$ of a few hundred $\mu$eV. For comparison, the measured dispersion is displayed in Fig. 5.4a. At smaller detuning levels, the coherence time decreases rapidly. This is likely due to being in a region of rapidly increasing $\left|\frac{d\Delta E_{12}}{d\varepsilon}\right|$, which will enhance the de-cohering effect of charge noise. Eventually oscillations disappear, likely due to not having

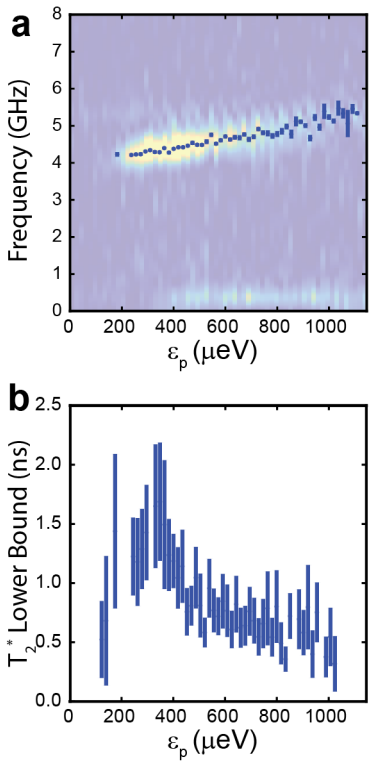


Figure 5.4: (a) The dispersion extracted from both an explicit sinusoidal fit, as in Fig. 1d, and from a Welch periodogram, both taken line by line from Fig. 2a. (b) The extracted values of the decay time: This value is actually a lower bound on phase coherence time $T_2^*$. The decay time increases rapidly at first and then begins to decrease. The longest value directly observed is 1.5 ns.

experienced the non-adiabatic portion of the pulse.

At higher detuning, the coherence time decreases gradually. This is likely due to the increased tendency of the system to transition to the nuisance (1,1) charge configuration as that state is made more favorable relative to the (1,0) configuration in which the qubit operates. At higher pulse amplitudes, the potential barrier between the left dot and the electron reservoir is lower, potentially exposing the electron to the effects of the environment.

The maximum observed coherence time is about 1.5 ns. We believe that it is limited by the system tunneling, since the pulse is not applied parallel to the detuning direction. As will be discussed in section 5.7, there is evidence that the actual coherence time could be longer, if the pulse induced tunneling to the reservoir can be suppressed.

## 5.6 Oscillation at Additional Anti-Crossing and Implications

It is important to point out that coherent oscillations with similar frequencies were observed at two consecutive anti-crossings. Such behavior was present not only at the quadruple point connecting the (0,1,1) and (1,0,1) charge regions but also at that connecting the (1,1,1) and (2,0,1) regions, as can be seen in Fig. 5.5a. The analysis of the other anti-crossing's qubit behavior proceeds just as that of the anti-crossing which was examined in the main text. Fig. 5.5 shows qubit operation in the (1,0,1) and (2,0,1) regions. There are significant qualitative similarities between the two tuning points. The two pulse height versus pulse width scans can be compared in Fig. 5.5b and Fig. 5.5c. The alternative crossing's decoherence dependence can be seen in Fig. 5.5d and its dispersion can be seen in Fig. 5.5e.

The presence of the behavior at multiple consecutive anti-crossings provides clues as to the nature of the excited state used in the qubit operation. For instance, the states whose coherent manipulation is observed here are unlikely to be spin-based, as the spectrum of energies associated with spin degrees of freedom are highly dependent on electron number parity. Furthermore, the possibility of the qubit space being composed of orbital states is precluded by the magnitude of $\delta$. Based on estimates of dot dimension, such an excited state would be expected to be an order of magnitude higher. Also, the control of oscillations with an energy splitting well below the thermal energy scale suggests that the valley states being manipulated are good quantum numbers. We therefore conclude that the qubit behavior reported here is the result of coherent manipulation of the valley states of silicon.

## 5.7 Diagonal Pulsing and Apparent Coherence Times

One difference between our hybrid qubit and that of some other groups is that we do not exhibit the detuning independent coherence times at greater pulse heights, which should be a natural consequence of the rather flat dispersion regime that the hybrid qubit operates in. We believe that this is due to our pulsing scheme, which is usually limited to a single gate, rather than being composed of two coordinated pulses on different gates, as seen in Fig. 5.6c. Because of this, as the

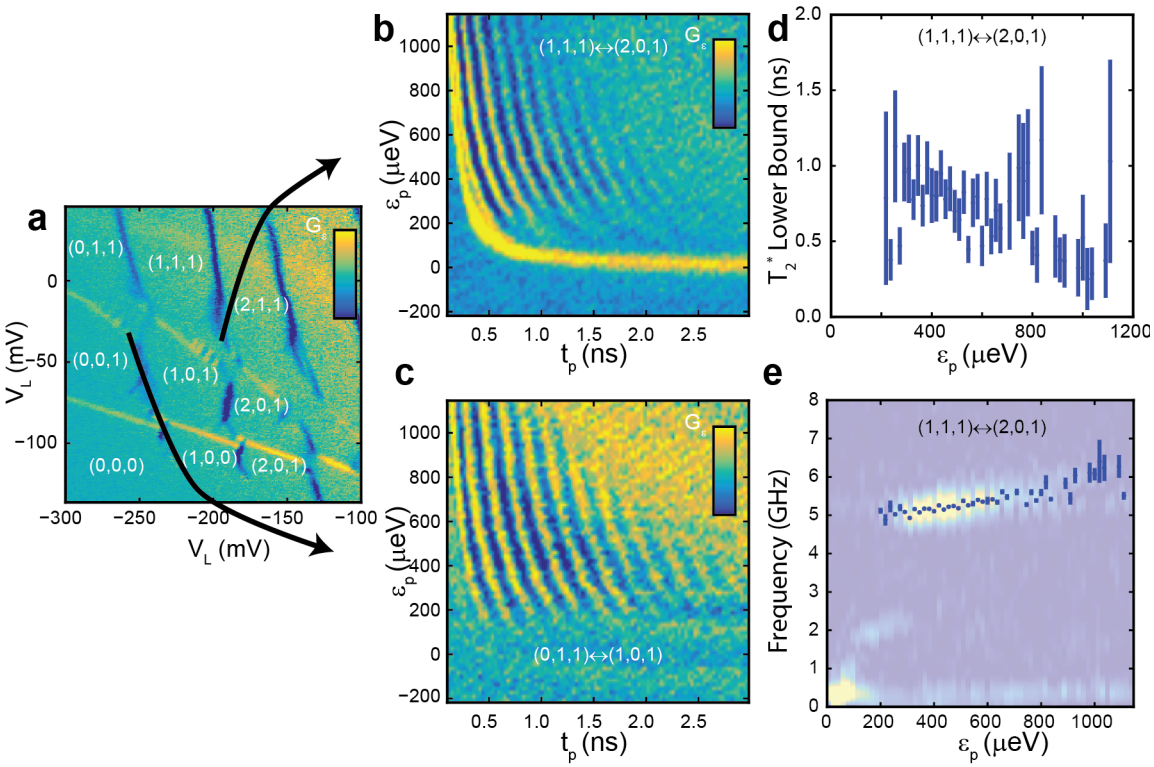


Figure 5.5: (a) The triple dot charge stability diagram with a pulse applied: This figure covers the same range as the stability diagram in Fig 1b, but with a pulse applied to $V_L$. It can be seen that interference fringes are simultaneously present at both the (0,1,1)↔(1,0,1) transition and the (1,1,1)↔(2,0,1) transition. (b) Experimental mapping of the detuning dependence of the time domain oscillations at the (1,1,1)↔(2,0,1) transition. This is directly analogous to Fig. 5.3a. (c) The pulse width and height dependence of the (0,1,1)↔(1,0,1) transition: This is the same as Fig. 5.3a. It is repeated here for comparison with (b). (d) The extracted decay times and (e) frequencies: These are obtained from (a) in the same way as the plots in Fig. 5.4.

amplitude of the pulse increases, the tendency to tunnel from (1,0) to (1,1) during the operation time becomes greater. If this happens, it disrupts the operation and initialization and the signal appears to more quickly attenuate as the pulse gets deeper into the region where (1,1) is favored. This can be observed in Fig. 5.6d. When two counteracting pulses were placed on separate gates, as in Fig. 5.6a, the general strength of the signal was greater and the coherent region extends further in $\varepsilon$ as seen in Fig. 5.6b. Due to difficulties with syncing the two pulses, the bulk of the experiments were performed with single-gate pulses. But the increased coherence time associated with two-gate pulses suggests that the discrepancy between the detuning dependence of our coherence times and those of other groups is due to our pulsing limitations, and were we better able to sync the pulses, a similar coherence profile may be observed.

An alternative possibility is that the greater pulses begin to have an effect on the barrier potential and not just the plunging voltage. By lowering the barrier, the electrons in the left dot are exposed to the environment to a greater extent, which contributes to dephasing during operation.

## 5.8 Contrast with other reported hybrid systems

According to the fit for the parameters of the Hamiltonian, with $\alpha = 3\,\%$,

$$\delta = 5.57\,\text{GHz} \qquad \Delta_1 = 6.4\,\text{GHz} \qquad \Delta_2 = 13.6\,\text{GHz}$$

The energy splitting for these extracted parameters can be seen in Fig. 5.3d, and the spectrum, plotted to scale, for these extracted parameters can be seen in figure 5.3b. In comparison to other hybrid like systems, ours operates in a different regime of tunnel couplings. Those other systems tended to operate where $2\Delta_1$ is less than $\delta$. For example, Shi et al.[SSW14] reports values where $\Delta_1 = 2.62\,\text{GHz}$, $\Delta_2 = 3.5\,\text{GHz}$, while $\delta = 9.2\,\text{GHz}$ (See also Kim et al. [KSS14]). The spectrum which results from such a regime is different from that reported here. Most notably, the avoided crossing between $|M\rangle$ and$|L_{v_1}\rangle$ at $\varepsilon \approx 0$ has a small enough splitting that passage through it is non-adiabatic. This means that coherent oscillations can be seen even

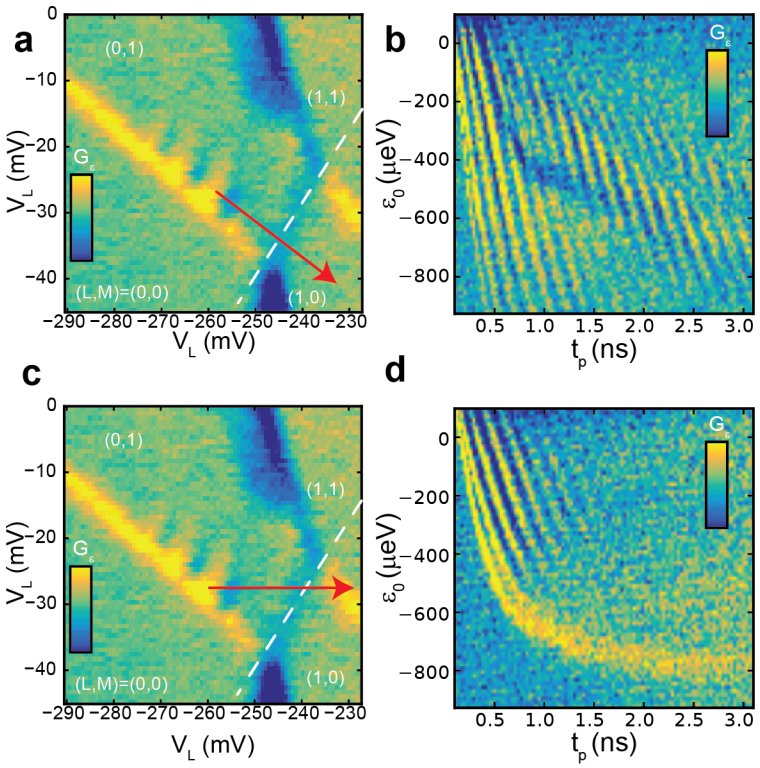


Figure 5.6: (a) Stability diagram from Fig. 5.1a showing the direction of a pulse when voltages are applied to both $V_L$ and $V_R$: The effect is to have a pulse which is more purely in the detuning direction without bringing the system to a voltage space where the ground state has a different total occupation. (b) Demonstration of enhanced coherence times with a diagonal pulse: The initialization/measurement point is varied as pulse width traces are taken with a fixed pulse height of +30 mV on $V_L$ and −30 mV on $V_R$. When such a pulsing system is used, strong oscillations are clearly visible out to 3 ns, which is considerably longer than the longest achieved with a single gate pulse. However, due to difficulty in pulse synchronization, usually only a single gate pulse is used. (c) A stability diagram showing the direction of a single gate pulse: Such a pulse brings the system into the (1,1) region during operation. (d) A plot identical to that of (b) except that pulses are only applied to $V_L$: A reduced apparent coherence time is visible as well as an additional bright and apparently incoherent line, which is believed to be (1,1)↔(1,0) charging line.

when $\varepsilon_p$ is close to 0. The oscillations seen at $\varepsilon_p \approx 0$ are slower than those caused by $\delta$ and are protected from decoherence because $\frac{d\Delta E_{12}}{d\varepsilon} = 0$ at that point. In contrast our system has no visible fringes as $\varepsilon_p$ approaches 0. We conclude that this is because when $0 < \varepsilon_{\max} < \varepsilon_x$, the operation includes no non-adiabatic process. Furthermore, at that point and anywhere to the left of $\varepsilon_x$, $\left|\frac{d\Delta E_{12}}{d\varepsilon}\right|$ is large, contributing to significant susceptibility to electronic noise. The conclusion that we operate in a regime where $2\Delta_1, 2\Delta_2 > \delta$, is further supported by the results of numerical fitting for the Hamiltonian parameters.

## 5.9 Use in Valley Splitting Metrology

As a host candidate for quantum information processing, qubits operating in a region of detuning invariant energy splitting, such as hybrid qubits and the valley qubit reported here, offer a promising combination of fast operation and resistance to noise.

However, the magnitude of the energy splitting between valley states in a given silicon based device is an important value in its own right, as it informs whether the device will be suitable for many exchange-based qubit architectures, which in general require the presence of Pauli spin blockade to perform spin to charge conversion. Valley splittings which are too small can disrupt spin blockade by providing an additional low energy state for an electron to tunnel into with the same spin configuration as that which would otherwise be blockaded. Often the magnitude of the valley splitting in a device is measured using magneto-spectroscopy. However, the magnitude of the valley splitting reported here in both charge configurations is below the measurement threshold for such techniques. The coherent measurements performed here could serve as a valuable method of probing the magnitude of certain smaller valley splittings.

As shall be seen in chapter 6, our group has already begun to use fast pulse coherent probing to explore the protected valley states of other devices.

# CHAPTER 6

# Noise resistant operation and valley spectroscopy

## 6.1 The dispersion-decoherence relationship

We have found that observing Landau-Zener based charge qubit oscillations[CLT13] in our dilution fridge setup has proved quite difficult. In a previous lab member's thesis, rough indications of charge based oscillations were visible in a MOS system using the JDR-500 dilution refrigerator setup.[Pan13] However, in our experiments conducted in SiGe based heterostructures, we were unable to observed charge qubit oscillations.

Those coherent oscillations which have been observable, such as those outlined in chapter 5, have all had a distinguishing feature: A roughly invariant operation frequency irrespective of the operation detuning point. This corresponds to a very flat dispersion. There is a strong relationship between the dispersion of a system and its susceptibility to charge noise. In general, when viewing a spectrum as a function of dot potentials, which are affected by voltage fluctuations in the leads and by charge fluctuations around impurities in the substrate, the greater the dependence of the energy gap between levels the greater the susceptibility to charge noise. Therefore, in systems where there is a broad region in potential space where the energy gap is constant, such as the hybrid qubit, there is a resilience to charge noise.[Qin16]

In this chapter, I will present measurements from three different devices, showing coherent operation within a region of low dispersion and discuss the application of such measurements to valley spectroscopy, where the value of interest is the valley splitting.

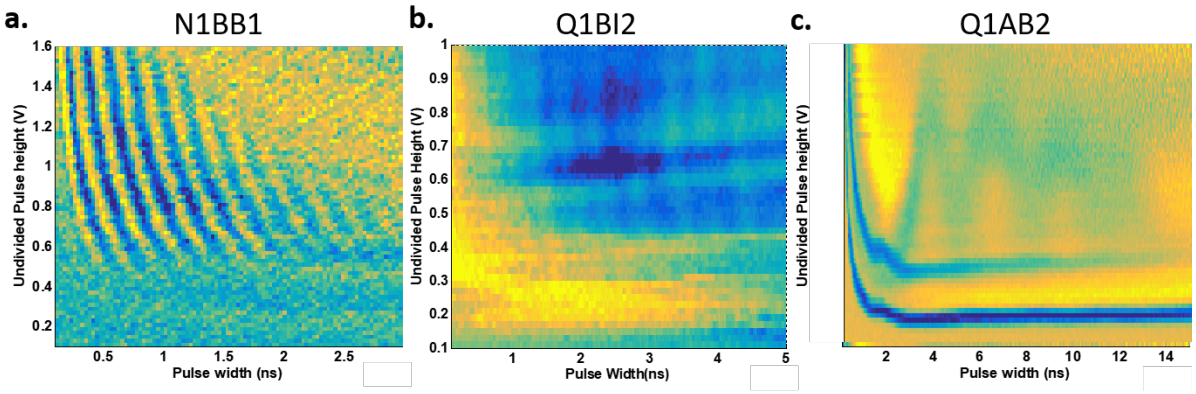


Figure 6.1: Coherent manipulation of states from three different devices with three different valley splitting values.

| Device: | N1BB1 | Q1BI2 | Q1AB2 |
|---|---|---|---|
| Splitting Frequency | $\sim 5.5 - 6.5$ GHz | $\sim 1.5$ GHz / 400 MHz | $\sim 340$ MHz |
| Consecutive Anti-Crossings | 2 | 3 | 1 |

Table 6.1: Summary of the three devices where valley splitting was coherently measured.

## 6.2 Valley spectroscopy of several devices

As has been seen in chapter 5, the use of non-adiabatic square pulses across the detuning line of a double dot system allows for coherent manipulation of its states. Furthermore, in the case of silicon based systems, there is the potential to gain insight into the magnitude of a valley splitting within a given configuration. We applied this technique to additional devices in order to measure the magnitude of their valley splittings.

Just as in the previous chapter, the first form of probing was to apply non-adiabatic square pulses across the detuning line and look for time dependence of the resulting QPC signal. The signature for the measurement of a valley splitting is a broad region of roughly constant splitting observed at multiple consecutive charge configurations of the operation dot. Examples of the coherent measurements taken from the three devices can be found in Figure 6.1.

It is worth noting that there is not a definitive single value for the valley splitting for a given device. As has been discussed in chapter 2, the valley splitting and inter-valley coupling can both be tuned by shifting the location of the dots relative to impurities. Furthermore, within different

dots, the valley splitting can vary. It seems likely that a demonstration of this fact can be seen in the device from chapter 5, where the measurement dot has been shown to have a first excited state much more energetic than the first valley state of the operation dot. Also, subsequent experiments using the device Q1BI2, which initially had a valley splitting in the operation dot of roughly 1 GHz, have shown its operation frequency to have decreased to roughly 400 MHz following the device having been warmed to room temperature and re-cooled. Nevertheless, such a measurement would still be useful for assessing the potential of a given configuration of a device during a specific cooldown.

### 6.2.1 Differences in clarity

The clarity of the oscillations in two of the three devices probed in this manner was noticeably less than that of those from the third device. We believe that this is due to the particular states of the measurement dots. Aiding in the visibility in dot N1BB1 was a very energetic state in the measurement dot. Evidence for this can be found int he shape of the fringing region of that dot system. Particularly at the (1,1,1)↔(2,0,1) crossing, the shape of the visibility region is clearly trapezoidal. The shape of this region can be explained by the presence of an additional high energy state in the middle dot with a high coupling to the lower valley state of the left dot, as is shown in Figure 6.2. The effect is to divide the classical high visibility region into three distinct regions.

The high visibility region as described in other work on charge qubits[DSP11] is a triangular region, consisting of all three regions marked in Figure 6.2, where the state (0,0) is energetically favorable to the excited charge state (1,0), but is not the ground state. However, in device N1BB1, visibility is limited to a trapezoidal region made up of only regions 1 and 2. In region 1, the mechanism of relaxation is the same as for the standard charge qubit high visibility region: the electron in the excited charge state, (1,0), tunnels out of the dot and another tunnels back in to fill the ground state (Figure 6.2b). However, when the measurement point is further detuned towards the middle dot, the electron in the excited charge state makes an adiabatic transition to an excited state of the middle dot, as indicated by the dotted arrow in figure 6.2c. From

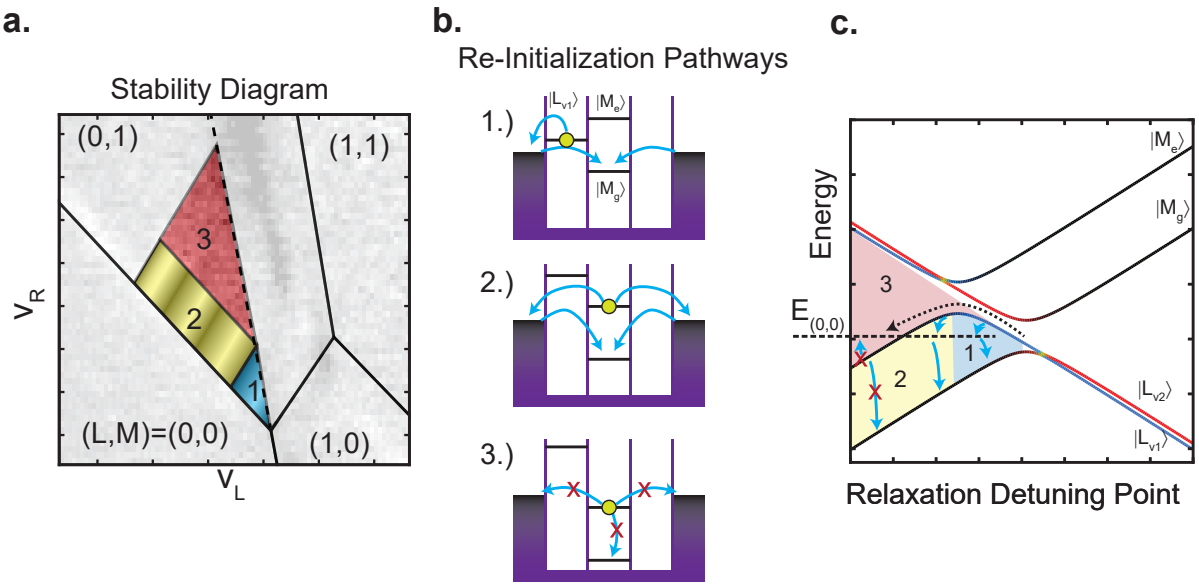


Figure 6.2: a. The standard high visibility region is divided into three regions. Fringes are only observed in regions 1 and 2. b. The relaxation pathways of the three regions: In region 1, an electron measured to be in the excited state is in a different charge configuration. The electron tunnels out and then a different electron tunnels back in. Also, direct charge relaxation is possible on the timescale of the pulse repetition rate. In regions 2 and 3, the electron will be in an excited middle dot state. In region 2, tunneling out before resetting is energetically favorable, allowing for visible fringes. In region 3 such tunneling is not allowed. Furthermore valley to valley relaxation is slow compared to the pulse repetition rate. Therefore, resetting is disrupted and no fringes are visible. c. A spectrum showing the excited middle dot state as well as the state trajectory when the system does not return to the middle ground state (dotted arrow). The shape of the spectrum is reflected in the trapezoidal region of visibility. The regions are defined on the x axis by the relaxation detuning point and on the y axis by the relative energy of the (0,0) state.

here relaxation is only possible if it is energetically favorable for the electron to tunnel out of the middle dot, as it is in region 2 but not region 3. The total absence of fringes in region three, where tunneling assisted relaxation is not energetically feasible, indicates a relaxation time between the two middle dot states that is significantly longer than the pulse repetition rate. This is consistent with prior literature suggesting that valley to valley relaxation time is on the order of tens to hundreds of microseconds. The experiments presented here were primarily performed in region 1, however occasionally they were performed in region 2, without any additional complication. The shape of the spectrum is mirrored in the shape of fringing region on the stability diagram, analogously to how the tunnel coupling can be seen from the curvature of the charging lines near the quadruple points.[HKP07]

In the other devices, rather than being between a middle and a left dot, the electron transition was between a left and a right dot. These two dots are more similar in dimensions, as they are designed to be mirror images of each other. As will be discussed, there is even some indication that the value of the valley splitting in each of the dots are very similar and quite small, meaning that the measurement pathway for the other devices was necessarily distinct from that from N1BB1. This suggest both a less efficient readout and possibly a less efficient mixing operation as well. This could explain why visibility is poorer.

### 6.2.2 Low Efficiency Spectroscopy

In order for initialization and readout to be efficient the inter-dot coupling as well as the valley splitting must be relatively well tuned. Simulation seems to suggest that at least one anti-crossing in the spectrum should have a splitting of a few gigahertz. This could pose a problem for using square pulse based valley spectroscopy over a wide range of values, particularly in the regime of lower coupling or valley splitting. However, the fact that oscillations are seen over such a wide range of valley splittings suggests that features resulting from the fixed splitting can be seen despite configurations of the dots that are not particularly well tuned.

To explain this, we performed simulations of pulses applied to systems in parameter space far away from the well tuned regime. In Figure 6.3a, the spectrum for such a system is shown to

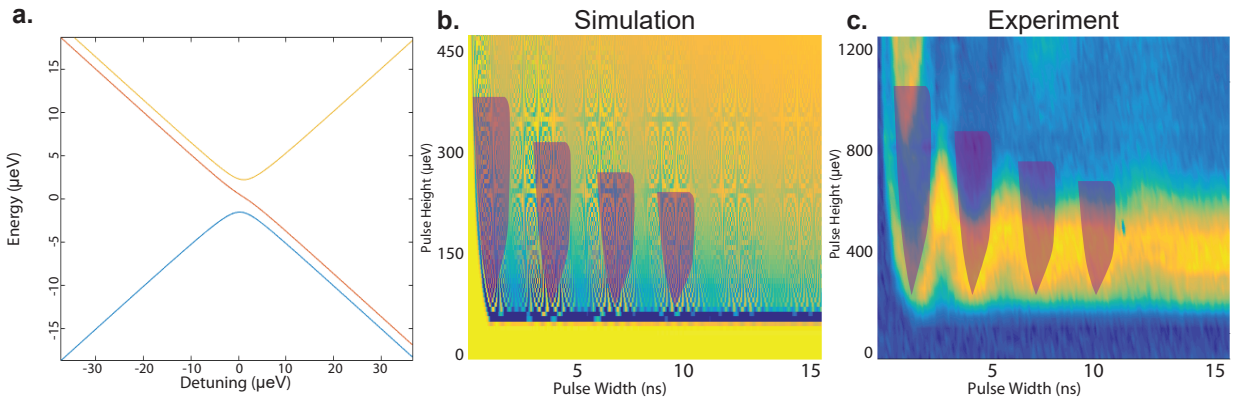


Figure 6.3: a.) A spectrum leading to a low efficiency spectroscopy process. b.) Its simulation in addition to highlights of those features appearing with the splitting frequency. c.) Raw data showing nearly vertical features at that frequency.

scale. The valley splitting in this instance is equal to 340 MHz, an order of magnitude less than the efficient system outlined in chapter 5. We then applied a trapezoidal pulse, and observed the final probability of returning to the measurement dot. The results of this simulation are shown in Figure 6.3b.

The probability of returning to the measurement dot in such an inefficient system is always very close to 1. Despite the fact that the system is not efficient with these pulses, the simulation produces features at the frequency of the valley splitting. In the figure those features are highlighted in purple. When examined closely it can be seen that these are fast oscillations with a sinusoidal envelope given by the frequency of the valley splitting. If the measurement process were highly non-linear, perhaps by taking a long time to re-initialize from an excited state through a tunneling process, then these features could be observed as the features seen in the experimental data in Figure 6.3c.

## 6.3 Ramsey-Like Spectroscopy in noise resistant region

Ramsey interferometry is a way of exploring the spectrum of a two state system. The outline for such a process as canonically described is shown in Figure 6.4. It is composed of four steps. The system begins initialized in the ground state, and the first step is a $\frac{\pi}{2}$ pulse about the $x$-axis

of the Bloch sphere. This has the effect of loading the system into an even mixture of the $|0\rangle$ and $|1\rangle$ states. The second step is to allow they system to evolve freely for a variable time $\tau$. This corresponds to a rotation of the state around the $z$-axis of the Bloch sphere. Phase will be accumulated at a rate given by $\Delta\phi = \frac{\Delta E_{01}}{2\pi\hbar}\tau$. The third step is another $\frac{\pi}{2}$ pulse about the $x$ axis. The effect of this pulse depends on the accumulated phase during step 2, as shown in Figure 6.4b. The final step is a measurement/initialization phase, during which the state of the system is read out. The probability of being in state $|1\rangle$ vs $|0\rangle$ will be an oscillatory function of time, with the frequency given by the value $\Delta E_{12}$, which is the value sought.

The $\frac{\pi}{2}$ operations were traditionally realized by applying an oscillatory field. In quantum dot charge qubits, this corresponds to applying two microwave pulses on top of slow adiabatic pulses to create the different parts of the sequence.[KWS15] However, in the work described here, the $\frac{\pi}{2}$ operations were performed by applying non-adiabatic square pulses in detuning. The system begins in detuning $\varepsilon_0$, the initialization/measurement detuning. The square pulses are then applied. The duration of these pulses is called $t_{\pi/2}$ and the detuning to which the system was pulsed is given by $\varepsilon_{\pi/2}$. The free evolution point of detuning is called $\varepsilon_\tau$ and can be varied in order to read out the detuning dependence of the energy splitting.

The approach taken when probing the device Q1AB2 was similar in spirit to that of Ramsey inteferometry. It was also similar to the approach taken by at least one other group[SSW14]. Figure 6.5 shows the results of such a Ramsey experiment applied to the device Q1AB2. As can be seen, there appears to be a sweet spot for $\varepsilon_{\pi/2}$. Also, if $t_{\pi/2}$ is increased or decreased (the resolution of the AWG610 used to perform these experiments is 6 GS/s), visibility is reduced to almost nothing and the pattern changes. The sweet spot for $\varepsilon_{\pi/2}$ appears to correspond with the base of the first lobe of coherent oscillations observed with just a square pulse, as can be seen in figure 6.5a. Additional Ramsey-like experiments with Q1BI2 confirms that this is generally the sweet spot, though the signal in that sample is less robust. The frequency observed at an operation point of $\varepsilon_\tau = \varepsilon_0$ seems to be almost the same as that observed with the fast pulse. This suggests either that there is a very similar valley splitting within the two dots or that there is a small inter-dot coupling, so that the same valley splitting is measured since the electron never returned to the original dot for operation.

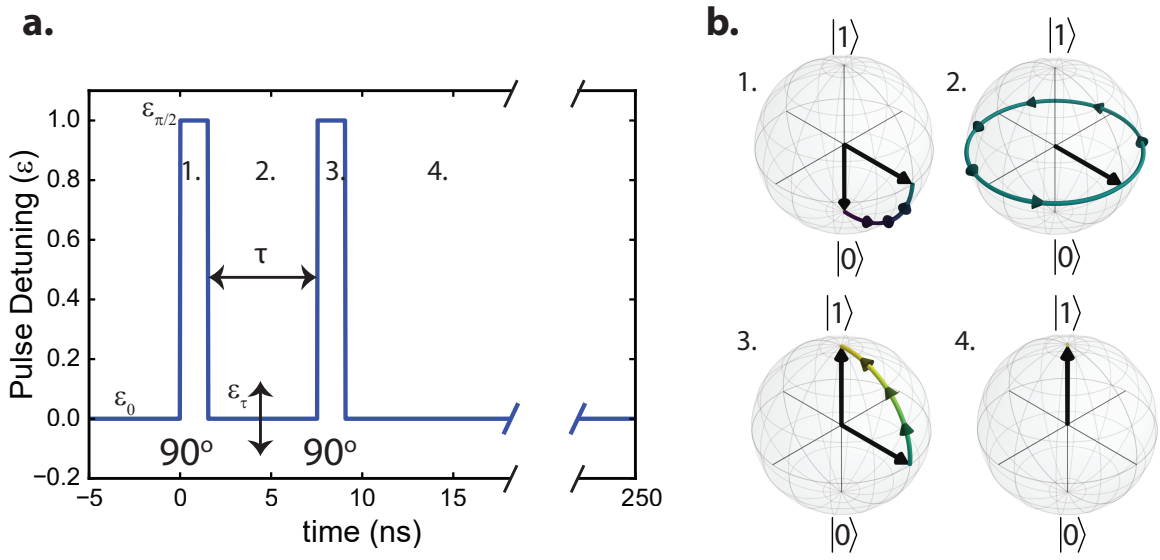


Figure 6.4: a.) The pulse sequence associated with a Ramsey spectroscopy experiment. b.) The canonical operations associated with a Ramsey pulse on the Bloch sphere.

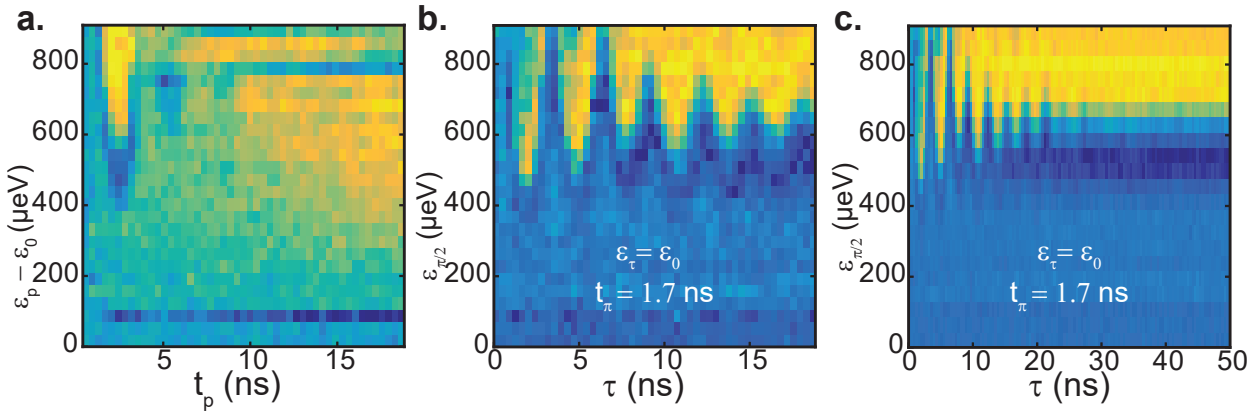


Figure 6.5: a.) The result of a square pulse with pulse duration $t_p$. b.) The result of a Ramsey pulse shape with $\varepsilon_\tau = \varepsilon_0$, where $\varepsilon_{\pi/2}$ and $\tau$ are both varied. c.) A more detailed scan showing how far out the fringes extend in the time domain.

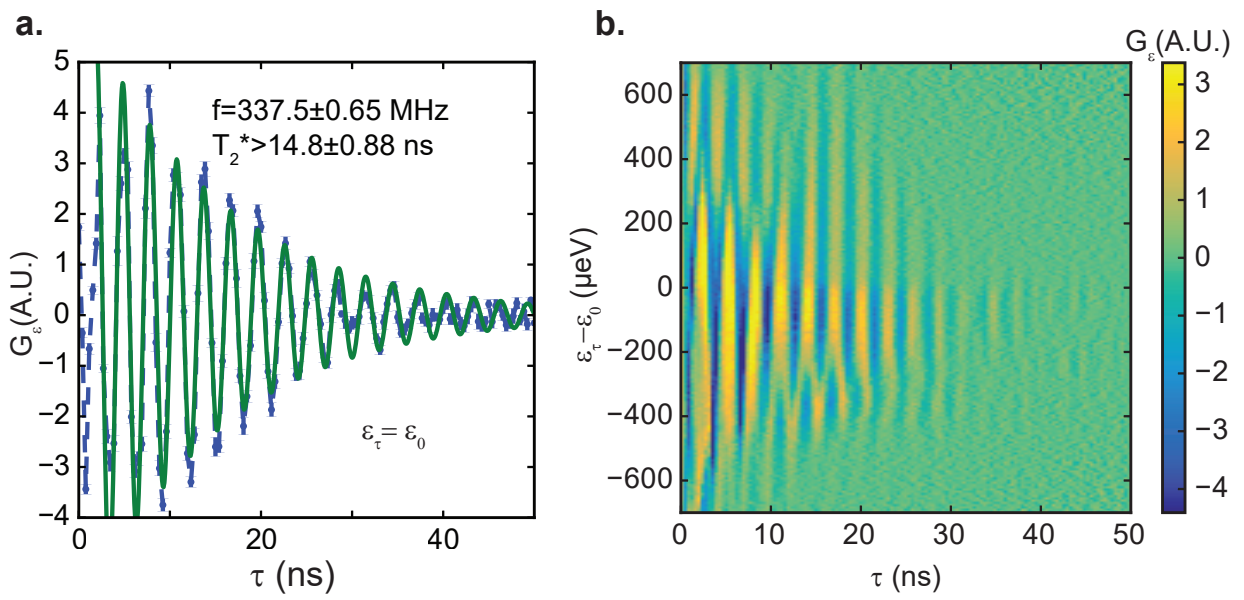


Figure 6.6: a) Charge sensing signal vs free evolution time, $\tau$, of a Ramsey-style pulse at the free evolution detuning point of maximum coherence time. A decaying sinusoidal fit reveals a long coherence time of 14.8 ns b) The dependence of the time domain oscillations as a function of the free evolution detuning point relative to $\varepsilon_0$. This reveals a relatively flat dispersion.

Having optimized the $\frac{\pi}{2}$ pulse height and duration, the next step was to vary the free evolution point, $\varepsilon_\tau$. This allows for the spectrum to be mapped by seeing how the energy splitting varies with detuning. From the square pulses, it was already evident that the operation frequency did not change over many hundreds of $\mu$eV in the operation dot. However, the Ramsey-style pulse allows us to see that the same is true in the measurement dot (subject to the caveat mentioned above). As can be seen in Figure 6.6b, the rate of phase accumulation does not seem to vary over a wide range of detuning. This detuning invariance of the splitting suggests the possibility that the operation may have a long coherence time. In fact, it does. As can be seen in Figure 6.6a, the coherence time for this system can be as long as 15 ns, which is quite long for a charge qubit.[1]

[1]But not as long as it could potentially be[MCZ17].

### 6.3.1 The $\frac{\pi}{2}$ pulses

For a charge qubit, this scheme works because at $\varepsilon_{\pi/2}$, which is often chosen to be $\varepsilon = 0$, the eigenstates of the system are even mixtures of $|0\rangle$ and $|1\rangle$, which means pulsing non-adiabitcally to that detuning induces rotation around the $x$ axis of the Bloch sphere, as required. However, in the case of our system, it is not completely clear that this is the effect of our square pulses. It is clear that some coherent mixing is occurring as the result of the pulses, which allows us to explore the spectrum of the dots and discover the low dispersion regime. However, as has been seen in chapter 5, there is a fair amount of flexibility in the non-adiabatic mixing operation. So long as such an operation is applied twice in succession, the overall outline of the interferometry is similar. It is therefore possible that the relevant part of the square pulse operation was not even the time $t_{\pi/2}$. Rather, the pulse itself could cause coherent mixing, perhaps through a Landau-Zener mechanism. The total effect of such a Landau-Zener square pulse has been shown to be sufficiently expressive to induce any single qubit operation[CLT13], including a $\frac{\pi}{2}$ rotation about the $x$ axis.

However, the fact that there is a sweet spot for both $\varepsilon_{\pi/2}$ and $t_{\pi/2}$, along with the fact that the pulses are relatively long (nominally about 1.3 ns), suggest that the visibility really is caused by something akin to a $\frac{\pi}{2}$ rotation about the $x$ axis during the time it is detuning.

## 6.4 Charge Noise Resistance from Non-Valley Systems

For a qubit space, the off diagonal term of the density matrix, roughly indicative of the phase coherence of the system, evolves in time as [Qin16]:

$$\frac{\mathrm{d}\rho_{01}}{\mathrm{d}t} = -\frac{i}{\hbar}\left(E_0 - E_1\right) - \gamma_{01}\rho_{01}.$$

The first term is simply the evolution expected from the Schrodinger equation. The second term is a the decay term. The coefficient $\gamma_{01}$ determines the rate of decay and is related to the noise power spectrum $S_\zeta(\omega)$ and the nature of the spectrum. Approximating the system of interest

as a two state system, one obtains

$$\gamma_{01} \approx \frac{\pi}{4}\left(1 - \left(\frac{\partial E_{10}}{\partial \varepsilon}\right)^2\right) S_\zeta\left(\omega_{01}\right) + \pi\left(\frac{\partial E_{10}}{\partial \varepsilon}\right)^2 S_\zeta\left(0\right).$$

The first term is the result of relaxation. However, the second term, which dominates is the effect of dephasing. This ultimately gives something akin to the results for a charge qubit[PPL10]:

$$T_2 = \frac{\sqrt{2}\hbar}{\sigma_\varepsilon}\left(\frac{\partial E_{01}}{\partial \varepsilon}\right)^{-1}$$

For an unprotected charge qubit, the slope of the spectra as plotted against detuning will be almost exactly 1. That is,

$$\frac{\partial E_{01}}{\partial \varepsilon} \approx 1,$$

so a change in potential asymmetry almost directly translates to a change in eigenstates energy difference.

In addition to coherent oscillations resulting from valley physics, which were present at multiple charge configurations, we found certain oscillations present at only a single charge configuration. Such osccilations and their numerically calculated dispersion can be seen in Figure 6.7. Definitively determining their source (perhaps exchange based) will be the subject of future work. Nevertheless these oscillations also benefited from the effects of being in a protected region. For these oscillations, which display the greatest range of oscillation frequencies observed in our setup, the frequency of oscillation changes roughly 6 GHz over roughly 1000 $\mu$eV. This corresponds to

$$\frac{\partial E_{01}}{\partial \varepsilon} \approx \frac{2\pi\hbar\,(6\,\mathrm{GHz})}{1000\,\mu\mathrm{eV}} \approx 0.03$$

In the case of a charge qubit, This allows us to compare the $T_2^*$ times due to charge noise in the two cases.

$$T_2^* \propto \left(\frac{\partial E_{10}}{\partial \varepsilon}\right)^{-1} \approx \begin{cases} 1 & \text{charge qubit} \\ 43 & \text{protected state} \end{cases}$$

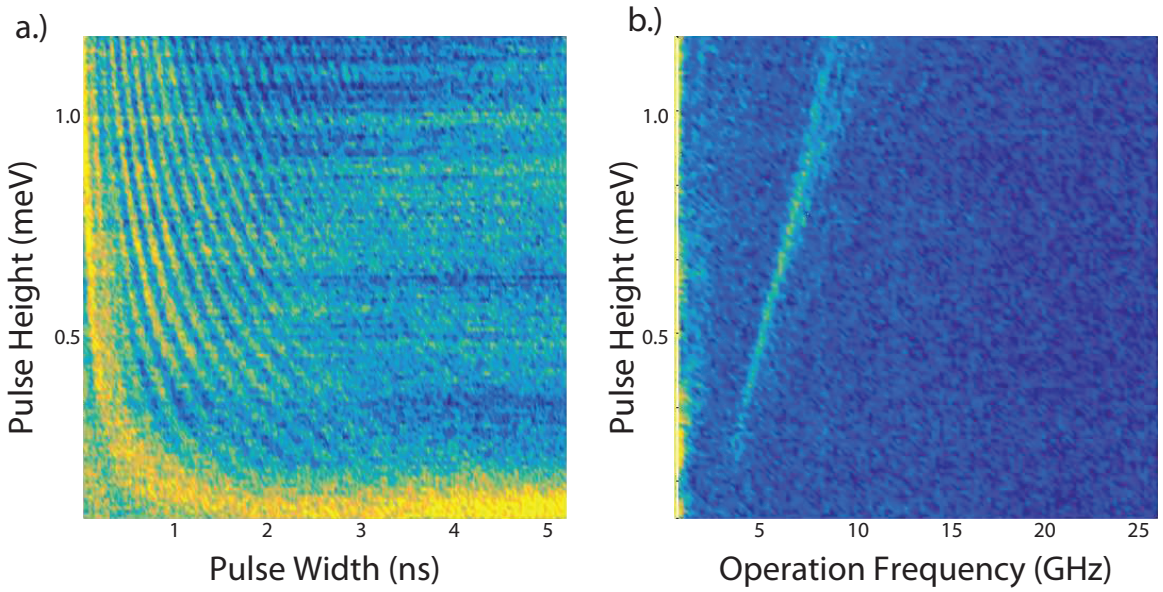


Figure 6.7: a.) Protected oscillations from an effect other than the valley states. b.) The numerically calculated dispersion showing the slow rate of change of $\Delta E_{12}$.

Given the level of $T_2^*$ observed in the regions that are protected, we can see that for the regions with unit slope in the spectra, the expected dephasing rate may be only a few tens of picoseconds, which is why we fail to observe them. This also allows us to estimate the total integrated power spectral density as:

$$\sigma_\varepsilon = \frac{\sqrt{2}\hbar}{T_2}\left(\frac{\partial E_{10}}{\partial \varepsilon}\right) = \frac{\sqrt{2}\hbar}{(1.5\,\text{ns})} \cdot 42 = 27\,\mu\text{eV}$$

Which is a factor of three higher than that reported in observed charge qubit systems[PPL10]. This is still consistent with our our reported values of the contribution to the charge noise from the individual gates,[FSJ16] as the total integrated spectrum is hard to model.

# CHAPTER 7

# Future Directions

## 7.1 Key Improvements and Future Directions

Work began in $Si/SiO_2$ devices. The MOS devices described in previous theses were fabricated on substrates with a 50 nm thick layer of insulating $SiO_2$. It was believed that reducing the thickness of this layer would result in improved confinement and decreased screening of the top-gate. In addition the size of the devices themselves was decreased, leading to noticeable improvements in the patterns of the stability diagram.

By far the greatest improvement in device performance, however, came from switching from a $Si/SiO_2$ based device architecture to one based on SiGe. Rather than deep wells with very high charging energy and inter-dot transitions with seemingly no ability to be tuned, we had dots on which nearly every gate had its designed effect. With the change of a few millivolts of confinement voltages, the inter-dot and charging tunneling rates could be varied over a wide range. In a sense this is not surprising, as other research groups had reported on the high quality of dots formed using undoped Silicon quantum wells embedded in insulating SiGe. However, by applying nearly identical fabrication techniques and using lithographically identical patterns, we were able to determine that there were in fact unique challenges to using MOS devices.

Looming largely among these challenges was the fact that seemingly identically patterned devices in MOS would result in dramatically different dot configurations. We believe that this is because the majority of dots formed in MOS devices are not lithographically defined, but rather are the result of deep incidental wells resulting from the presence of defects at the interface. Devices based on SiGe, however, seem to be considerably less prone to the formation of immobile and deep traps.

If the number of incidental deep traps could be reduced, it may be possible for MOS based systems to exhibit the same high tunability of SiGe based systems.

To that end, an important next step is to try to reduce the number of defect based charge traps within MOS-dots systems. We believe that the damage imparted to the devices from our electron-beam lithography steps could be considerable and could contribute to the presence of these traps. To counteract the formation of these traps, it would be useful to attempt a fabrication technique that does not involve bombarding the device with high energy electrons.

This is challenging because of the scale of our devices. Photolithography, which uses ultra-violet light to form patterns, is not appropriate for this length scale as the wavelength is several hundred nanometers. Although state of the art photolithography can achieve this scale, it is well outside the capabilities of our university clean-room setup.

Instead of photolithography, we will use a different, and less common, form of lithography: Nanoimprint Lithoraphy (NIL). In NIL, a stamp is used to directly press into the resist, forming a pattern in the resist in the same shape as the stamp.[Zho13] The stamp is generally formed in some hard substance such as either silicon or quartz. The resist (such as PMMA) is then spun on the sample and heated beyond its glass transition temperature and the stamp is then pressed under several Megapascals of pressure into the resist. This lithographic technique has the potential for both extremely high resolution and extremely high throughput. But most importantly, because it does not rely on a high energy beam of electrons, it could potentially reduce damage to the oxide, resulting in a cleaner interface in the region near the dots.

The use of accumulation only devices[ZHM15, VYH15] also seems like a promising avenue for exploration. Groups have reported that the value for charge dephasing in these systems, particularly when readout is done through strongly coupling the dots to a microwave cavity, can be as long as several hundred nanoseconds (two orders of magnitude greater than reported using other gate architectures). [MCZ17]

On another note, one of the recurring difficulties encountered while taking data was the absence of clearly visible coherent effects in regions where the dispersion was rapidly changing, even when the setup was capable of producing clear oscillations in those regions with relatively

flat dispersion. Furthermore, when electron temperatures have been measured, they have often been found to be in excess of 300 mK,[1] even when the base temperature of the fridge is as low as 40 mK and electron temperatures from other university labs have been around 100 mK.[MPB17]

The high electron temperatures observed here suggest that there is considerable room for improvement in isolating the device from heating effects, particularly those transmitted through the wires.

A countermeasure that we currently take in order to shield the device from heating through the wires, in addition to standard measures such as thermal anchoring at the different fridge stages, is the use of stainless steel wire (Cooner wire) for all lines not intended to transmit high frequency signals. This wire is less conductive to heat and therefore contributes to thermally isolating the device from room temperature.

However, there is still the possibility that the ability to transmit electrical signals can lead to heating the electron temperature. Therefore, an additional countermeasure would be to electrically isolate these low frequency lines in addition to the thermal isolation already provided by the thermal anchoring and the use of stainless steel wires. Low pass filters can be used to block those electrical signals coming from the room temperature portion of the wire. Multi-pole RC filters can be used to block signals greater than several hundred kilohertz. Also, metal powder filters can be used to block microwave signals, which may contribute strongly to heating. More generally, moving forward, improved isolation of the device and noise reduction will be crucial.

## 7.2 Conclusion

With our dot design, fabrication techniques and experimental setup, we have demonstrated the ability to produce clear and repeatable time-resolved quantum oscillations across several different devices. Furthermore, even though these quantum oscillations do not yet themselves represent complete control over the quantum states of an electron, such as would be required for a qubit

[1] It is possible that the electron temperature in the Triton dilution fridge setup is lower than this and that the measurement in agreement with this is the result of lag between the reading on the temperature sensor and the device itself coming to the correct temperature as the heaters in the fridge are engaged.

in a realized quantum computer, they are useful for directly measuring important properties of a given quantum dot configuration – specifically the valley splitting.

Perhaps more exciting, though, is the prospect that with sufficient control and sophistication in reducing noise, the valley states of silicon which were manipulated in this work could some day represent a viable qubit in their own right. More generally, the valley states of silicon represent an interesting frontier to be explored. Many of the features of spin physics, such as blockade and long coherence times, can potentially be realized in the valley degree of freedom.

Silicon is a special material for the technology community. The rapidly oscillating conducing states of silicon are also special. Their potential for use as well as the unique challenges they present have only begun to be explored. As semiconducting quantum devices move increasingly to silicon, the valley states of silicon have become impossible to ignore. Perhaps, someday, even conventional electronics will have to recon with these special states. My hope is that the work here will serve as a helpful contribution to a future of valleytronics.

# APPENDIX A

# Simulation and Software

## A.1 Simulation of Lock-In Signals

A lock-in current signal will be given by

$$\Re\left[I_{\text{lock-in}}\left(\theta\left(\hat{V}\right)\right)\right] = \int I\left(\theta\left(\hat{V} + A\sin\left(\phi\right)\right)\right)\sin\phi \mathrm{d}\phi$$

where the measured current through the QPC, $I$, is a function of parameters $\theta$, which in turn depend on the voltage $V$. The quantity $A$ is the lock-in voltage excitation amplitude.

In the case of our setup, $I$ is the average QPC signal over many pulse trains. The parameters of import, $\theta$, are $\varepsilon_p$, and $t_p$. Since $\varepsilon_p = \varepsilon_0 + \varepsilon_{\text{nom}}$, and $\varepsilon_{\text{nom}}$ is determined by the pulse generator and not the fixed voltage of the side gates, $\varepsilon_0$ is the only parameter that is affected by the excited voltage $V$. So, we may write, $\varepsilon_0\left(\phi\right) = \hat{\varepsilon}_0 + \alpha A\sin\left(\phi\right)$. Therefore:

$$\begin{aligned}\Re\left[I_{\text{lock-in}}\left(t_p, \varepsilon_{\text{nom}}, \varepsilon_0\right)\right] &= \int I\left(t_p, \varepsilon_{\text{nom}}, \hat{\varepsilon}_0 + \alpha A\sin\left(\phi\right)\right)\sin\left(\phi\right)\mathrm{d}\phi \\ &\approx \sum_{\phi_i=-\frac{\pi}{2}}^{\frac{\pi}{2}} I\left(t_p, \varepsilon_{\text{nom}}, \hat{\varepsilon}_0 + \alpha A\sin\left(\phi_i\right)\right)\sin\left(\phi_i\right)\end{aligned}$$

Where, each of the terms $I\left(t_p, \varepsilon_{\text{nom}}, \hat{\varepsilon}_0 + \alpha A\sin\left(\phi_i\right)\right)$ may be computed in a separate simulation. This became the simulated lock-in signal.

## A.2 GPU accelerated quantum simulation

The time dependent simulations shown in this work were produced by time evolving the Von Neumann equation,[1]

$$\frac{\partial \rho(t)}{\partial t} = -\frac{i}{\hbar}[H(t), \rho(t)],$$

where $\rho$ is the density matrix of the system and $H$ is the Hamiltonian of the system.[WM09] If the dimension of the Hilbert space is $D$, then the density matrix is a $D \times D$ positive semi-definite Hermitian matrix of unit trace. Each element of this matrix represents one of the coupled differential equations that we solve numerically. These constraints on $\rho$ mean that there are actually only $\frac{D^2+D}{2} - 1$ independent elements. In practice, however, we solve $\frac{D^2+D}{2}$ coupled equations and use the fact that the trace should be preserved in order to check for numerical errors.

There were many parameters, some of which were properties of the control pulses and some of which were parameters of the Hamiltonian. In order to reproduce the experimental data collected, it was necessary to run a separate simulation for each different data point within a given trace of data. Often times, the data we wished to reproduce was 2 dimensional. For example, a typical scan of pulse width versus pulse height, such as those shown in Figure 5.3, would contain roughly 150 different pulse widths and 60 different pulse heights.

When run on a single core, a single solution of the Von Neumann equation could take up to a few seconds for $D = 3$. If each time dependent simulation took 1 second, then the total time to perform the simulations for the trace above would require 2.5 hours. During the initial stages of parameter exploration devoting that much time to each trace would be be impractical.

Fortunately, the problem of solving the Von Neumann equation several thousand times for different parameters is nearly perfectly parallelizable, since the problems are each completely independent of one another, meaning that it has potential for speedup proportional to the number of cores available. Such problems are also appropriate for many out of the box parallel computing solutions. For example, if there are many CPU cores available, one can use the "parallel for"

[1] This equation is equivalent to the Schrodinger equation using the density matrix formalism.

function (`parfor` in Matlab from the Parallel Computing Toolbox), which will simply send different iterations of a for loop to separate cores, provided that there is no information transfer between iterations. However, the total number of CPU cores available to our group on a single system is limited to between 4 and 32[2]. A speedup of 4x is helpful but not sufficient.

In recent years there has been an increased interest in using Graphical Processing Units (GPU) for scientific computing. These units are dedicated pieces of hardware which can be added to a computer in order to accelerate its performance for graphics intensive processes. Figuring out what color a given display pixel needs to be is a pretty easy problem. However, there are very many pixels for which this calculation needs to be done. A GPU is a dedicated hardware unit that contains very many low powered computing cores. Each individual core is not very fast. But when the problem is that there are very many relatively simple and independent problems that need to be solved, such as in graphics acceleration, GPU computing can offer significant speedup. Our many independent Von Neumann equation solutions are another such problem.

The GPU used to conduct our simulations was an Nvidia GeForce 760. This GPU contains 1152 cores each clocked at 980 MHz, which would be quite slow for a CPU. In addition it has 2 GB of memory, which is important for storing all of the necessary variables for each of the computations. Though the speed of an individual computation takes a fairly significant hit from the switch from a CPU core to a GPU core, the total number of computations that can be done in parallel overwhelmingly outweighs that slowdown when performing many hundreds or thousands of separate simulations.

[2]Four cores was the most that any machine in our lab had available. However more cores were available as EC2 instances from Amazon Web Services.

### A.2.1 Details of Implementation with MATLAB `gpuarray`

To solve the differential equation we used the Runge-Kutta method (RK4)[WA04]. This is a numerical solution to a first order differential equation specified in the following way:

$$\frac{df}{dt} = f\left(t, y\right) \qquad\qquad y\left(t_0\right) = y_0,$$

where $y$ can be a vector. The system is evolved in time steps of size $h$ according to the update rule

$$y_{n+1} = y_n + \frac{h}{6}\left(k_1 + 2k_2 + 2k_3 + k_4\right),$$

where

$$\begin{aligned}
k_1 &= f\left(t_n, y_n\right), \\
k_2 &= f\left(t_n + \frac{h}{2}, y_n + \frac{1}{2}k_1\right), \\
k_3 &= f\left(t_n + \frac{h}{2}, y_n + \frac{1}{2}k_2\right), \\
k_4 &= f\left(t_n + h, y_n + k_3\right),
\end{aligned}$$

meaning that at each time step 4 different evaluations of $f$ must be performed. Using this system, we place the $\frac{D^2+D}{2}$ elements into a vector, which stands for $y$. The function $f\left(t, \vec{\rho}\right) = \frac{-i}{\hbar}\left[H\left(t\right), \rho\left(t\right)\right]$

We implemented our GPU simulation using the Matlab parallel computing toolkit, which allows for very simple array based GPU computing. Matlab has built in acceleration for certain functions such as matrix multiplication. That was not sufficient for our use, however. Our goal was to use the individual cores to each independently solve the differential equation. In Matlab the basic GPU unit is the `gpuarray`. This represents an array of data which is present on the GPU. Each array represents a scalar on the individual cores. One can then perform array functions to manipulate these scalars. For example, `c = a + b`, where `a` and `b` are both a `gpuarray` is computed by each core computing a single addition operation and storing the result as another `gpuarray`. Therefore, the operations to compute the time dependent hamilto-

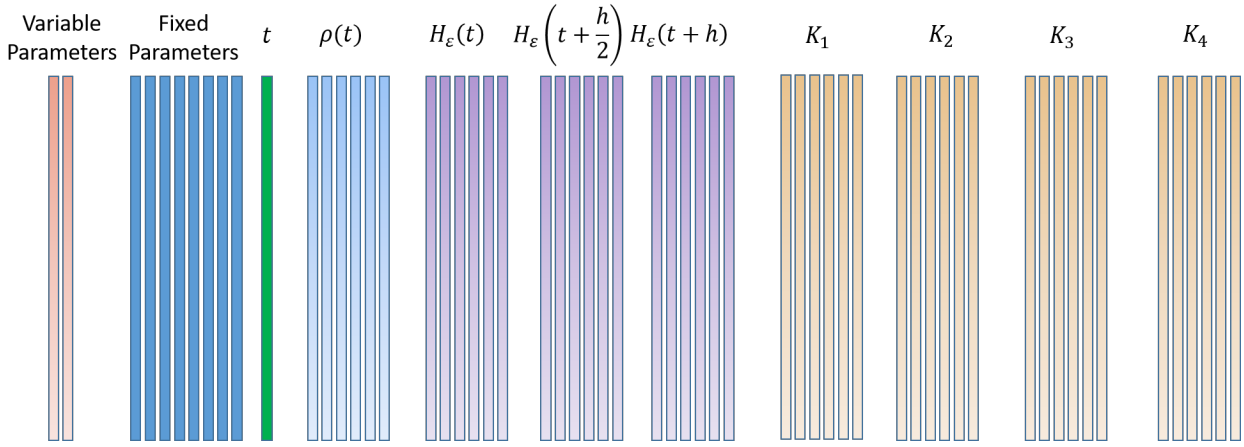


Figure A.1: A diagram representing the various `gpuarray` objects which are explicitly created to perform the Runge-Kutta method on the Von Neumann equation. Other arrays are made implicitly in this process. Note that each element of the density matrix and Hamiltonian is its own array. A solid array means that every element of that array is the same value at a given time step. The update equation is given by $\rho_i\,(t+h) = \rho_i\,(t) + \frac{h}{6}\,(k_{i,1} + 2k_{i,2} + 2k_{i,3} + k_{i,4})$.

nian as well as the operations to compute the commutators must be expressed as scalar functions of the elements of the hamiltonian and the density matrix. The commutators are particularly challenging, as writing out the commutator of two Hermitian matrices as a function of the independent elements and returning only the independent elements is taxing to do by hand. To generate these scalar functions we use the Matlab Symbolic Math toolbox, which has the ability to create Matlab functions from the results of its symbolic calculations, which can then be turned into array functions. Code demonstrating an example of the commute function being converted to a function of scalars is given in. The outline of the process can be seen in Figure A.1.

This system was independently implemented by both me and Blake Freeman. Most of the work shown here was done using the Freeman implementation, which despite being somewhat slower due to an increased number of implicitly created `gpuarray`'s, was considerably more expressive and more developed. For the 3 and 4 dimensional simulations presented here, the difference in time was less significant than it would have been for the 8 dimensional simulation required for the Resonant Exchange qubit simulation that the Schoenfield implementation was made for.

**Algorithm A.1** Function to compute the commutator of 3 Dimensional Hermitian matrices $H$ and $\rho$, $[H, \rho]$. The variables `h1`, `h2`, ... `h6` stand for the 6 independent complex elements of $H$ and the variables `p1`, `p2`, ... `p6` stand for the 6 independent complex elements of $\rho$. The order is given by the upper right half of the matrix read like a book.

```
function [out1, out2, out3, out4, out5, out6] = ...
    dm_commute_gpu_3(h1,h2,h3,h4,h5,h6,p1,p2,p3,p4,p5,p6)
    %DM_COMMUTE_3
    %    F = DM_COMMUTE_3(H1,H2,H3,H4,H5,H6,P1,P2,P3,P4,P5,P6)
    %    This function was generated by the
    %   Symbolic Math Toolbox version 6.0.
    %    02-Mar-2015 11:20:54
    t2 = conj(p2);
    t3 = conj(h2);
    t4 = p2.*t3;
    t5 = conj(p5);
    t6 = conj(h5);
    t7 = conj(p3);
    t8 = conj(h3);
    t9 = p3.*t8;
    t10 = p5.*t6;
    out1 = t4+t9-h2.*t2-h3.*t7;
    out2 = -h1.*p2+h2.*p1-h2.*p4+h4.*p2-h3.*t5+p3.*t6;
    out3 = -h1.*p3+h3.*p1-h2.*p5+h5.*p2-h3.*p6+h6.*p3;
    out4 = -t4+t10+h2.*t2-h5.*t5;
    out5 = -h4.*p5+h5.*p4-h5.*p6+h6.*p5+h3.*t2-p3.*t3;
    out6 = -t9-t10+h3.*t7+h5.*t5;
```

## A.3 Simulation Aided Design

To aid the design of our devices we used Comsol Multiphysics software to reconstruct the geometry of our devices and then solve the electrostatic Poisson equation for a semiconductor. The geometry can be seen in Figure A.2a. The top of the geometry was associated with the voltage of the top gate. The internal faces of the geometry were given voltages of the side gates that they represent.

These simulations helped in switching from a circular design as is shown in Figure A.2a, to a linear design such as that detailed in the main text and the device being solved in Figure A.2b. The appropriate voltages were sometimes not so similar to what simulation said they should be. Also simulation suggested that a large negative voltage on the gate controlling the QPC could be quite disruptive to dot formation, though this did not turn out to be the case in general.

Also attempted was a self consistent Poisson-Schrodinger equation solution. However the results of such simulations as performed by us were not generally indicative of what we observed in terms of dot formation. They in general did not provide better insight than the poisson-only simulations. In MOS-dots this is likely because of the presence of deep charge traps, which were the primary drivers of dot formation.

## A.4 Pulse Design

In order to carry out more sophisticated pulsing for dot control we wrote pulse design software in Matlab which allowed for simple and idomatic scripting of pulses involving ramping to different values with the AWG 610 and 520 Arbitrary Waveform Generators. An example of a desired ramp pulse is given in Figure A.3.

In the new system pulses were described by a pulse profile with names for each of the individual steps. Each individual step can be specified by the following five features.

1. The name for the step as a string

2. What sort of step it is.

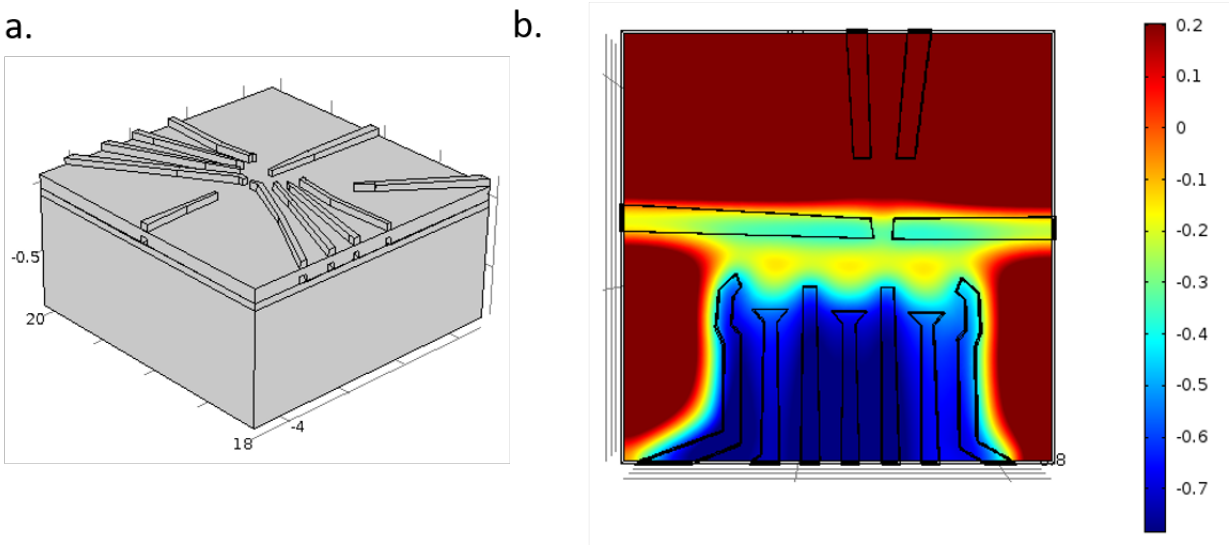


Figure A.2: (a) An example of the geometry over which the electrostatic equations were solved. This is an early design used in the lab different from that used in the paper. (b) An example of our simulation showing the electrostatic potential at the interface (which would be at roughly the depth of the quantum well). This demonstrated the viability of the linear design for producing many dots in a row and how the gap in the wall separating the dots from the QPC does not preclude dot formation. This was a draft of a potential triple dot design.

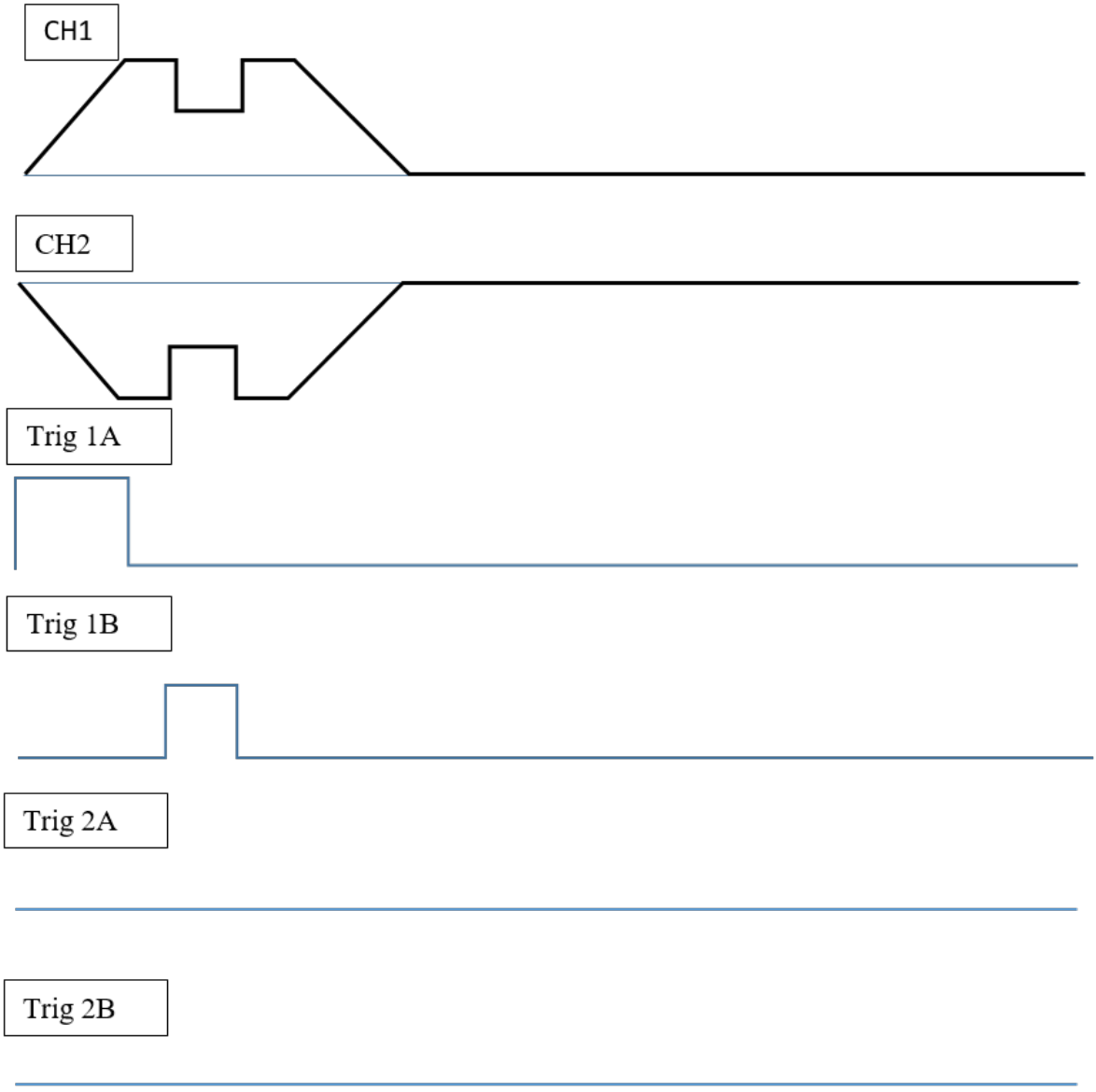


Figure A.3: The Desired Pulse to be creaed with the `rampPulse` software.

   (a) Point to directly specify the voltages
   (b) Vector to specify the “direction” of the pulse
3. The time to ramp up to the step.
4. The voltages to dwell at for the next step. If this is not zero for the last step, then the voltages will fall to zero after the final dwell time.
5. The time to dwell at the next step

The different parts of the pulse are shown in Figure A.4. The markers can be specified by:

1. The name for the marker feature
2. Relative to what step in the pulse signature you want to specify the time. These are the same step names that you defined with the pulse signature.
3. Relative to what part of the pulse step you want to specify the time
   (a) ‘r’amp: The moment it starts ramping
   (b) ’b’eginning; The moment it begins to dwell
   (c) ’e’nd; The very end of the step
4. What sort of feature you want to add
   (a) ‘Add’: adds time where the value is 1
   (b) ‘Subtract’: removes time where the value is 1
5. The offset in time from the specified point. This can be negative, meaning that it begins before the specified point.
6. The duration of the marker feature. This can also be negative.
7. Which marker channel. This is specified as [# of channel, # of marker]

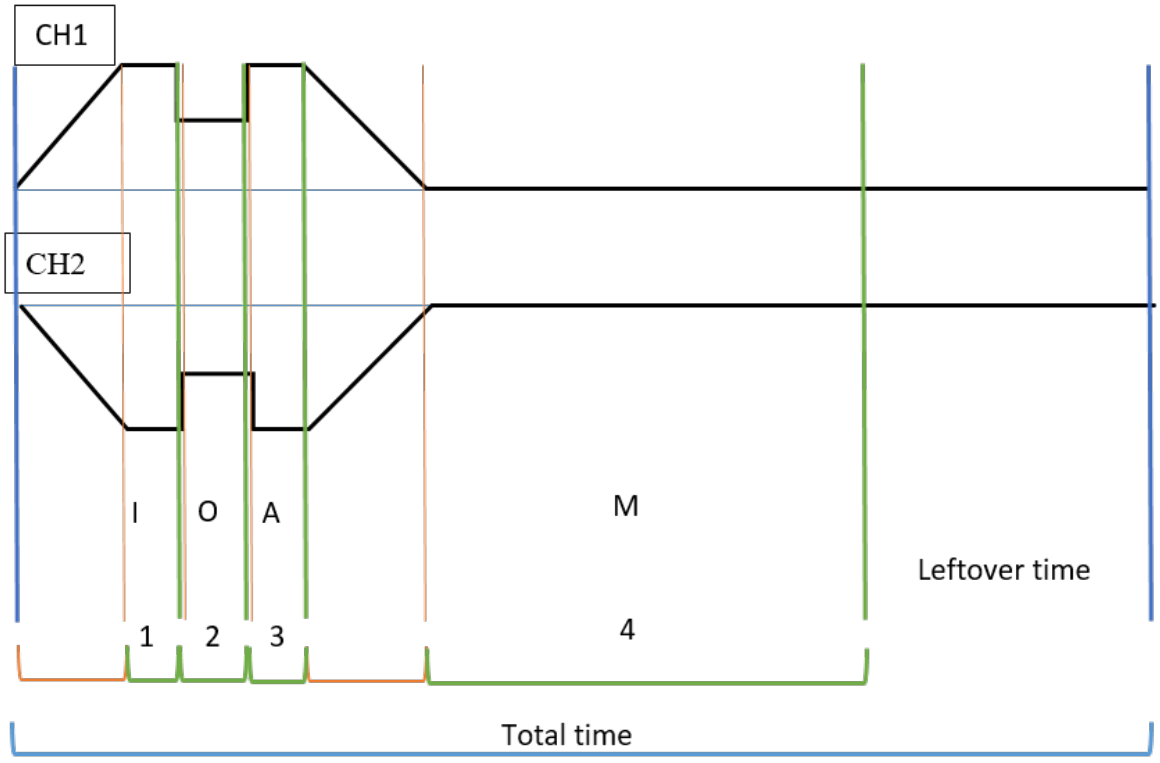


Figure A.4: The different parts of a fully specified 4-step pulse which can be used to make pulses like that in Figure A.3.

The main benefit of the `ramp_pulse` software is its ease of expression. Sets of pulse files for the AWG are created by writing scripts containing loops that change one or more parameters in the definition of a `rampPulse` object, which in turn creates an AWG run file corresponding to that pulse form. An example of a complete script for the pulses described in Figures A.3 and A.4 is given in Algorighm A.2.

**Algorithm A.2** Example of scripting to generate many pulses like those in figure A.3 of differing operation time.

```
for t_o_in_ns = 0:1:100
    sprintf('%d ns', t_o_in_ns)
    clear my_IOM_pulse
    t_meas = 20e-06;
    t_o = t_o_in_ns*1e-9;
    t_wait = .5e-6;
    t_ramp = 1e-6;
    t_total = 10e-6;
    file_base =  sprintf('rabiOperation_%04dns',t_o_in_ns);

    my_pulse_signature = {'I', 'point', t_ramp, [1,-1], t_wait; ...
                          'O', 'point', 0, [.5,-.5], t_o; ...
                          'A', 'point', 0, [1,-1], t_wait; ...
                          'M', 'point', t_ramp, [0,0], 1e-06};

    my_marker_signature = ...
        {'Omk1', 'O', 'b', 'add', 0, t_o, [1,1]; ...
         'Trig1', 'I', 'r', 'add', 0, t_ramp, [1,2]};

    my_IOM_pulse = rampPulse(2, ...
                             my_pulse_signature, ...
                             t_total, ...
                             file_base,my_marker_signature);

    my_IOM_pulse.pulse_actuator.write_pulse
end
```

[AM76] Neil W Ashcroft and N. David Mermin. *Solid state physics*. Harcourt college publishers, Fort Worth, 1976. OCLC: 848759935.

[BER15] M. G. Borselli, K. Eng, R. S. Ross, T. M. Hazard, K. S. Holabird, B. Huang, A. A. Kiselev, P. W. Deelman, L. D. Warren, I Milosavljevic, A. E. Schmitz, M. Sokolich, M. F. Gyure, and A. T. Hunter. "Undoped accumulation-mode Si/SiGe quantum dots." *Nanotechnology*, **26**(37):375202, 2015.

[BSO11] R. Brunner, Y.-S. Shin, T. Obata, M. Pioro-Ladrière, T. Kubo, K. Yoshida, T. Taniyama, Y. Tokura, and S. Tarucha. "Two-Qubit Gate of Combined Single-Spin Rotation and Interdot Spin Exchange in a Double Quantum Dot." *Physical Review Letters*, **107**(14):146801, September 2011.

[BT15] Graham Batey and Gustav Teleberg. *Principles of dilution refrigeration: A brief technology guide*. Oxford Instruments NanoScience, 2015.

[CLT13] Gang Cao, Hai-Ou Li, Tao Tu, Li Wang, Cheng Zhou, Ming Xiao, Guang-Can Guo, Hong-Wen Jiang, and Guo-Ping Guo. "Ultrafast universal quantum control of a quantum-dot charge qubit using Landau–Zener–Stückelberg interference." *Nature Communications*, **4**:1401, January 2013.

[CLY16] Gang Cao, Hai-Ou Li, Guo-Dong Yu, Bao-Chuan Wang, Bao-Bao Chen, Xiang-Xiang Song, Ming Xiao, Guang-Can Guo, Hong-Wen Jiang, Xuedong Hu, and Guo-Ping Guo. "Tunable Hybrid Qubit in a GaAs Double Quantum Dot." *Physical Review Letters*, **116**(8):086801, February 2016.

[CSK12] Dimitrie Culcer, A. L. Saraiva, Belita Koiller, Xuedong Hu, and S. Das Sarma. "Valley-Based Noise-Resistant Quantum Computation Using Si Quantum Dots." *Physical Review Letters*, **108**(12):126804, March 2012.

[Dav97] John H Davies. *The Physics of Low-dimensional Semiconductors an Introduction*. Cambridge University Press, Cambridge, 1997. OCLC: 859644759.

[DiV95] David P. DiVincenzo. "Two-bit gates are universal for quantum computation." *Physical Review A*, **51**(2):1015–1022, February 1995.

[DiV00] David P. DiVincenzo. "The Physical Implementation of Quantum Computation." *Fortschritte der Physik*, **48**(9-11):771–783, September 2000.

[DSP11] Y. Dovzhenko, J. Stehlik, K. D. Petersson, J. R. Petta, H. Lu, and A. C. Gossard. "Nonadiabatic quantum control of a semiconductor charge qubit." *Physical Review B*, **84**(16):161302, October 2011.

[ELS15] Kevin Eng, Thaddeus D. Ladd, Aaron Smith, Matthew G. Borselli, Andrey A. Kiselev, Bryan H. Fong, Kevin S. Holabird, Thomas M. Hazard, Biqin Huang, Peter W. Deelman, Ivan Milosavljevic, Adele E. Schmitz, Richard S. Ross, Mark F. Gyure,

and Andrew T. Hunter. "Isotopically enhanced triple-quantum-dot qubit." *Science Advances*, **1**(4):e1500214, May 2015.

[FCT07] Mark Friesen, Sucismita Chutia, Charles Tahan, and S. N. Coppersmith. "Valley splitting theory of $\mathrm{Si}\mathrm{Ge}/\mathrm{Si}/\mathrm{Si}\mathrm{Ge}$ quantum wells." *Physical Review B*, **75**(11):115318, March 2007.

[FSJ16] Blake M. Freeman, Joshua S. Schoenfield, and HongWen Jiang. "Comparison of low frequency charge noise in identically patterned Si/SiO2 and Si/SiGe quantum dots." *Applied Physics Letters*, **108**(25):253108, June 2016.

[GEC13] John King Gamble, M. A. Eriksson, S. N. Coppersmith, and Mark Friesen. "Disorder-induced valley-orbit hybrid states in Si quantum dots." *Physical Review B*, **88**(3):035310, July 2013.

[GGK12] L. Gaudreau, G. Granger, A. Kam, G. C. Aers, S. A. Studenikin, P. Zawadzki, M. Pioro-Ladrière, Z. R. Wasilewski, and A. S. Sachrajda. "Coherent control of three-spin states in a triple quantum dot." *Nature Physics*, **8**(1):54–58, January 2012.

[HKP07] R. Hanson, L. P. Kouwenhoven, J. R. Petta, S. Tarucha, and L. M. K. Vandersypen. "Spins in few-electron quantum dots." *Reviews of Modern Physics*, **79**(4):1217–1265, October 2007.

[Hou12] Matthew Gregory House. *Lateral Quantum Dots for Quantum Information Processing*. PhD thesis, January 2012.

[HPX11] M. G. House, H. Pan, M. Xiao, and H. W. Jiang. "Non-equilibrium charge stability diagrams of a silicon double quantum dot." *Applied Physics Letters*, **99**(11):112116, September 2011.

[HRX14] Xiaojie Hao, Rusko Ruskov, Ming Xiao, Charles Tahan, and HongWen Jiang. "Electron spin resonance and spin–valley physics in a silicon double quantum dot." *Nature Communications*, **5**:3860, May 2014.

[KBV07] F. H. L. Koppens, C. Buizert, I. T. Vink, K. C. Nowack, T. Meunier, L. P. Kouwenhoven, and L. M. K. Vandersypen. "Detection of single electron spin resonance in a double quantum dot." *Journal of Applied Physics*, **101**(8):081706, April 2007.

[KGF12] Teck Seng Koh, John King Gamble, Mark Friesen, M. A. Eriksson, and S. N. Coppersmith. "Pulse-Gated Quantum-Dot Hybrid Qubit." *Physical Review Letters*, **109**(25):250503, December 2012.

[KJS16] Erika Kawakami, Thibaut Jullien, Pasquale Scarlino, Daniel R. Ward, Donald E. Savage, Max G. Lagally, Viatcheslav V. Dobrovitski, Mark Friesen, Susan N. Coppersmith, Mark A. Eriksson, and Lieven M. K. Vandersypen. "Gate fidelity and coherence of an electron spin in an Si/SiGe quantum dot with micromagnet." *Proceedings of the National Academy of Sciences*, **113**(42):11738–11743, October 2016.

[KSS14] Dohun Kim, Zhan Shi, C. B. Simmons, D. R. Ward, J. R. Prance, Teck Seng Koh, John King Gamble, D. E. Savage, M. G. Lagally, Mark Friesen, S. N. Coppersmith, and Mark A. Eriksson. "Quantum control and process tomography of a semiconductor quantum dot hybrid qubit." *Nature*, **511**(7507):70–74, July 2014.

[KWS15] Dohun Kim, D. R. Ward, C. B. Simmons, John King Gamble, Robin Blume-Kohout, Erik Nielsen, D. E. Savage, M. G. Lagally, Mark Friesen, S. N. Coppersmith, and M. A. Eriksson. "Microwave-driven coherent operation of a semiconductor quantum dot charge qubit." *Nature Nanotechnology*, **10**(3):243–247, March 2015.

[LD98] Daniel Loss and David P. DiVincenzo. "Quantum computation with quantum dots." *Physical Review A*, **57**(1):120–126, January 1998.

[MBH12] B M Maune, M G Borselli, B Huang, T D Ladd, P W Deelman, K S Holabird, A A Kiselev, I Alvarado-Rodriguez, R S Ross, A E Schmitz, M Sokolich, C A Watson, M F Gyure, and A T Hunter. "Coherent singlet-triplet oscillations in a silicon-based double quantum dot." *Nature*, **481**(7381):344–7, January 2012.

[MBT13a] J. Medford, J. Beil, J. M. Taylor, S. D. Bartlett, A. C. Doherty, E. I. Rashba, D. P. DiVincenzo, H. Lu, A. C. Gossard, and C. M. Marcus. "Self-Consistent Measurement and State Tomography of an Exchange-Only Spin Qubit." February 2013.

[MBT13b] J. Medford, J. Beil, J. M. Taylor, E. I. Rashba, H. Lu, A. C. Gossard, and C. M. Marcus. "Quantum-Dot-Based Resonant Exchange Qubit." *Physical Review Letters*, **111**(5):050501, July 2013.

[MBT13c] J. Medford, J. Beil, J. M. Taylor, E. I. Rashba, H. Lu, A. C. Gossard, and C. M. Marcus. "The Resonant Exchange Qubit." April 2013.

[MCZ17] X. Mi, J. V. Cady, D. M. Zajac, P. W. Deelman, and J. R. Petta. "Strong coupling of a single electron in silicon to a microwave photon." *Science*, **355**(6321):156–158, January 2017.

[Mer07] N. David Mermin. *Quantum computer science: an introduction*. Cambridge University Press, Cambridge, UK; New York, 2007. OCLC: 137221653.

[MHP15] X. Mi, T. M. Hazard, C. Payette, K. Wang, D. M. Zajac, J. V. Cady, and J. R. Petta. "Magnetotransport studies of mobility limiting mechanisms in undoped Si/SiGe heterostructures." *Physical Review B*, **92**(3):035304, July 2015.

[MPB17] X. Mi, Csaba G. Peterfalvi, Guido Burkard, and J. R. Petta. "High Resolution Valley Spectroscopy of Si Quantum Dots." *arXiv:1704.06312 [cond-mat, physics:quant-ph]*, April 2017. arXiv: 1704.06312.

[MSB13] Filipp Mueller, Raymond N. Schouten, Matthias Brauns, Tian Gang, Wee Han Lim, Nai Shyan Lai, Andrew S. Dzurak, Wilfred G. van der Wiel, and Floris A. Zwanenburg. "Printed circuit board metal powder filters for low electron temperatures." *Review of Scientific Instruments*, **84**(4):044706, April 2013.

[NLN13] Khoi T. Nguyen, Michael P. Lilly, Erik Nielsen, Nathan Bishop, Rajib Rahman, Ralph Young, Joel Wendt, Jason Dominguez, Tammy Pluym, Jeffery Stevens, Tzu-Ming Lu, Richard Muller, and Malcolm S. Carroll. "Charge Sensed Pauli Blockade in a Metal–Oxide–Semiconductor Lateral Double Quantum Dot." *Nano Letters*, **13**(12):5785–5790, December 2013.

[Ozh97] Yuri Ozhigov. "Quantum Computer Can Not Speed Up Iterated Applications of a Black Box." *arXiv:quant-ph/9712051*, December 1997. arXiv: quant-ph/9712051.

[Pan13] Hong Pan. *Experimental Investigation of silicon metal-oxide-semiconductor based triple quantum dot*. PhD thesis, UCLA, January 2013.

[Pet99] Charles Petzold. *Code: the hidden language of computer hardware and software*. Microsoft Press, Redmond, Wash., 1999. OCLC: 42290141.

[PGT16] Justin K. Perron, Michael J. Gullans, Jacob M. Taylor, Jr Stewart, and Neil M. Zimmerman. "Valley blockade in a silicon double quantum dot." *arXiv:1607.06107 [cond-mat]*, July 2016. arXiv: 1607.06107.

[Pob07] Frank Pobell. *Matter and Methods at Low Temperatures*. Springer Science & Business Media, February 2007. Google-Books-ID: mRZ0uPfiWTQC.

[PPL10] K. D. Petersson, J. R. Petta, H. Lu, and A. C. Gossard. "Quantum Coherence in a One-Electron Semiconductor Charge Qubit." *Physical Review Letters*, **105**(24):246804, December 2010.

[Qin16] Xiao-Ke Qin. "Decoherence of the hybrid qubit in a double quantum dot." *EPL (Europhysics Letters)*, **114**(3):37006, 2016.

[SFJ17] Joshua S. Schoenfield, Blake M. Freeman, and HongWen Jiang. "Coherent manipulation of valley states at multiple charge configurations of a silicon quantum dot device." *Nature Communications*, **8**(1):64, July 2017.

[Sho97] P. Shor. "Polynomial-Time Algorithms for Prime Factorization and Discrete Logarithms on a Quantum Computer." *SIAM Journal on Computing*, **26**(5):1484–1509, October 1997.

[SN11] J. J Sakurai and Jim Napolitano. *Modern quantum mechanics.* Addison-Wesley, Boston; Montréal, 2011. OCLC: 701605733.

[SSW14] Zhan Shi, C. B. Simmons, Daniel R. Ward, J. R. Prance, Xian Wu, Teck Seng Koh, John King Gamble, D. E. Savage, M. G. Lagally, Mark Friesen, S. N. Coppersmith, and M. A. Eriksson. "Fast coherent manipulation of three-electron states in a double quantum dot." *Nature Communications*, **5**:3020, January 2014.

[SW] Scott Aaronson and Zach Weinersmith. "Saturday Morning Breakfast Cereal - The Talk.".

[SYC16] John R. Schaibley, Hongyi Yu, Genevieve Clark, Pasqual Rivera, Jason S. Ross, Kyle L. Seyler, Wang Yao, and Xiaodong Xu. "Valleytronics in 2D materials." *Nature Reviews Materials*, **1**:16055, August 2016.

[TSM13] J. M. Taylor, V. Srinivasa, and J. Medford. "Electrically-protected resonant exchange qubits in triple quantum dots." p. 5, April 2013.

[VHY14] M. Veldhorst, J. C. C. Hwang, C. H. Yang, A. W. Leenstra, B. de Ronde, J. P. Dehollain, J. T. Muhonen, F. E. Hudson, K. M. Itoh, A. Morello, and A. S. Dzurak. "An addressable quantum dot qubit with fault-tolerant control-fidelity." *Nature Nanotechnology*, **9**(12):981–985, December 2014.

[VYH15] M. Veldhorst, C. H. Yang, J. C. C. Hwang, W. Huang, J. P. Dehollain, J. T. Muhonen, S. Simmons, A. Laucht, F. E. Hudson, K. M. Itoh, A. Morello, and A. S. Dzurak. "A two-qubit logic gate in silicon." *Nature*, **526**(7573):410–414, October 2015.

[WA04] Hans-Jurgen Weber and George B Arfken. *Essential mathematical methods for physicists, ISE*. Academic, Amsterdam; London, 2004. OCLC: 606321590.

[Wan14] Ke Wang. *Few-electron Qubits in Silicon Quantum Electronic Devices*. PhD thesis, 2014.

[WM09] Howard M. Wiseman and Gerard J. Milburn. *Quantum measurement and control*. Cambridge University Press, 2009.

[WPD13] K. Wang, C. Payette, Y. Dovzhenko, P. W. Deelman, and J. R. Petta. "Charge Relaxation in a Single-Electron $\mathrm{Si}/\mathrm{SiGe}$ Double Quantum Dot." *Physical Review Letters*, **111**(4):046801, July 2013.

[WWP14] Xian Wu, D. R. Ward, J. R. Prance, Dohun Kim, John King Gamble, R. T. Mohr, Zhan Shi, D. E. Savage, M. G. Lagally, Mark Friesen, S. N. Coppersmith, and M. A. Eriksson. "Two-axis control of a singlet–triplet qubit with an integrated micromagnet." *Proceedings of the National Academy of Sciences*, **111**(33):11938–11942, August 2014.

[YLZ11] C. H. Yang, W. H. Lim, F. A. Zwanenburg, and A. S. Dzurak. "Dynamically controlled charge sensing of a few-electron silicon quantum dot." *AIP Advances*, **1**(4):042111, December 2011.

[YRR13] C. H. Yang, A. Rossi, R. Ruskov, N. S. Lai, F. A. Mohiyaddin, S. Lee, C. Tahan, G. Klimeck, A. Morello, and A. S. Dzurak. "Spin-valley lifetimes in a silicon quantum dot with tunable valley splitting." *Nature Communications*, **4**:2069, June 2013.

[ZDM13] Floris A. Zwanenburg, Andrew S. Dzurak, Andrea Morello, Michelle Y. Simmons, Lloyd C. L. Hollenberg, Gerhard Klimeck, Sven Rogge, Susan N. Coppersmith, and Mark A. Eriksson. "Silicon quantum electronics." *Reviews of Modern Physics*, **85**(3):961–1019, July 2013.

[ZHC16] Neil Zimmerman, Peihao Huang, and Dimitrie Culcer. "Valley Phase, Interface Roughness and Voltage Control, and Coherent Manipulation in Si Quantum Dots." *arXiv:1608.06881 [cond-mat]*, August 2016. arXiv: 1608.06881.

[ZHM15] D. M. Zajac, T. M. Hazard, X. Mi, K. Wang, and J. R. Petta. "A reconfigurable gate architecture for Si/SiGe quantum dots." *Applied Physics Letters*, **106**(22):223507, June 2015.

[Zho13] Weimin Zhou. *Nanoimprint Lithography: An Enabling Process for Nanofabrication*. Springer, Berlin, Heidelberg, 2013. OCLC: 980891586.

[ZLS13] Lijun Zhang, Jun-Wei Luo, Andre Saraiva, Belita Koiller, and Alex Zunger. "Genetic design of enhanced valley splitting towards a spin qubit in silicon." *Nature Communications*, **4**:2396, September 2013.